Reconstruction of Local and Global Marine Paleoredox Conditions during Deposition of the Devonian-Mississippian Exshaw Formation (Black Shale Member) and the Evaluation of Hydrocarbon Maturation Effects

by

Shuai Yang

A thesis
presented to the University of Waterloo
in fulfillment of the
thesis requirement for the degree of
Master of Science
in
Earth Sciences

Waterloo, Ontario, Canada, 2019

Author's Declaration

I hereby declare that I am the sole author of this thesis. This is a true copy of the thesis, including any required final revisions, as accepted by my examiners.

I understand that my thesis may be made electronically available to the public.

Abstract

The end-Devonian Hangenberg event represented one of the biggest Phanerozoic mass extinctions. However, the potential mechanism(s) for triggering this event, including climate cooling, sea-level change, glaciation and ocean anoxia, is still an ongoing subject of debate. In this study, geochemical paleoredox proxies (redox-sensitive trace metals as well as Mo and S isotopes) preserved in black shales of the Exshaw Formation were used to reconstruct local and global ocean redox conditions during the Hangenberg event.

The effect of hydrocarbon maturation on the paleoredox proxies was first assessed. Statistically, an unpaired t-test of S and Mo isotope data showed no significant difference between thermally immature, mature, and overmature samples. Large sulfur isotope fractionations (–15‰ to –65‰) between original seawater sulfate and pyrite is best explained by microbial sulfate reduction (MSR) during deposition and early diagenesis rather than thermochemical sulfate reduction (TSR). Hence, it suggested that the geochemical data were minimally affected by hydrocarbon maturation and retained their depositional signatures.

Eastern immature shales and central mature shales have a wide range of total organic carbon (TOC; 1.0–15.3 wt%; 2.2–19.3 wt%, respectively) and Mo (1.2–116.7 ppm; 18.3–129.3 ppm, respectively), U (2.4–44.5 ppm; 6.1–66.1 ppm, respectively), and Re (3.9–214.1 ppb; 11.2–316.0 ppb, respectively) concentrations, implying rapidly fluctuating redox conditions at each locality. By contrast, the stratigraphically higher shales from the western overmature area are marked by lower TOC (1.3–2.3 wt%) and trace metal contents (Mo: 1.3–23.5 ppm; U: 2.1–6.5 ppm; Re: 6.7–34.1 ppb), suggesting oxic to suboxic depositional conditions, whereas the stratigraphically lower shales have moderate trace metal enrichments (TOC: 1.3–3.5 wt%; Mo: 10.7–62.7 ppm; U: 5.5–20.7 ppm; Re: 21.5–89.3 ppb), indicating a suboxic to euxinic environment.

The basin restriction is no more than moderate, based on moderate Mo/TOC and Mo/U EF (enrichment factor) ratios.

The Mo isotope values in the most Mo-rich shales (most likely to be deposited from locally euxinic bottom waters) from the three areas range from 0.3‰ to 1.1‰. Samples with low δ^{98}Mo (0.3–0.4‰) have high V enrichments, suggesting the operation of an Fe-Mn particulate shuttle that delivered isotopically light Mo to sediments. Samples with lower V enrichments may record local seawater-sediment Mo isotope fractionation because of weakly euxinic conditions. Applying Mo isotope fractionation factors of 0.3–1.0‰, global seawater δ^{98}Mo at the Devonian-Mississippian boundary may fall in the range of 1.4‰ to 2.1‰. The Re and Mo enrichment data constrain the extent of anoxic and euxinic seafloor, respectively, to be <2% in both cases using mass-balance models. The Mo isotope mass-balance model suggests <5% euxinic seafloor. Hence, compared to modern ocean seafloor (anoxia: 0.35%; euxinia: 0.021–0.063%), the global ocean at the Devonian-Mississippian boundary likely had more anoxia/euxinia, particularly in intracratonic and continental margin regions, which may have contributed to the Hangenberg mass extinction.

Acknowledgements

I would like to express my gratitude towards my supervisor, Dr. Brian Kendall, for the opportunity to work on this project and his help throughout. Through countless discussions, Dr. Kendall offers his guidance in this scientific research. Without his patience and support, the outcome and success of this thesis could not be achieved. This research was supported by an NSERC Discovery Grant (RGPIN-435930) to Dr. Brian Kendall. The Metal Isotope Geochemistry Laboratory at the University of Waterloo was funded in part by the Canada Foundation for Innovation and the Ontario Research Fund.

I would like to thank the Alberta Core Research Centre in Calgary, for providing cores for sampling.

I would like to thank Dr. Gwyneth Gordon and Dr. Stephen Romaniello at Arizona State University, for helping to measure Mo isotope data.

I would like to thank lab manager Stephen Taylor at the University of Calgary, for helping to measure S isotope data.

I would like to thank our lab manager Dr. Liyan Xing, for her kind guidance, which ensured the smooth running of my lab work, especially for metal concentration measurements.

I would like to thank Dr. Chris Yakymchuk and Dr. Shaun Frape for being my committee members and their generous time, precious comments, and countless support.

I would like to thank my parents for their love and support during my graduate study.

I would like to thank my following colleagues and school mates for their help (including but not limited to): Facheng Gong, Alex Kunert, Jiangyu Li, Kai Liu, Xinze Lu, Shinong Mao, Xin Tong, Ryan Truong, Jieying Wang, Su Wang, Xiaomeng Xu, Tian Yu, Yan Zhang, and Jiabao Zhu.

Table of Contents

List of Figures

List of Tables

1. Introduction

Reconstruction of depositional environment, provenance, and diagenesis within ancient marine systems requires the use of multiple proxies, including redox-sensitive trace metals (Brumsack, 1980; Dean et al., 1997; Algeo and Lyons, 2006; Tribovillard et al., 2006; Scott et al., 2008; Weyer et al., 2008; Scott and Lyons, 2012; Reinhard et al., 2013; Chen et al., 2015; Scott et al., 2017; Armstrong et al., 2018). The Mo isotope system has been widely utilized as a proxy to evaluate Earth's ocean oxygenation conditions and biogeochemical evolution (Arnold et al., 2004; Algeo and Lyons, 2006; Scott et al., 2008; Dahl et al., 2010; Scott and Lyons, 2012; Reinhard et al., 2013; Chen et al., 2015; Kendall et al., 2015; Kendall et al., 2017; Cheng et al., 2018; Chen et al., 2019). In addition, mass balance models coupled with element concentrations (e.g., Mo, Re) are used to constrain the extent of ocean oxygenation (Dahl et al., 2011, Reinhard et al., 2013; Goldberg et al., 2016; Sheen et al., 2018). However, some post-depositional processes (e.g., burial diagenesis, thermal maturation) can potentially modify the chemical composition of black shales and alter the geochemical signature of these redox proxies. In a previous study, thermal maturation was shown to have minimal effect on the chemical composition of black shales (Mongenot et al., 1996). On the contrary, another study suggested the initial geochemical depositional signature of redox proxies in black shales was changed after hydrocarbon maturation (Ardakani et al., 2016). Thus, before using paleo-redox proxies for black shales that have undergone hydrocarbon maturation, it is important to first explore the effects of hydrocarbon maturation on geochemical data in black shales.

In this thesis, the effects of hydrocarbon maturation are further evaluated for the Exshaw Formation lower black shale member, which is located within the Western Canadian Sedimentary

Basin (WCSB) and deposited across the Devonian-Mississippian (D-M) boundary. In terms of thermal maturity, the Exshaw Formation can be divided into three areas from east to west: immature, mature, and overmature corresponding to burial temperature conditions below, at, and above the oil generation threshold (Fig. 1; Piggott and Lines, 1991; Selby and Creaser, 2003). Sulfur isotope analysis of early diagenetic pyrite and synsedimentary pyrite is utilized to understand sulfur cycling and local depositional environment (Gautier, 1986; Calvert et al., 1996; Lyons, 1997; Wei et al., 2016) as well as to differentiate microbial sulfate reduction (MSR) and thermochemical sulfate reduction (TSR) (Ardakani et al., 2016). In this thesis, the first objective is to assess the influence of hydrocarbon maturation on the redox-sensitive trace metal enrichments and Mo and S isotope compositions of the Exshaw Formation black shale member.

The Late Devonian (385–359 Ma) is one of the most prominent geological periods when some profound Phanerozoic mass extinction events occurred, such as the Givetian-Frasnian Taghanic event, the Frasnian-Famennian Kellwasser events, and the end-Devonian Hangenberg event (Sepkoski, 1986; Ryder, 1996; McGhee et al., 2013; Formolo et al., 2014). The Kellwasser crisis is the most severe and well-studied of the Devonian extinctions. It is marked by the extensive elimination of species, including those found in metazoan reef systems (Sorauf and Pedder, 1986; Copper, 2002) and benthic (e.g., trilobites, ostracods) and nektonic (e.g., ammonoids, tentaculites) marine communities (McGhee, 1996; Walliser, 1996; Ma et al., 2016; Huang et al., 2018). Several studies have been conducted to explore the potential causes for triggering the two (upper and lower) Kellwasser mass extinction events, including an expansion of global ocean anoxia (Joachimski and Buggisch, 1993; Becker and House, 1994; Bond et al., 2004; Carmichael et al., 2014, Wang, 2016), eustatic sea-level changes (Johnson et al., 1985; Chen and Tucker, 2004), ocean eutrophication (Murphy et al., 2000; Gong et al., 2002), volcanism (Courtillot et al., 2010; Racki et al., 2018), and climate change (Streel et al., 2000; Joachimski and Buggisch, 2002; Song et al., 2017; Huang et al., 2018; White et al., 2018).

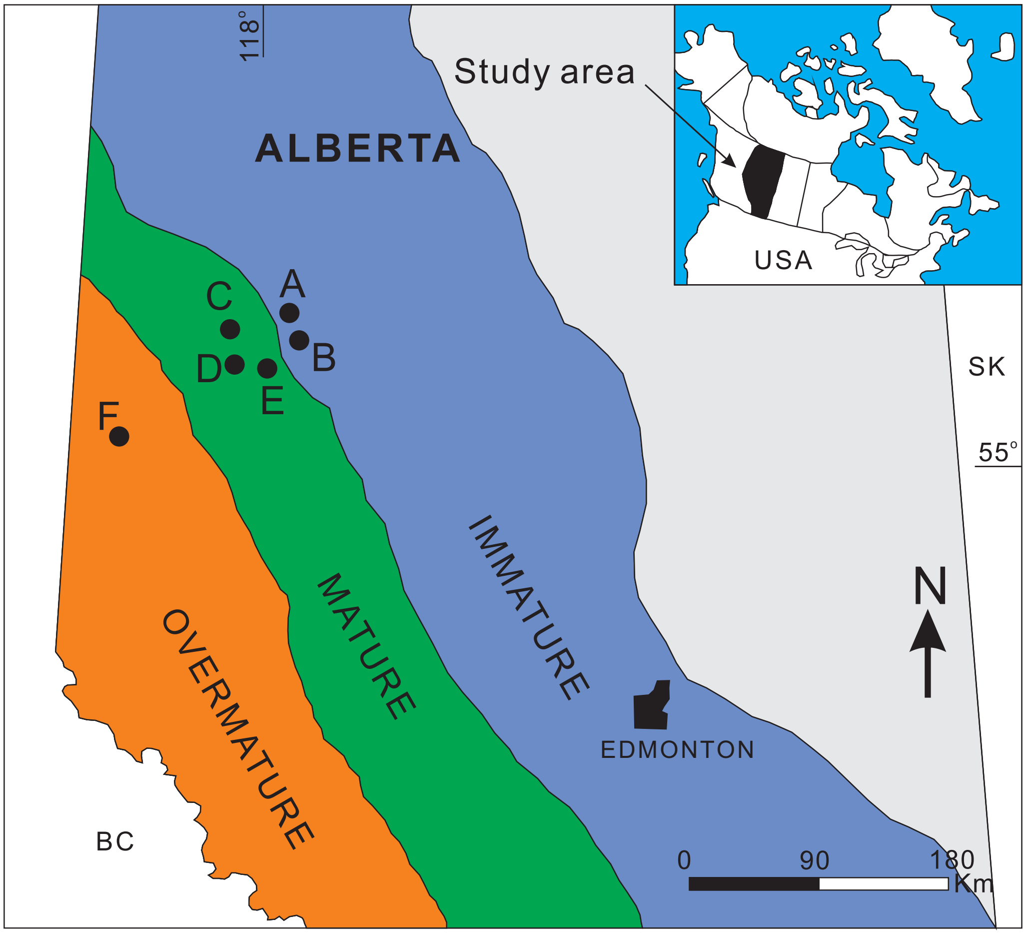

Fig. 1. Regional map showing the drill cores with Exshaw Formation black shales and the spatial extent of hydrocarbon thermal maturity levels throughout the study area (modified from Piggott and Lines, 1992; Creaser et al., 2002). Drill cores 13-18-180-23W5 (A) and 3-19-80-23W5 (B) are in the immature area. Drill cores 14-22-80-02W6 (C), 6-19-78-25W5 (D), and 8-29-78-01W6 (E) are in the mature area. Drill core 4-23-72-10W6 (F) is in the overmature area.

However, the following Famennian-Tournaisian (F-T) boundary Hangenberg mass extinction event is not as well studied as the Kellwasser events. The event caused ~20% elimination of marine invertebrate species and pelagic organisms as well as ~50% of vertebrates (Walliser, 1996; Sandberg et al., 2002; Scholze and Gess, 2017). The triggering mechanism(s) for the event is still being debated, including global cooling, glaciation, ocean anoxia, and possible volcanism. Expanded ocean anoxia/euxinia is one of the leading mechanisms to explain the extinction, based on the observation of sedimentary facies change and carbon cycle disturbance, which is supported by trace metal and oxygen and carbon isotope data (Brand et al., 2004; Kaiser, 2005; Buggisch and Joachimski, 2006; Kaiser et al., 2006, 2008; Marynowski and Filipiak, 2007; Trela and Malec, 2007; Cramer et al., 2008; Clark et al., 2009; Matyja et al., 2010, 2014; Day et al., 2011; Marynowski et al., 2012; Kumpan et al., 2013, 2014; Cole et al., 2015; Kaiser et al., 2016). A positive $\delta^{13}C$ excursion in the Late Devonian and Early Mississippian coincided with the occurrence of widespread black shales and are interpreted as the consequence of enhanced organic carbon burial (Walliser, 1996; Kaiser et al., 2006). However, some other studies suggest that the extent of ocean anoxia at the Famennian-Tournaisian boundary was not as expansive as previously thought. Dahl et al. (2010) suggested there was a high extent of ocean oxygenation (at least intermittently) in the Late Devonian based on the observation of high $\delta^{98}Mo$ in black shales. Kazmierczak et al. (2012) stated that the oxic conditions could be more expanded than previously thought in Famennian, based on the observation of mass occurrence of benthic cyanobacterial mats. Wallace et al. (2017) proposed that the evolution of vascular plants promoted extensive oxygenation of the Frasnian-Famennian atmosphere-ocean system, which is supported by negative cerium anomaly values (<0.6) in marine carbonates. Thus, the exploration of the local and global redox conditions at the F-T boundary is of significance to further understand the mechanism of the Hangenberg mass extinction event (359 Ma). Thus, the second objective of this thesis is to assess the local and global redox conditions and evaluate ocean anoxia/euxinia as the cause of the Hangenberg extinction event.

2. Geological setting

The Exshaw Formation, known for its critical stratigraphic horizon spanning the Famennian-Tournaisian boundary and its economic importance as an abundant hydrocarbon source rock in western Alberta (Leenheer, 1984; Creaney and Allan, 1991; Selby and Creaser, 2003; Warren and Cooper, 2017), was deposited within the Western Canada Sedimentary Basin (WCSB), which trends approximately northwest to southeast between the Western Cordillera and Canadian Shield and occupies an area of around 1.4×10^6 km^2 (Piggott and Lines, 1991; Robison, 1995; Creaser et al., 2002; Porter et al., 2014; Wang et al., 2018). The WCSB has been developed into two different phases over its evolutionary history (Podruski et al., 1988; Hiyagon and Kennedy, 1992). The first phase is dominated by Paleozoic to Jurassic carbonate strata on the stable craton proximal to the ancient passive margin of North America while the second phase includes mid-Jurassic to Paleocene clastic rocks deposited in a foreland basin (Podruski et al., 1988; Hiyagon and Kennedy, 1992; Pujol et al., 2017). Strata of the WCSB have undergone two major erosion events. The first one occurred from 150 Ma to 119 Ma, corresponding to the Sub-Mannville Unconformity and the second occurred during the Laramide Orogeny from 57.8 Ma to the present (Wang et al., 2018). In the Late Devonian, Western Canada was in an equatorial location facing Panthalassa and the Exshaw Formation was deposited in an epeiric sea along the western margin of Euramerica (Fig. 2; Witzke and Heckel, 1988; Savoy, 1990; Robison, 1995; Pratt and van Heerde, 2016).

Fig. 2. Paleogeographic map showing the ancient continents and oceans at the Late Devonian. The red star represents the Exshaw Formation (modified from Steptoe, 2012).

The Exshaw Formation extends from the outcrop in the thrust and fold belt of the Canadian Rockies eastward in the subsurface across Alberta and southern Saskatchewan (Robison, 1995). It is lithologically and stratigraphically equivalent to the Bakken Formation (Leenheer, 1984; Smith and Bustin, 2000). The Exshaw Formation consists of a Tournaisian upper member of siltstone to silty limestone and a lower member of Tournaisian calcareous as well as Famennian non-calcareous black shales, resting with minor disconformity upon the underlying Upper Devonian Palliser Formation. The disconformity results from a transgression onto the Alberta platform during the Late Devonian (Famennian) (Richards and Higgins, 1988; Meijer and Johnston, 1993; Caplan and Bustin, 1999; Richards et al., 1999; Selby and Creaser, 2003; Porter et al., 2014). At the Jura Creek area in western Alberta where the type section is located, the Exshaw Formation has a thickness of ~47 m (Richards and Higgins, 1988; Selby and Creaser, 2005). It consists of a 9.3 m thick lower member and a 37.4 m thick upper member, overlying marine carbonates of the Palliser Formation (Smith and Bustin, 2000; Selby and Creaser, 2005). The lower member is characterized by 1–6 cm basal sandstone-conglomerate, 6.9 m of non-calcareous to calcareous black shale and 2.4 m of calcareous black shale, while the upper member consists of predominantly siltstone (~37.4 m).

The upper member siltstone to silty limestone member of the Exshaw Formation was interpreted to be deposited under a shallowing and regressing sea (Savoy, 1990; Robison, 1995). By comparison, it was suggested that the Exshaw Formation lower member black shales were deposited below storm wave base at a water depth shallower than 300 m (Richard and Higgins, 1988; Robison, 1995). Based on high biogenic silica, phosphate and organic carbon contents, it was suggested that the Exshaw shales were deposited within an upwelling zone which extended along the western margin of the craton (Macdonald, 1985; Richards and Higgins, 1988; Robison, 1995).

Stasiuk and Fowler (2004) defined five petrographic organic facies (I–V) for the Exshaw Formation based on their assemblages of alginites, acritarchs, sporinites, siliceous microfossils and algal mat microtextures. Specifically, organic facies I–V represent different depositional conditions. Organic facies I, II (prasinophyte alginites and acritarchs) and III (coccoidal alginite) suggests sediment deposition in relatively deep basin, intermediate shelf platform and lagoonal shallow waters, respectively. Organic facies IV, defined by siliceous microfossils, represents an upwelling zone which extended into intracratonic and epicontinental settings. Organic facies V (stromatolitic microtexture with/without coccoidal alginite) represents shallow water in restricted shelf to lagoonal settings. The Exshaw Formation is dominated by organic facies IV in the west and organic facies III in south-eastern Alberta between 110ºW to 113ºW, in accordance with its depositional setting of an epicontinental sea (Stasiuk and Fowler, 2004).

The lower member black shales in the Exshaw Formation are characterized by a large range of total organic carbon (TOC; 1.6–20 wt%), but most shales have 2–4% TOC (Caplan and Bustin, 1999; Creaser et al., 2002). Total sulfur from the Exshaw shales in the Peace River Arch area range from 0.7 to 4 wt% (Leventhal, 1987; Berner and Raiswell, 1983; Richards and Higgins, 1988). Trace metals such as Ni, V, Zn, Pb, Re, Os, Mo, and U are enriched in the Exshaw black shales (Duke, 1983; Creaser et al., 2002; Selby and Creaser, 2003). Lower member shales are typically planar laminated, brownish to black, and calcareous to slightly or non-calcareous. Conodont biostratigraphy records the depositional age (Selby and Creaser, 2003, 2005). In southwestern Alberta (~51ºN, 115ºW), conodont species *Polyganthus communis* and *Siphonodella cooperi* (Fig. 3; MacQueen and Sandberg, 1970; Higgins et al., 1991; Savoy and Harris, 1993) were found in the uppermost part of the lower black shale unit, which occurs from Upper *Siphonodella duplicata* Zone upward into the Upper *Siphonodella crenulata* – *Siphonodella isoticha* Zone and thus represents Early Tournaisian time (Macqueen and Sanberg, 1970; Savoy and Harris, 1993; Selby and Creaser, 2003). Moreover, *S. duplicate* conodont species, occurring between the *duplicate* Zone and Lower *S. crenulata* Zone (Fig. 3; Sandberg et al., 1978; Richards et al., 1999), were present in lower member black shales from the middle of Alberta (~ 54ºN, ~118ºW). Thus, the

Exshaw Formation lower member black shales were deposited between the *expansa* and *duplicate* Zones, corresponding to Late Famennian to Early Tournasian time (Richards et al., 1999; Creaser et al., 2002), which span the time of the occurrence for the Hangenberg event (~359 Ma) (Myrow et al., 2014; Scholze and Gess, 2017). The D-M boundary is constrained by the presence of the conodont *Siphonodella sulcate* (Paproth, 1980). Although it has not been observed in the Exshaw Formation, the boundary is suggested to be placed at the contact of the two types of black shale (calcareous and non-calcareous) (Richards and Higgins, 1988; Selby and Creaser, 2005).

Depositional age of the Exshaw Formation was given by previous geochronological studies. Richards et al. (2002) suggested a depositional age of 363.3 ± 0.4 Ma for the Exshaw lower member black shales from U-Pb monazite geochronology on a tuff unit close to the base of the black shale member. This age is consistent with the U-Pb zircon age (363.6 ± 1.6 Ma) of volcanic units within the Upper *expansa* Zone in New Brunswick (Tucker et al., 1998). Trapp et al. (2004) calculated an age of 360.7 ± 0.7 Ma for the D-M boundary by interpolation of U-Pb zircon dates. Selby and Creaser (2005) determined the D-M boundary age to be 361.3 ± 2.4 Ma by Re-Os geochronology of the Exshaw Formation black shales. Therefore, the depositional age for the black shales in the Exshaw Formation (lower member) is constrained between 363 and 360 Ma (Tucker et al., 1998; Creaser et al., 2002).

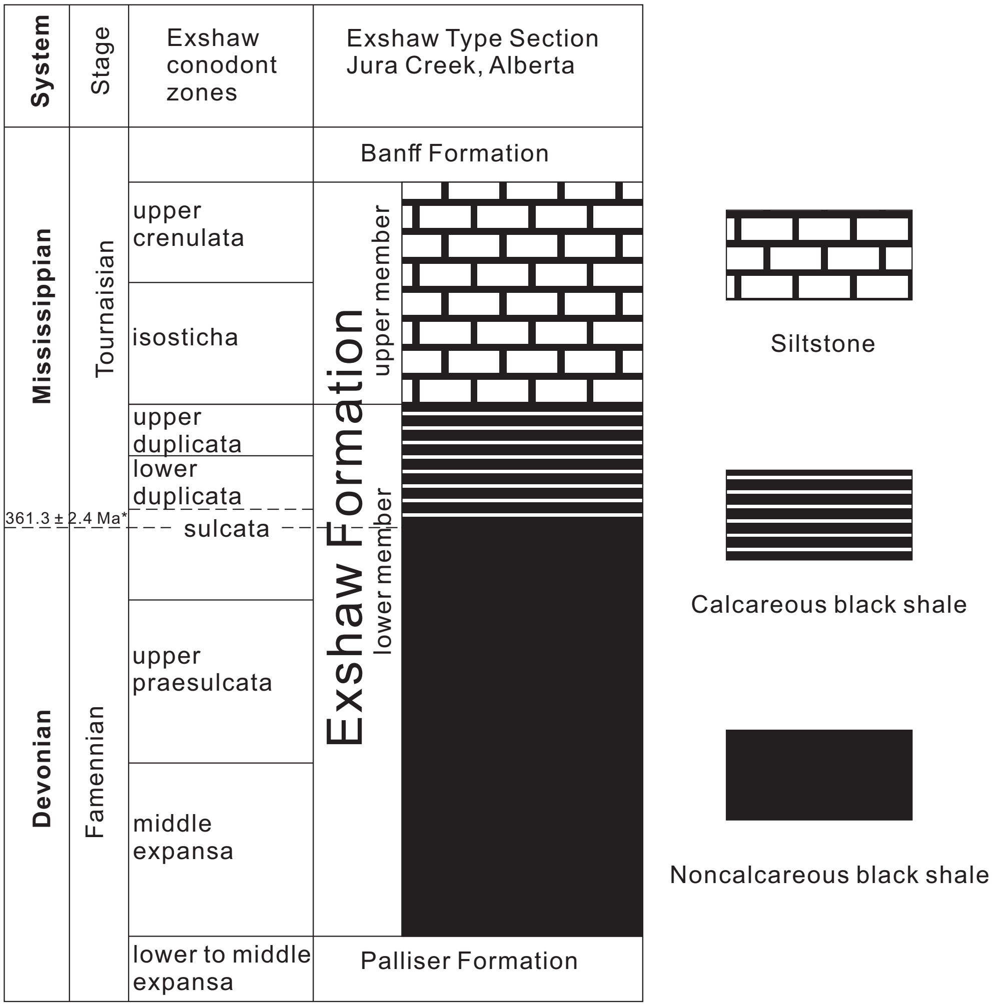

Fig. 3. Stratigraphic column of the Exshaw Formation. Dashed line denotes the Devonian–Mississippian boundary. "*" represents Re-Os age (modified from Selby and Creaser, 2005).

The maturity levels for the Exshaw Formation were determined by Rock-Eval pyrolysis (Creaser et al., 2002). Burial temperatures necessary for hydrocarbon maturation in the Exshaw Formation increased westwards from maturity levels of immature to overmature (immature-pressure and temperature below the oil generation threshold; mature-within oil generation window;

overmature-above the oil generation threshold; Piggott and Lines, 1991). The boundaries between thermal maturity zones are roughly parallel to the Cordilleran orogenic front (Piggott and Lines, 1991; Creaser et al., 2002; Selby and Creaser, 2003). In the Eocene, the Western Canada Sedimentary Basin reached maximum burial depths and subsequent uplift and erosion followed.

Other previous geochemical analyses were also conducted on the Exshaw Formation. High hydrogen index (HI), low Oxidation Index (Ox.I.), bulk organic carbon isotopes and bulk rock nitrogen isotopes were analyzed by Caplan and Bustin (1999) to verify the influence of the palaeoceanographic factors on organic matter preservation. They concluded that laminated mudrocks were deposited under eutrophic conditions with high primary production. In Porter et al. (2014), four immature black shale samples in the Exshaw Formation were collected from drillcore 3-19-80-23W5 (detailed in Piggott and Lines, 1992 and Creaser et al., 2002) and analyzed for trace metal abundance. Relatively high Ni/Co values (13.8 to 21.4) indicated the black shales were deposited under suboxic to anoxic conditions (Porter et al., 2014). In addition, although V/(V + Ni) ratios are not consistently reliable as a redox proxy, in this case, high V/(V + Ni) ratios (averaging ~0.68) showed agreement with the suboxic to anoxic conditions (Porter et al., 2014). However, there is an exception for V/Cr ratios. Two samples (SP10-10 and SP13-10) with high V/Cr values (7.2 and 9.0, respectively) suggest suboxic-anoxic conditions, whereas the other two samples (SP8-10 and SP9-10) with low V/Cr ratios (2.0 and 2.1, respectively) suggest dysoxic conditions (Porter et al., 2014).

3. Geochemical background on redox-sensitive trace metals, Mo isotopes and S isotopes

3.1 Trace metals

3.1.1 Molybdenum abundances

Molybdenum and its isotopes are widely used as paleoredox proxies to evaluate the extent of euxinia in ancient oceans (Arnold et al., 2004; Algeo and Lyons, 2006; Scott et al., 2008; Dahl et al., 2010; Scott and Lyons, 2012; Reinhard et al., 2013; Chen et al., 2015; Kendall et al., 2015; Kendall et al., 2017). The major source of ocean Mo is from the transportation of the stable species molybdate (MoO_4^{2-}) from rivers. Molybdenum is characterized by its long oceanic residence time (~440 kyr) and conservative behavior under oxygenated water conditions (Miller et al., 2011). Ferromanganese crusts and nodules can scavenge minor amounts of Mo by the process of adsorption and co-precipitation in oxic deep waters, which is a slow process due to the slow rate of sedimentation (Morford and Emerson, 1999; Scott et al., 2008). Molybdate (MoO_4^{2-}) preferentially converts to thiomolybdate ($MoO_{4-x}S_x^{2-}$) when there are sulfidic conditions in sediment pore waters or in the water column (Dahl et al., 2013). If $[H_2S]_{aq}$ is greater than 11 µM, molybdate will ultimately convert to tetrathiomolybdate (MoS_4^{2-}) as well as reactive Mo-polysulfide species with the reactions with zero-valent sulfur and then these species can be captured by Fe-sulfide minerals, clay minerals and organic matter (Erickson and Helz, 2000; Helz et al., 2011; Dahl et al., 2013). Chappaz et al. (2014) stated that pyrite should be viewed as a nontrivial sink but not the primary host for Mo in euxinic settings. Dahl et al. (2017) stated that Mo can be scavenged from natural sulfidic waters by organic matter without an Fe-assisted pathway. By contrast, Helz and Vorlicek (2019) proposed that Mo can be captured by sulfide during the sulfate reduction process rather than by organic ligands.

Black shales contain relatively high Mo concentrations (10s to 100s ppm) compared to the continental crust (~1.5 ppm; Taylor and McLennan, 1995; Scott et al., 2008). Based on data from modern marine organic-rich sediments, although bulk Mo concentrations in black shales can be influenced by several factors such as global ocean redox state and degree of basin restriction, they are used to track the depositional environment. To be specific, low Mo concentrations (<25 ppm) suggests the restriction of H_2S to sediment pore waters, and the overlying bottom waters were suboxic to oxic (the lowest concentrations reflect well-oxygenated conditions). By contrast, relatively high Mo concentrations (>100 ppm) indicate that the bottom waters were persistently euxinic. Moderate Mo concentrations (25–100 ppm) implies bottom waters were suboxic to euxinic, depending on many local factors such as basin restriction, sedimentation rates, pH, and an Fe-Mn particulate shuttle (Scott and Lyons, 2012; Scholz et al., 2017). A higher Mo concentration in seawater indicates a relatively high extent of ocean oxygenation. On the contrary, a lower seawater Mo concentration suggests expanded ocean anoxia/euxinia.

3.1.2 Uranium abundances

In nature, uranium exists as either a reduced state [U(IV)] or an oxidized state [U(VI)]. U(IV) efficiently precipitates from reducing sediment pore waters as UO_2 (Anderson et al., 1989), whereas U(VI) is soluble in oxygenated waters. As the most important species of dissolved U(VI) in oxygenated seawater, the uranyl carbonate anion ($UO_2[CO_3]_3^{4-}$) behaves conservatively in the water column (Langmuir, 1978). Compared to the ocean mixing time of ~1.5 kyr (Scott et al., 2008), the long U residence time (~400–500 kyr; Ku et al., 1977; Dunk et al., 2002) leads to a globally homogeneous U concentration and isotope composition in seawater. Similar to Mo, the source of U in oceans is mainly from transportation of dissolved U(VI) via rivers. Multiple major U marine sinks exist, such as biogenic carbonates and sediments deposited beneath low-oxygen and anoxic seawater (Morford and Emerson, 1999; Dunk et al., 2002; Partin et al., 2013).

Sediments under well-oxygenated bottom waters and hydrothermal alteration of oceanic crust are minor sinks for U (Morford and Emerson, 1999; Dunk et al., 2002; Partin et al., 2013; Kendall et al., 2015; Yang et al., 2017).

The removal of U in anoxic basins mainly occurs below the sediment-water interface but not in the water column (Anderson et al., 1989; Barnes and Cochran, 1990). Reduction and removal of U to anoxic sediments does not require dissolved H_2S like Mo, but relies on both metal-reducing bacteria (MRB) (Morford and Emerson, 1999; Morford et al., 2005; Tribovillard et al., 2006; Algeo and Tribovillard, 2009; Stylo et al., 2015) and common abiotic reductants, such as Fe (II) (Brown et al., 2018). Like Mo, a higher seawater U concentration indicates a relatively high extent of ocean oxygenation whereas a lower seawater U concentration suggests expanded ocean anoxia and depletion of U in seawater via U burial in shales (Partin et al., 2013).

3.1.3 Rhenium abundances

Sinks for Re removal are subdivided into oxic, suboxic and anoxic settings. There is a considerable difference between the Re accumulation rate in sediments beneath anoxic waters versus well-oxygenated bottom waters (Colodner et al., 1993; Crusius et al., 1996; Morford and Emerson, 1999; Morford et al., 2005; Morford et al., 2012; Sheen et al., 2018). Compared to Cr and U, which are also used as paleoredox proxies, Re is more sensitive to low oxygenation conditions because the enrichment of authigenic Re in organic-rich mudrocks is considerably higher than the detrital background (Sheen et al., 2018). Thus, the enrichment of Re in organic-rich mudrocks could provide some novel insights on global ocean redox conditions. In the modern oceans, the source of Re is mainly from oxidative weathering of sulfide minerals in the upper continental crust (Colodner et al., 1993; Miller et al., 2011), and Re primarily exists as the soluble perrhenate oxyanion ReO_4^- in oxygenated seawater (Anbar et al., 1992; Colodner et al., 1993). In an anoxic water column with both high and low levels of dissolved H_2S, Re is efficiently removed into sediments. By contrast, Re is less enriched in reducing sediments that are overlain by mildly oxygenated bottom waters (Crusius et al., 1996; Morford and Emerson, 1999; Morford et al., 2005). In oxic settings, the enrichment of Re in sediments is low and Re adsorption onto Fe-Mn oxides is minimal (Colodner et al., 1993). Similar to U, a higher seawater Re concentration indicates a relatively high extent of ocean oxygenation whereas a lower seawater Re concentration points to expanded ocean anoxia.

3.1.4 Vanadium abundances

Vanadium in nature exists as three oxidation states: V(III), V(IV), and V(V) (Wanty and Goldhaber, 1992). In aqueous solution, V(III) is hydrolyzed and converted to insoluble V(III) oxyhydroxides rapidly and completely. V(IV) and V(V) are two soluble forms of vanadium in nature and exist as oxocation VO^{2+} and oxyanions ($H_nVO_4^{n-3}$) in waters, respectively (Wanty and Goldhaber, 1992). Owing to its distinct chemical behavior in various conditions, V can be used to infer redox conditions in modern and ancient environments (Breit and Wanty, 1991; Wanty and Goldhaber, 1992). Previous studies linked V enrichments to the accumulation of excess H_2S in sediments and bottom waters (Lewan and Maynard, 1982; Lewan, 1984; Breit and Wanty, 1991; Wanty and Goldhaber, 1992). In Scott et al. (2017), it was proposed that a sediment V concentration of over 500 ppm should be regarded as “hyper-enriched” and reflects “hyper-sulfidic” bottom water conditions (H_2S >10 mM). However, the V abundance in the Framvaren Fjord deep basin, which has the highest H_2S concentration (8 mM) in modern marine setting, is low (averaging 41 ppm). Thus, the understanding of V enrichment in sediments still needs further exploration.

However, if local H_2S activity is indeed critical for the reduction for V(IV) to V(III) and hyper-enrichment of V in black shales, the content of H_2S in coeval bottom waters/pore-waters should be at least 8 mM (Scott et al., 2017). A high flux of Fe-Mn oxides to the sediment-water interface could further accelerate the enrichment of V in anoxic sediments. In anoxic waters, vanadate is reduced to the vanadyl form (VO^{2+}) as the Mn oxides are reduced to Mn^{2+}, and then efficiently removed to the sediments (Emerson and Huested, 1991). With the presence of oxygen in bottom waters, vanadium could escape to the overlying waters (Emerson and Huested, 1991; Zhang et al., 2016). Based on the observation of modern oceans, V is usually enriched together with Mo and U in euxinic basins (Nameroff et al., 2002; Scholz et al., 2011; Zhang et al., 2016). Overall, V is enriched in sediments deposited from anoxic bottom waters but not in sediments deposited under oxygenated depositional conditions.

3.1.5 Mo enrichment factor (EF) and U enrichment factor (EF)

Molybdenum-uranium covariation is associated with specific attributes and processes of the depositional system. Algeo and Tribovillard (2009) stated three patterns of authigenic molybdenum-uranium covariation in specific marine environmental conditions and processes (Fig. 4): (1) redox variation, (2) Fe-Mn particulate shuttle, and (3) evolving watermass chemistry. In unrestricted open-ocean systems characterized by suboxic bottom water conditions, the accumulation rate of U_{auth} (as authigenic U) is superior to that of Mo_{auth} (as authigenic Mo), resulting in low sediment $(Mo/U)_{auth}$ ratios relative to modern seawater (Mo/U). With more reducing bottom water conditions, authigenic enrichment of both Mo and U in sediments becomes strong and thus cause Mo/U EF ratios in sediment equal or even higher relative to the Mo/U ratio of seawater due to more efficient removal of Mo than U, especially in euxinic settings. Euxinic sediments in the Cariaco Basin, where there is operation of a particulate Mn-Fe oxyhydroxide shuttle, are characterized by even higher enrichment of Mo_{auth} than U_{auth} due to the efficient uptake of Mo but limited uptake of U onto Mn-Fe oxides. In the Black Sea, which is highly restricted with respect to water exchange with the open ocean, euxinic sediments have a Mo/U EF ratio that is only ~0.04 of the open ocean seawater Mo/U ratio due to the faster rate of Mo removal than U to sediments without adequate resupply and hence Mo is drawn down from the Black Sea bottom waters (Algeo and Tribovillard, 2009).

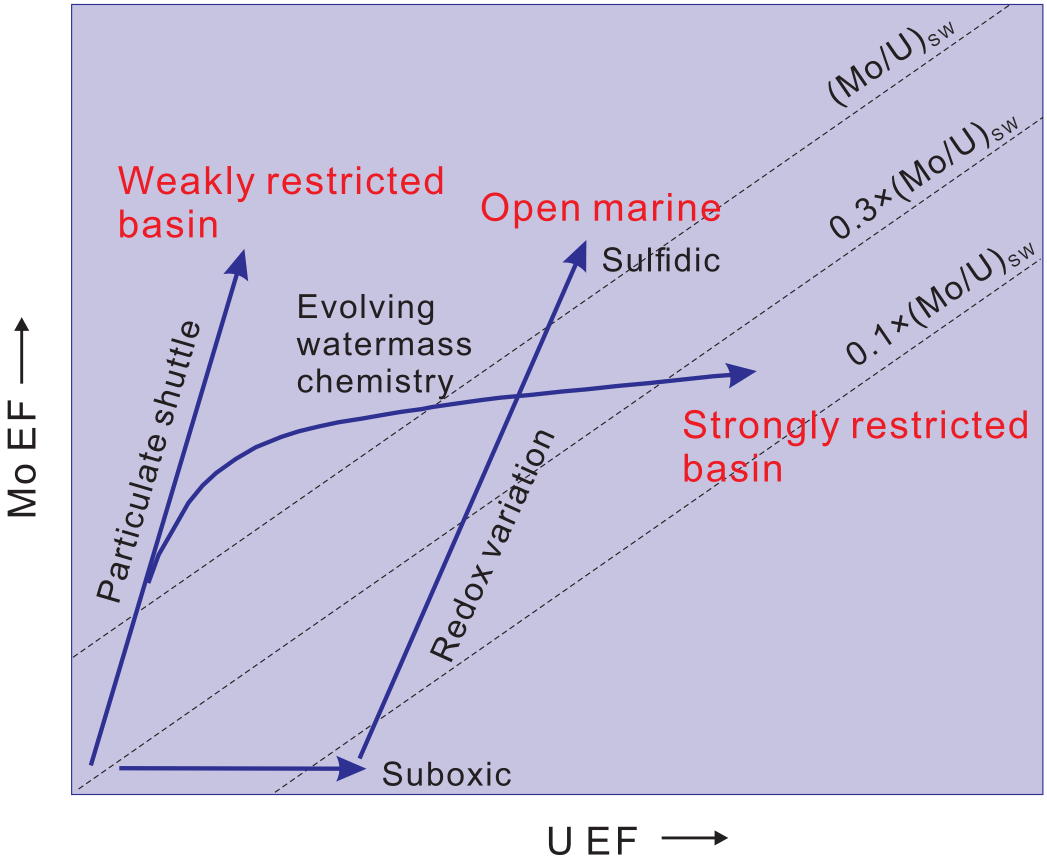

Fig. 4. Three patterns of authigenic molybdenum-uranium covariation. The dashed lines refer to seawater Mo/U EF ratios (modified from Algeo and Tribovillard, 2009).

3.1.6 Mo/TOC ratios

Basin restriction has a significant impact on Mo concentrations in organic-rich sediments. Since Mo and TOC are usually associated and correlated with each other in modern organic-rich sediments deposited from euxinic bottom waters, the Mo/TOC ratio in ancient euxinic black shales (those having well-correlated Mo and TOC contents) can be used to evaluate the extent of basin restriction (Algeo and Lyons, 2006). The Mo/TOC ratio records the uptake rate of Mo per unit organic matter, which reflects the aqueous Mo concentrations in euxinic deep waters. High Mo/TOC ratios from euxinic sediments occur when there is a relatively open ocean basin. This is because the recharge rate of Mo to the bottom waters (i.e., dissolved Mo entering the basin from the open ocean) keeps balance with the removal rate of Mo to the euxinic sediments (Algeo and Lyons, 2006). By contrast, euxinic organic-rich sediments deposited in a strongly restricted basin yield a relatively low Mo/TOC ratio due to the depletion of aqueous Mo, reflecting a low Mo recharge rate (Algeo and Lyons, 2006). As modern analogues, the Black Sea, Cariaco Basin, and Saanich Inlet correspond to strong, moderate, and weak basin restriction, respectively, and the organic-rich sediments in these basins yield average Mo/TOC ratios of 4.5 ± 1 ppm/wt%, 25 ± 5 ppm/wt%, and 45 ± 5 ppm/wt%, respectively (Algeo and Lyons, 2006). Basin restriction exerts some control on the extent of sulfidic conditions. The Black Sea deep water is interpreted as a strongly euxinic marine condition ($[H_2S]_{aq} > 11\ \mu M$) whereas the Cariaco Basin deep water is a weakly euxinic marine environment ($[H_2S]_{aq} < 11\ \mu M$) (Algeo and Lyons, 2006; Algeo and Tribovillard, 2009). Much of the Saanich Inlet deep basin is seasonally anoxic/euxinic and the deep-water layer is characterized by $[H_2S]_{aq} < 25\ \mu M$ (Algeo and Lyons, 2006).

3.2 Mo isotopes

The average δ^{98}Mo of the modern global ocean is 2.34 ± 0.10‰ (relative to NIST SRM 3134 = 0.25‰; Barling et al., 2001; Nakagawa et al., 2012; Nägler et al., 2014), which is a high value compared to the average δ^{98}Mo from river and groundwater inputs (~0.55‰; Neely et al., 2018). When bottom waters are strongly euxinic ($[H_2S]_{aq}$ >11 μM), quantitative conversion of molybdate (MoO_4^{2-}) to tetrathiomolybdate (MoS_4^{2-}) as well as near-quantitative removal of Mo from bottom waters in a semi-restricted basin can result in the preservation of seawater δ^{98}Mo in sediments, like that observed in the Black Sea, marine Lake Rogoznica (Adriatic Sea), and Kyllaren Fjord (Norway) (Barling et al., 2001; Arnold et al., 2004; Neubert et al., 2008; Noordmann et al., 2015; Bura-Nakic et al., 2018). Considering the ocean mixing time of ~1.5 kyr (Scott et al., 2008) and long residence time of Mo (~440 kyr; Miller et al., 2011), the δ^{98}Mo of ocean waters is mixed homogeneously. Then, δ^{98}Mo in euxinic sediments from some severely semi-restricted basins may approximately represent global seawater δ^{98}Mo; thus, seawater δ^{98}Mo has been widely used as a proxy of global ocean redox conditions, particularly the extent of ocean euxinia.

However, Mo isotope fractionation in euxinic marine environments may occur by various processes (Fig. 5). Even if there is a strongly euxinic bottom water condition, a small Mo isotope fractionation (Δ^{98}Mo = ~0.5 ± 0.3‰) potentially could occur between dissolved Mo (MoO_4^{2-}) and authigenic solid Mo (Nägler et al., 2011; Anderson et al., 2018). In addition, Bura-Nakic et al. (2018) suggested that the offset between dissolved Mo and authigenic solid Mo could be ~0.3‰, based on the observation of deep water in the marine Lake Rogoznica at high sulfide concentrations. This is because several factors such as pH, sulfur speciation and $[H_2S]_{aq}$ could affect the rate of Mo removal to sediments, and may cause non-quantitative Mo removal from bottom waters. For $[H_2S]_{aq}$ concentrations <11 μM (weakly euxinic conditions), there is a large range of Mo isotope fractionation (<1‰ in the deep Cariaco Basin; up to 3‰ in the shallower part of the Black Sea below the chemocline) between seawater and sediments. This larger fractionation probably can be ascribed to the incomplete conversion of molybdate to tetrathiomolybdate, and hence the preservation of intermediate thiomolybdate complexes (Arnold et al., 2004, 2012; Neubert et al., 2008; Dahl et al., 2010; Nägler et al., 2011; Azrieli-Tal et al., 2014).

Other than some weakly euxinic settings, the magnitude of Mo isotope fractionation associated with Mo burial in sediments is larger in non-euxinic compared to euxinic environments. A consistently large Mo isotope fractionation of 3‰ takes place during the adsorption of isotopically light Mo from bottom waters onto Mn-oxides in sediments deposited from well-oxygenated bottom waters (Barling et al., 2001; Poulson Brucker et al., 2009). By contrast, a relatively stable Mo isotope fractionation of 0.7‰ is observed under weakly oxygenated and anoxic/non-sulfidic conditions along continental margins (Siebert et al., 2006; Poulson et al., 2006). In sediments deposited from mildly oxygenated bottom waters, the δ^{98}Mo is intermediate between well-oxygenated to weakly oxygenated conditions (Siebert et al., 2006; Poulson Brucker et al., 2009; Goldberg et al., 2012).

High seawater Mo concentrations and δ^{98}Mo values indicate a relatively greater extent of global ocean oxygenation. By contrast, low seawater Mo concentrations and δ^{98}Mo suggest expanded ocean euxinia (Barling et al., 2001; Arnold et al., 2004; Scott et al., 2008). Considering the possibility of isotope fractionation between seawater and euxinic sediments, δ^{98}Mo in black shales can represent a minimum value for seawater δ^{98}Mo. To be specific, high Mo concentrations and low δ^{98}Mo in black shales suggest a weakly euxinic environment and/or enhanced delivery of Mo to sediments via an Fe-Mn particulate shuttle which could promote Mo_{auth} accumulation and deliver isotopically light Mo to sediments, both of which result in pronounced seawater-sediment

Mo isotope fractionation (Herrmann et al., 2012; Kendall et al., 2015). On the contrary, low Mo concentrations and low δ^{98}Mo in black shales point to expanded ocean euxinia.

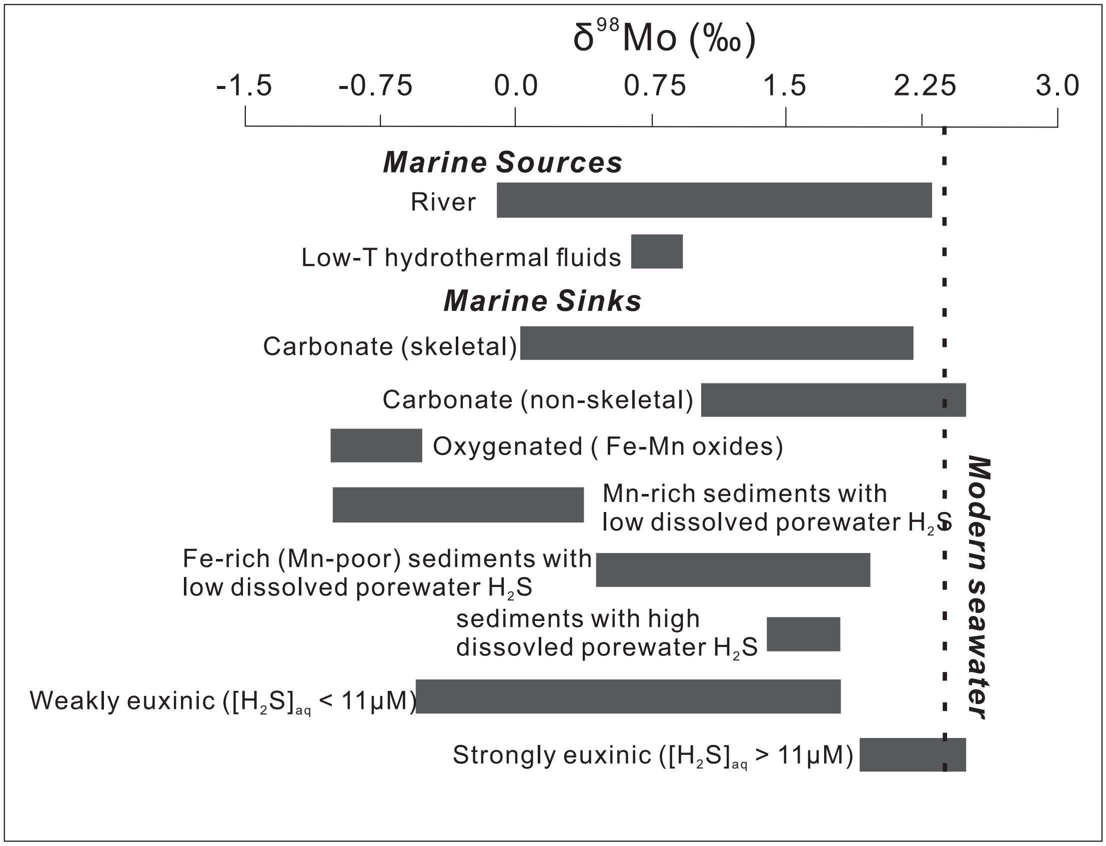

Fig. 5. Major sources and sinks for oceanic Mo and their Mo isotope compositions (modified from Kendall et al., 2017).

3.3 Pyrite sulfur isotopes

The sulfur isotope analysis of early diagenetic pyrite can provide critical information such as isotopic fractionation, sulfur cycling and reconstruction of the depositional environment (Gautier, 1986; Calvert et al., 1996; Lyons, 1997; Wei et al., 2016). Sulfur is buried as metal sulfides and/or organo-sulfur complexes in organic-rich sediments. Both inorganic and microbial sulfate reductions can yield ^{34}S-depleted sulfide and ^{34}S-enriched residual sulfate. Microbial sulfate reduction (MSR) and thermochemical sulfate reduction (TSR) are two common redox reactions which could form sulfide and pyrite in diagenetic environments. Generally, MSR is characterized by large sulfur isotope fractionation (up to –60‰) between seawater sulfate and H_2S, depending on the type of bacteria (Canfield, 2001; Amrani, 2014). The extent of isotope fractionation during microbial sulfate reduction is related to the rate of sulfate reduction. The largest sulfur isotope fractionation occurs at lower rates of sulfate reduction (Harrison and Thode, 1958; Kaplan and Rittenberg, 1964; Habicht and Canfield, 1997, 2001; Canfield, 2001). Sulfur isotope fractionation decreases as rates of sulfate reduction increase, and eventually becomes rate-independent (Habicht and Canfield, 1997). By contrast, TSR, as the redox reaction involving sulfate reduction and organic matter oxidation at relatively high temperatures (i.e., $80 < T < 200^{\circ}C$; Orr, 1997; Machel et al., 1995; Cross et al., 2004), leads to a much smaller degree of sulfur isotopic fractionation (−15‰ to −10‰). It is temperature dependent at 150 to 200ºC (Krouse et al., 1988; Machel et al., 1995) and kinetically slow and insignificant below 100ºC (Kiyosu and Krouse, 1990).

Sulfur isotopes and its fractionation can provide insights on local marine redox conditions. Low sulfur isotope fractionation values (<22‰) reflect limiting sulfate concentrations (closed porewater-seawater sulfate system), while high isotope fractionation values (>22‰) reflect a sufficient sulfate supply (i.e., an open system) (Habicht and Canfield, 1997). Oxygenated conditions can cause positive $\delta^{34}S$ values in pyrite. The increase of oxygen concentrations in bottom water causes deepening of the oxic-anoxic interface in the sediments (Núñez-Useche et al., 2016). Furthermore, it also isolates the porewater from the overlying water column and limits the sulfate supply in a closed system, corresponding to heavy $\delta^{34}S$. This is also consistent with the pyrite morphology that euhedral pyrites are associated with heavy $\delta^{34}S$ (Wei et al., 2016). The euhedral pyrites potentially record pyrite precipitation within the sediments at considerably slow rate and occurs during the late stage of early diagenesis in sulfide-depleted porewater (Raiswell, 1982; Coleman and Raiswell, 1995). Additionally, sulfur diffusion is an additional source of sulfide and could cause comparative depletion in ^{34}S in silled basins (Lyons, 1997). Gomes and Hurtgen (2015) stated that the sulfur isotope difference ($\Delta^{34}S$) between sulfates and sulfides is associated with sulfate concentrations. Under high sulfate conditions (>10 mM), the influence of the sulfate reservoir effect is limited and $\Delta^{34}S$ indicate biological and environment controls, whereas $\Delta^{34}S$ display positive correlations with sulfate concentration under low sulfate concentrations (<5 mM). Moreover, pyrite sulfur isotope fractionation could be affected by sedimentation rate. Slow sedimentation could increase the exchange between porewater and underlying seawater and cause large biological sulfur fractionation in an open system, whereas a rapid sedimentation rate would lead to limited fractionation in a closed system (Liu et al., 2019).

4. Methodology

4.1 Sampling

A total of 58 samples of organic-rich black shales from the Exshaw Formation were obtained from the Alberta Core Research Centre, Calgary, Alberta. Multiple samples were collected from six previously drilled cores which covered the hydrocarbon immature, mature, and overmature areas, with a lateral scale of >150 km. The number of samples taken from each core depended on the thickness of the Exshaw Formation, lithology, and quality of core preservation (i.e., stratigraphically intact core versus disaggregated core material). Eight samples were obtained from core 3-19-80-23W5 (immature zone), 8 samples from core 13-18-80-23W5 (immature zone), 3 samples from core 8-29-78-01W6 (mature zone), 6 samples from core 14-22-80-02W6 (mature zone), 7 samples from core 6-19-78-25W5 (mature zone), and 26 samples from core 4-23-72-10W6 (overmature zone). To reconstruct redox conditions during deposition and limit the influence of diagenesis, all samples were taken from the inner part of the core, avoiding obvious carbonate/quartz interbeds/veins and late diagenetic macroscopic pyrite nodules (Fig. 6). Each shale was broken to chips and crushed into fine powder using an automated ball mill machine (agate jars and balls) at the University of Waterloo. Total organic carbon content (TOC), major, minor, and trace metal abundances, Mo isotope compositions, and S isotope compositions were analyzed.

3-19-80-23W5 13-18-80-23W5 14-22-80-02W6

6-19-78-25W5 8-29-78-01W6 4-23-72-10W6

Fig. 6. Drill cores for the Exshaw Formation and representative black shale samples for each core. Drill cores 3-19-80-23W5 (A) and 13-18-80-23W5 (B) are in the immature zone. Drill cores 14-22-80-02W6 (C), 6-19-78-25W5 (D), and 8-29-78-01W6 (E) are in the mature zone. Drill core 4-23-72-10W6 (F) is in the overmature zone.

4.2 Total organic carbon measurements

Total organic carbon (TOC) contents of the samples were measured at the Agriculture and Food Laboratory, University of Guelph. The TOC content of a sample is calculated as the difference between total carbon (TC) and total inorganic carbon (TIC) contents of that sample. Firstly, sample powder was ashed at 475ºC for 3 hours in order to remove organic matter. Then, samples were analyzed using catalytic combustion at 960ºC on an Elementar Vario Macro Cube CN combustion analyzer. Inorganic carbon components were separated from other gases and measured by using thermal conductivity detection. Total carbon contents were quantified on a separate split of sample powder at 960ºC without ashing. Instrument accuracy was evaluated by two measurements of the United States Geological Survey (USGS) standard SBC-1, which yielded TOC values of 1.36 wt% and 1.37 wt%, respectively (the certified value is 1.23 ± 0.02 wt%; 1SD).

4.3 Elemental concentration measurements

Elemental concentration measurements were carried out at the Metal Isotope Geochemistry Laboratory, Department of Earth and Environmental Sciences, University of Waterloo. The analytical protocols used in this study are followed in Kendall et al. (2009), and are briefly summarized here.

A known amount (~100 mg) of sample powder was ashed overnight at 550ºC in crucibles to destroy organic matter. In a clean laboratory, the powder was transferred to 22 mL Savillex Teflon beakers and dissolved in 2.5 ml concentrated trace-metal grade HNO_3 and 0.5 ml trace-metal grade HF at 110ºC over 48 hours, followed by trace-metal grade aqua regia (3 ml HCl and 1 ml HNO_3) at 110ºC over 48 hours, and then 2 ml of trace-metal grade HCl at 110ºC for 24 hours. Subsequently, each sample solution was stored in a LDPE vial in 5 ml 6M HCl and 3 drops of 0.5% HF.

For analysis of metal concentrations, a small portion of the sample solution was dried, and re-dissolved in 2% HNO_3. An Agilent 8800 triple quadrupole inductively coupled plasma mass spectrometer (QQQ-ICP-MS) was used to measure element concentrations. The United States Geological Survey (USGS) black shale standards Eocene Green River Shale (SGR-1b), Pennsylvanian Brush Creek Shale (SBC-1), and Devonian Ohio Shale (SDO-1) were used as secondary standards to verify instrument accuracy. The multiple analyses of each black shale standard (SBC-1, SGR-1b, and SDO-1) yield relative standard deviation (%RSD) within 5% for major and trace metal elements. The average recovery rate of these standards is within 10% of certified standard values. For each individual sample, the %RSD is within 10%. Duplicates yield %RSD within 5%. Low procedural blank levels (<1%) were observed for all elements analyzed in this study. An internal standard solution with elements Sc, Ge, In and Bi were used to correct for instrumental drift during the course of QQQ-ICP-MS analysis.

Authigenic enrichment factors (EF) were used for correcting variable detrital and carbonate contents in samples. Average upper crust concentrations for Na, Mg, K, Ca, Ti, Fe, Mo, U, V, Zn, Cr, Mn, Co, Pb, and Re are from McLennan (2001), Tribovillard et al. (2006) and Sheen et al. (2018). The formula is as below:

$$EF = [\text{element} / \text{Al}]_{\text{sample}} / [\text{element} / \text{Al}]_{\text{average upper crust}}$$

4.4 Molybdenum isotope measurements

Molybdenum isotope compositions were measured on a Thermo Neptune multi-collector inductively coupled plasma mass spectrometer (MC-ICP-MS) at the W.M. Keck Foundation Laboratory for Environmental Biogeochemistry, School of Earth and Space Exploration, Arizona State University (ASU). The measurements were conducted following the analytical protocol in

Duan et al. (2010), Kendall et al. (2015), and Lu et al. (2017). Prior to separation of Mo from digested sample solutions via ion-exchange chromatography, an appropriate amount of a double spike (^{97}Mo–^{100}Mo) was added to sample solutions for correcting instrumental mass fractionation. BioRad AG1-X8 100-200 mesh resin and BioRad AG50W-X8 200-400 mesh resin were used for Mo anion column chemistry and subsequent Mo cation column chemistry, respectively. NIST-SRM-3134 is an international Mo standard solution against which sample Mo isotope data is reported. The δ^{98}Mo of the NIST-SRM-3134 is defined as +0.25‰ instead of the usual 0‰ (as normally done for isotope standards) to enable the Mo isotope data of samples to be directly compared with the traditional seawater value of ~2.3‰ previously measured against most in-house standards in different laboratories (Nakagawa et al., 2012; Goldberg et al., 2013; Nägler et al., 2014). On this scale, sample δ^{98}Mo is defined by the equation below (Goldberg et al., 2013; Nägler et al., 2014):

$$\delta^{98}\text{Mo}\ (‰) = \{[(^{98/95}\text{Mo})_{\text{sample}} / (^{98/95}\text{Mo})_{\text{NIST-SRM-3134}}] - 1\} \times 1000\} + 0.25$$

In practice, the Mo isotope composition of the samples was first measured relative to ASU’s in-house standard RochMo2. The NIST-SRM-3134 standard was measured during the same analytical sessions as the samples and had an average δ^{98}Mo of 0.32 ± 0.02 ‰ (2SD; n=4) relative to RochMo2. Hence, 0.07‰ was subtracted from each sample δ^{98}Mo measured relative to RochMo2 to yield the sample δ^{98}Mo relative to NIST-SRM-3134 = 0.25‰.

The SDO-1 black shale standard was processed in the same fashion as samples and was used to verify the accuracy of Mo isotope measurements (Barling et al., 2001; Siebert et al., 2003; Arnold et al., 2004; Goldberg et al., 2013; Nägler et al., 2014). During the course of this study, SDO-1 yielded δ^{98}Mo of 0.81 ± 0.02‰ (2SD, n=3) relative to NIST-SRM-3134 = 0.0‰ and 1.06 ± 0.02‰ (2SD, n=3) relative to NIST-SRM-3134 = 0.25‰. The first value shows excellent agreement with the average δ^{98}Mo of 0.82 ± 0.11‰ (2SD, n=145), based on double spike analyses at Arizona State University (Goldberg et al., 2013). The 2SD uncertainty of a sample was reported as the 2SD uncertainty of sample replicate measurements or the long-term reproducibility of SDO-1 (0.11‰), whichever is greater. Three duplicates also yield excellent reproducibility (<3% variation).

4.5 Sulfur isotope measurements

Pyrite sulfur contents and sulfur isotope compositions were measured at the Isotope Science Laboratory, University of Calgary. The procedure followed Mayer and Krouse (2004) and Ardakani et al. (2016). The samples were first mixed with 10 mL of ethanol in a reaction vessel and then reacted with a 1M $CrCl_2$ solution via a rubber septum under a stream of N_2. Subsequently, the solution was boiled for 2 hours to release H_2S and then converted to Ag_2S for S isotope analysis (Mayer and Krouse, 2004). Ag_2S was measured by thermal decomposition in an elemental analyzer coupled to an isotope ratio mass spectrometer (EA-IRMS). Finally, the $^{34}S/^{32}S$ ratios were measured on the by-product SO_2 and expressed relative to the international standard Canyon Diablo Troilite (V-CDT) by $\delta^{34}S$ notation. Calibration and normalization of sulfur isotope measurements are conducted by the repeated analyses of standards IAEA S1 (−0.3‰ by definition), S2 (22.7 ± 0.2‰), and S3 (−32.6 ± 0.2‰). Lab standards analyzed along with samples had a precision of 1.0‰. Pyrite sulfur contents were also used to calculate pyrite iron contents using FeS_2.

5. Results

5.1 TOC content and trace metal enrichments

The TOC contents, major and trace element concentrations as well as some geochemical ratios from six drill cores among different levels of hydrocarbon maturity are shown in Table 1 and Table 2. The enrichment factors and other geochemical ratios are displayed in Table 3. The TOC contents in the two immature cores widely range from 1.0 to 15.3 wt%, with an average of 5.2 ± 5.3 wt% (1SD, n=16). The TOC contents in all three mature cores also have a large range (2.2–19.3 wt%), with an average of 7.6 ± 5.7 wt% (1SD, n=16). By comparison, the overmature core contains relatively low TOC contents (1.3–3.5 wt%), averaging 2.1 ± 0.5 wt% (1SD, n=26).

Trace metal Mo, U and Re concentrations (and enrichment factors) in the two immature cores have similar trends and vary considerably from 1.2 to 116.7 ppm (EFs: 1.2–203.3), 2.4 to 44.5 ppm (EFs: 1.2–41.5), and 3.9 to 214.1 ppb (EFs: 14.8–1398.8), respectively. Similarly, the concentration of these three trace metals in the three mature cores showed significant variations from 18.3 to 129.3 ppm, 6.1 to 66.1 ppm, and 11.2 to 316.0 ppb, respectively. However, Mo, U, and Re in the overmature core have relatively lower concentrations: Mo (1.3–62.7 ppm; EFs: 1.6–62.3), U (2.1–20.7 ppm; EFs: 2.1–9.5), Re (6.8–89.3 ppb; EFs: 43.7–229.6). Vanadium concentrations in the immature cores (91.2–1021.4 ppm; EFs: 1.3–16.8) and mature cores (337.8–1460.4 ppm; EFs: 4.5–22.5) span a wide range but most samples are characterized by high V concentrations. In comparison, the overmature core (76.2–809.9 ppm; EFs: 2.4–13.0) has V concentrations that do not reach levels as high as the immature/mature cores. Overall, the averages and standard deviations for Mo, U, Re, and V for each core are fully summarized in Table 2.

The Mo and TOC contents of the immature shales and mature shales have good correlations ($R^2 = 0.89$, $R^2 = 0.84$, respectively), and both yield slopes of 6.0 ppm/wt%. A significantly weaker correlation between Mo and TOC contents ($R^2 = 0.4$) is observed for the overmature shales. Regarding Mo/TOC ratios, a wide range is observed in immature shales from 1.1 to 15.0 ppm/wt%, with an average of 9.8 ± 8.4 ppm/wt% (2SD, n=16). Mature shales yield Mo/TOC values from 4.8 to 13.6 ppm/wt%, with an average of 9.0 ± 4.8 ppm/wt% (2SD, n=16), and overmature shales have ratios between 0.7 and 24.6 ppm/wt%, averaging 8.8 ± 12.6 ppm/wt% (2SD, n=26). Mo/U EF ratios in immature shales range from 0.9 to 8.2, with an average of 5.9 ± 4.4 (2SD, n=16). Mature core Mo/U EF ratios range from 2.9 to 6.6 (average = 5.4 ± 2.4, 2SD, n=16), whereas the overmature core has Mo/U EF ratios from 0.7 to 10.7, averaging 4.9 ± 4.6 (2SD, n=26; Table 2; Fig. 7). A good correlation is observed between Mo EF and U EF, with the trend falling between 1 times modern seawater Mo/U EF and 3 times modern seawater Mo/U EF ratios.

The Fe/Al ratios in immature shales, mature shales, and overmature shales are 0.3–0.9, averaging 0.5 ± 0.4 (2SD, n=16), 0.4–0.8, averaging 0.5 ± 0.2 (2SD, n=16) and 0.3–0.8, averaging 0.4 ± 0.2 (2SD, n=26), respectively. Most samples have Fe/Al ratios close to 0.5 (average continental crust value; Taylor and McLennan, 1985; Lyons and Severmann, 2006).

Most samples showed a good trend between Re and Mo. The Re/Mo ratios in immature shales, mature shales, and overmature shales range from 0.4 to 3.3, averaging 1.4 ± 1.6 (2SD, n=16), 0.3 to 2.8, averaging 1.2 ± 0.7 (2SD, n=16) and 0.8 to 7.4, averaging 2.1 ± 3.2 (2SD, n=26), respectively (Fig. 8). Fe_{PY}/Fe_T in the immature, mature, and overmature areas are 0.21 to 0.41, averaging 0.33 ± 0.16 (2SD, n=5), 0.22 to 0.59, averaging 0.37 ± 0.26 (2SD, n=9), and 0.21 to 0.33, averaging 0.27 ± 0.10 (2SD, n=4), respectively (Fig. 9).

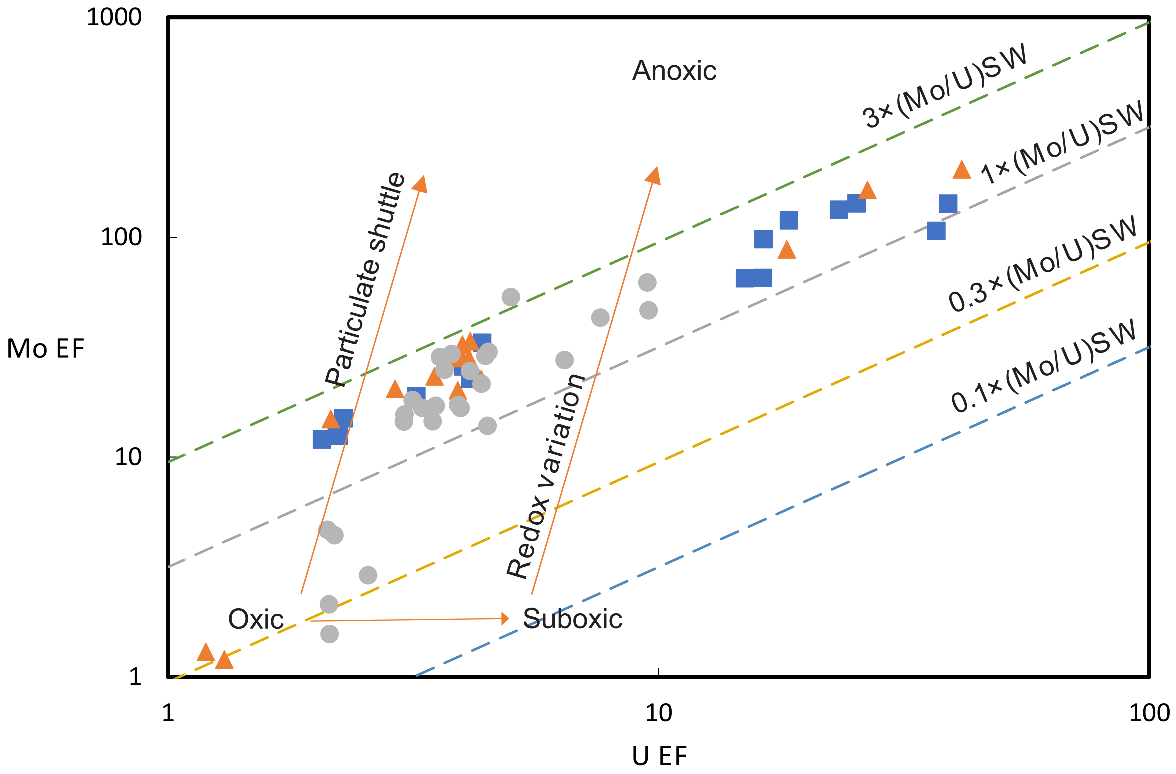

Fig. 7. Geochemical diagram showing cross-plot of Mo EF versus U EF for the Exshaw Formation black shales. Orange triangles refer to data from immature cores; blue squares refer to data from mature cores; grey circles refer to data from the overmature core. Dashed lines represent the weight equivalents of the molar Mo/U EF ratios of modern seawater (1×SW), and corresponding fractions of modern seawater (0.1×SW, 0.3×SW, and 3×SW) (Algeo and Tribovillard, 2009). Enrichment patterns and corresponding controls in the figure are illustrated following Algeo and Tribovillard (2009).

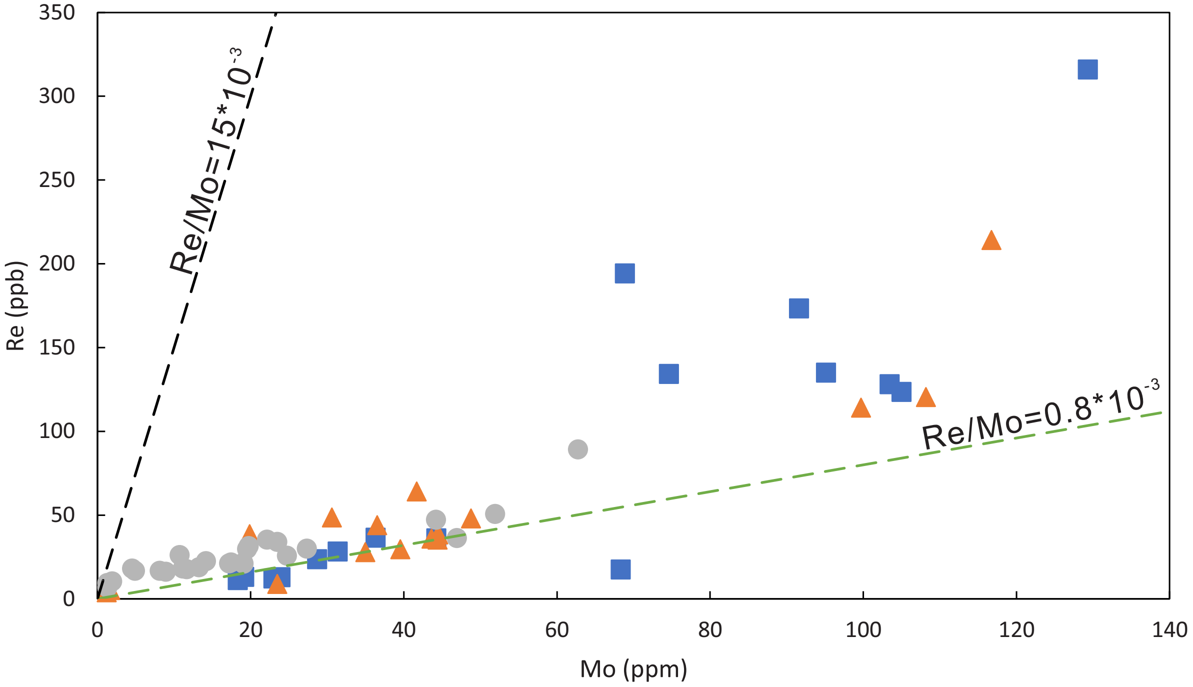

Fig. 8. Geochemical diagram showing cross-plot of Re versus Mo concentrations for the Exshaw Formation black shales. Orange triangles refer to data from immature cores; blue squares refer to data from mature cores; grey circles refer to data from the overmature core.

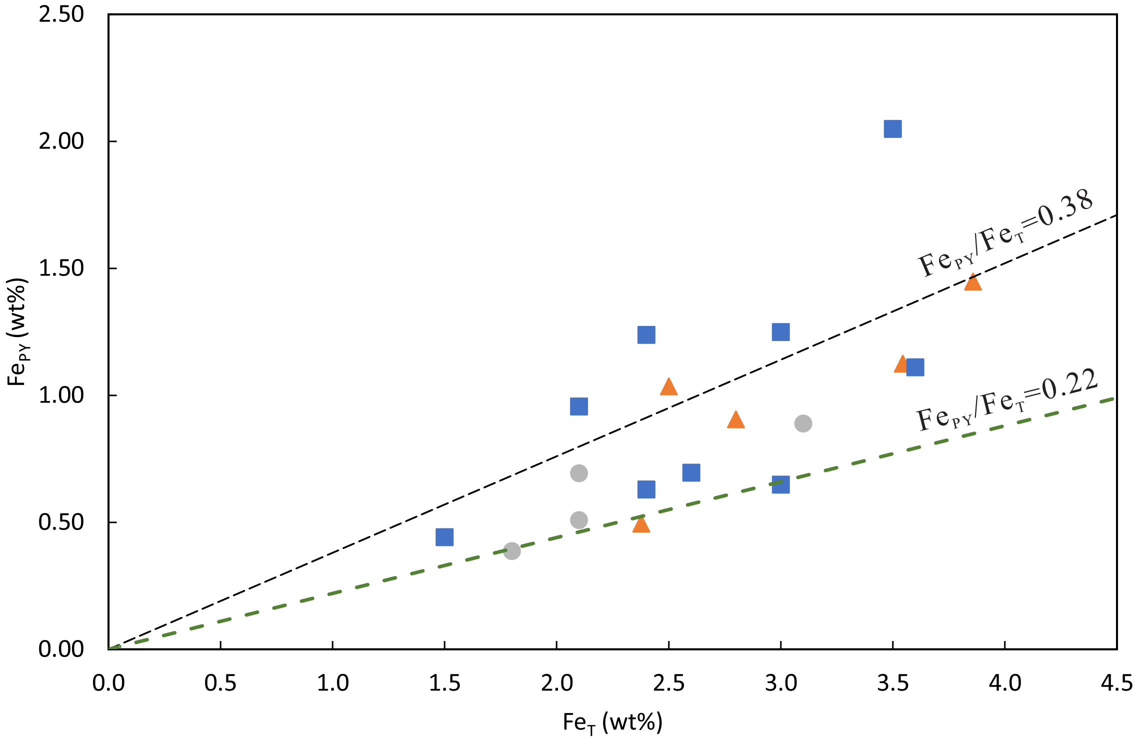

Fig. 9. Geochemical diagram showing cross-plot of Fe_{PY} versus Fe_T abundances for the Exshaw Formation black shales. Orange triangles refer to data from immature cores; blue squares refer to data from mature cores; grey circles refer to data from the overmature core. Grey dashed line refers to the ratios of Fe_{PY}/Fe_T of 0.38. Green dashed line refers to the ratios of Fe_{PY}/Fe_T of 0.22.

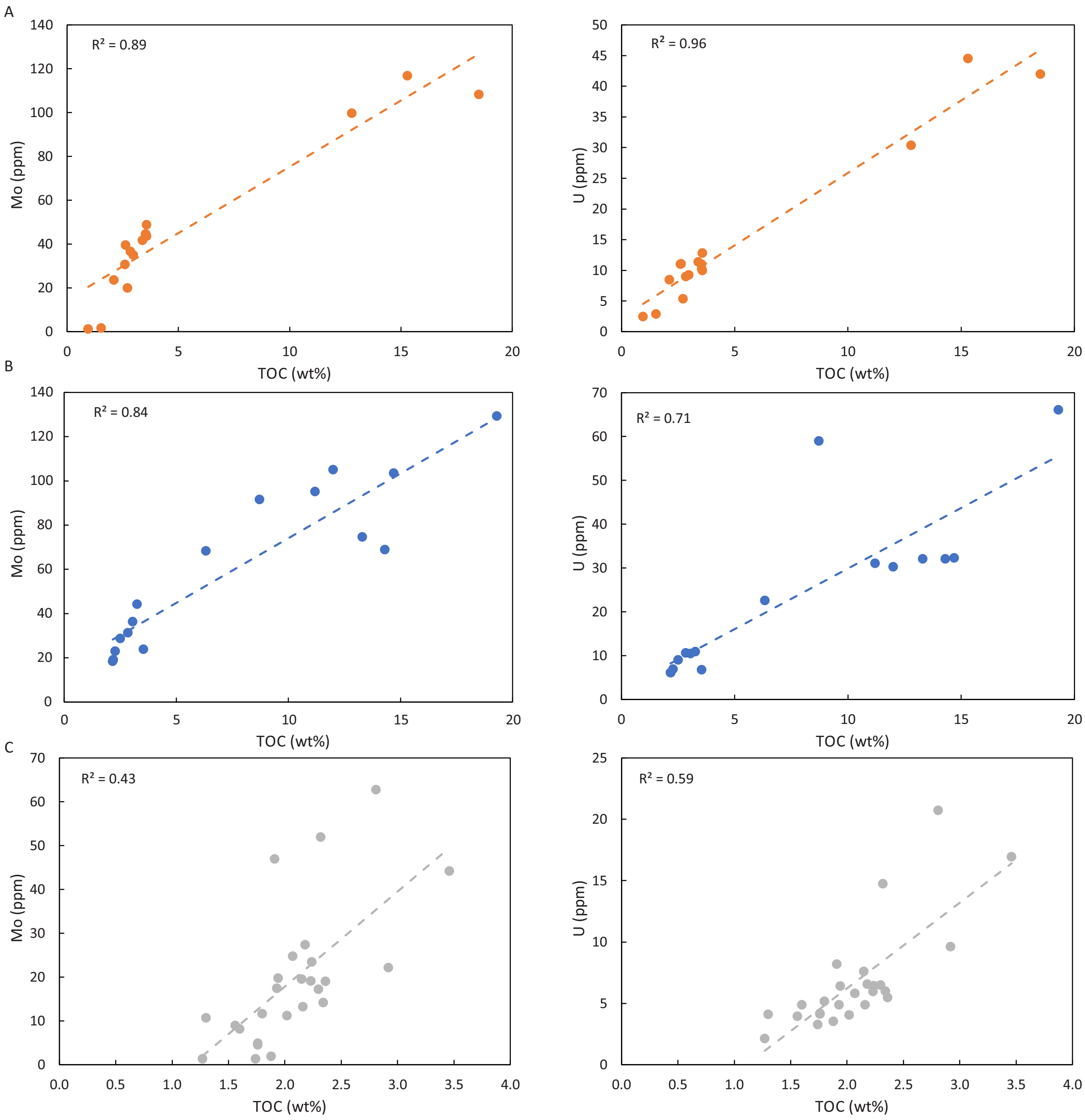

Fig. 10. Geochemical diagrams of Mo concentrations versus TOC content and U concentrations versus TOC content for the Exshaw Formation black shales in immature (A), mature (B) and overmature cores (C). Orange, blue, and grey circles refer to data points in immature cores, mature cores and overmature core, respectively.

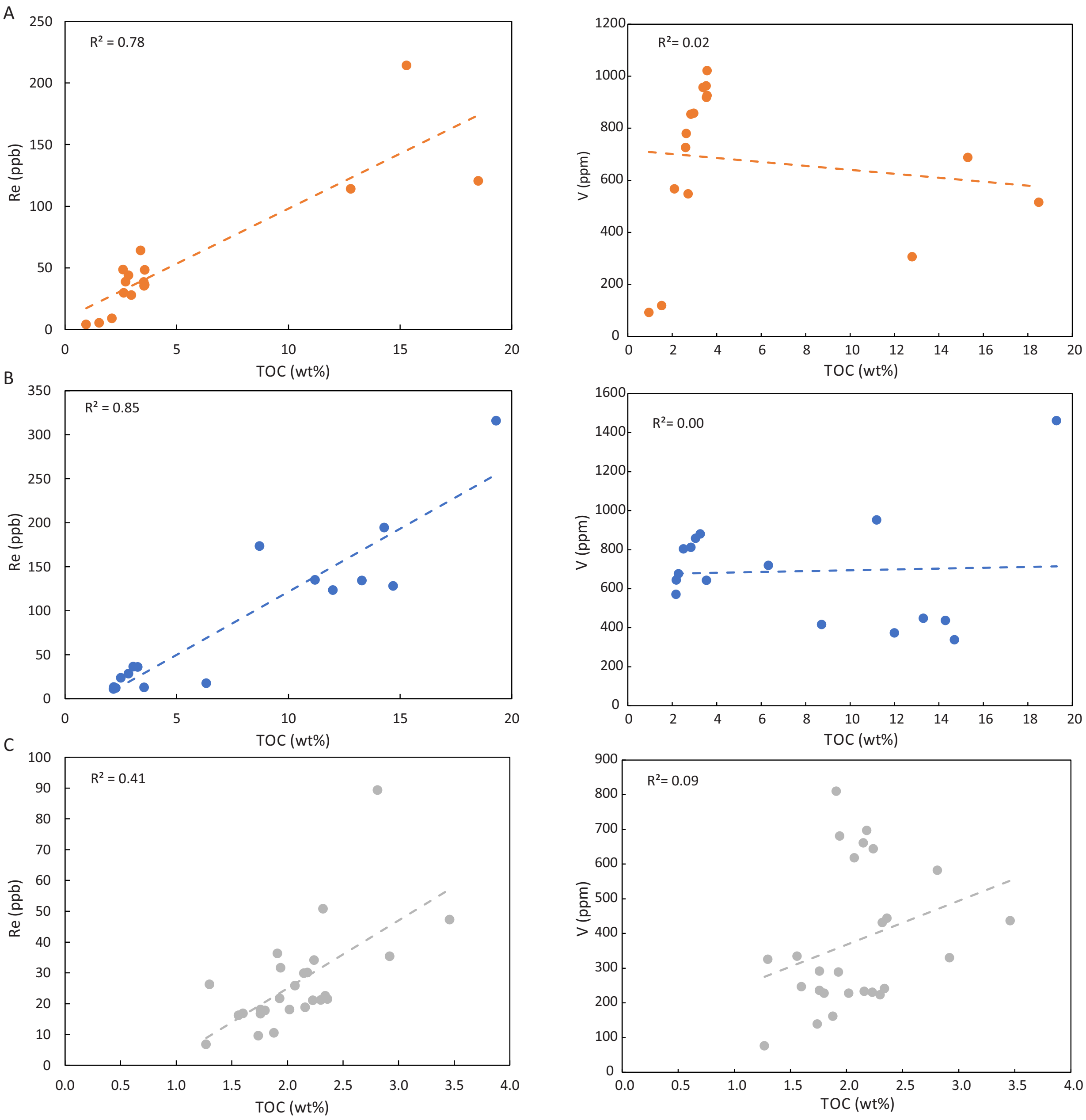

Fig. 11. Geochemical diagrams of Re concentrations versus TOC content and V concentrations versus TOC content for the Exshaw Formation black shales in immature (A), mature (B) and overmature cores (C). Orange, blue, and grey circles refer to data points in immature cores, mature cores and overmature core, respectively.

5.2 Molybdenum isotope compositions

Eighteen samples with high enrichments of Mo from each core were selected to conduct Mo isotope analysis. Overall, δ^{98}Mo in those samples from the three hydrocarbon maturity areas range from 0.26‰ to 1.11‰, with an average of 0.76 ± 0.51‰ (2SD, n=18) (Table 4). Immature black shales yield δ^{98}Mo from 0.65‰ to 0.98‰, averaging 0.85 ± 0.22‰ (2SD, n=5). Mature black shales range from 0.26‰ to 0.99‰, with an average of 0.66 ± 0.52‰ (2SD, n=9). Mo isotope compositions in overmature shales are between 0.41‰ and 1.11‰, with an average of 0.87 ± 0.62‰ (2SD, n=4). Statistically, no significant difference was observed after an unpaired t-test among each area (p-value = 0.15 between immature shales and mature shales, p-value = 0.90 between immature and overmature shales, p-value = 0.23 between mature and overmature shales).

5.3 Pyrite sulfur content and isotope compositions

The same samples analyzed for Mo isotopes were also analyzed for pyrite S content and S isotope compositions (Table 4). Pyrite sulfur content ranges from 0.44 to 2.34 wt% for all samples. The pyrite sulfur content in the immature, mature, and overmature samples are 0.57 to 1.72 wt%, 0.50 to 2.34 wt%, and 0.44 to 1.21 wt%, respectively. Overall, δ^{34}S ranges from –24.7 to 0.9‰ relative to VCDT, with an average of –12.9 ± 14.3‰ (2SD, n=18). Separately, immature shales, mature shales, and overmature shales have a range of –22.1 to 0.9‰ (averaging –9.5 ± 20.3‰; 2SD, n=5), –24.7 to –6.9‰, (averaging –14.5 ± 13.7‰; 2SD, n=9), and –14.3 to –12.9‰, (averaging –13.4 ± 1.2‰; 2SD, n=4), respectively. Similar to Mo isotopes, no significant difference in pyrite sulfur isotope compositions was observed based on unpaired t-tests (p-value = 0.29 between immature and mature shales, p-value = 0.47 between immature and overmature shales, p-value = 0.78 between mature and overmature shales).

Table 1. Elemental data for black shales from the Exshaw Formation

Core depth (m)	TOC[a] (wt%)	Na (wt%)	Mg (wt%)	K (wt%)	Ca (wt%)	Ti (wt%)	Al (wt%)	Fe (wt%)	Mo (ppm)	U (ppm)	V (ppm)	Zn (ppm)	Cr (ppm)	Mn (ppm)	Co (ppm)	Pb (ppm)	Re (ppb)
3-19-80-23w5(I[b])																	
1752.00	3.5	0.4	1.0	4.2	0.3	0.5	8.2	3.5	44.5	11.0	962	9392	112	104	19.5	28.0	38.4
1752.64	3.6	0.4	1.2	4.6	0.3	0.4	9.2	3.9	48.8	12.8	1021	610	115	97.5	21.3	37.4	48.1
1752.90	3.4	0.3	1.0	4.7	0.6	0.4	7.9	3.9	41.7	11.3	957	696	110	114	19.5	37.6	64.1
1753.78	18.5	0.2	0.8	4.9	1.3	0.4	6.6	2.4	108	41.9	515	27.8	89.9	79.0	12.4	28.4	120
1754.40	3.0	0.4	1.1	4.6	0.2	0.4	9.2	4.2	35.0	9.3	857	426	112	108	20.7	75.5	27.8
1754.79	2.6	0.4	1.3	4.6	0.4	0.4	9.1	3.8	39.5	11.1	779	452	106	107	20.0	70.5	29.7
1755.66	1.5	0.3	3.8	3.7	6.3	0.5	6.8	2.0	1.7	2.8	118	28.8	77.6	167	11.7	21.0	5.2
1756.12	1.0	0.3	5.3	2.9	9.3	0.3	5.3	1.6	1.2	2.4	91.2	27.0	61.7	205	8.4	20.8	3.9
13-18-80-23w5(I)																	
1747.51	2.6	0.5	0.9	3.1	0.5	0.4	7.3	3.1	30.6	11.0	725	375	89.3	100	15.8	20.1	48.5
1747.91	2.7	0.5	1.0	3.2	0.8	0.4	7.2	3.5	19.9	5.4	547	182	95.5	142	16.6	19.0	38.6
1748.06	2.1	0.4	0.8	3.0	0.2	0.4	6.2	3.1	23.5	8.5	566	221	80.6	95.2	15.8	23.2	8.8
1748.61	3.6	0.5	0.9	3.2	0.5	0.4	7.2	3.4	43.6	10.0	924	342	105	107	18.0	17.1	35.9
1748.94	3.5	0.5	0.9	3.2	0.6	0.4	7.1	3.5	44.4	10.2	918	356	106	100	18.4	19.4	35.3
1749.58	2.9	0.5	0.8	3.3	0.5	0.4	7.0	3.3	36.5	9.0	853	297	95.2	126	17.1	19.8	43.9
1750.59	15.3	0.2	0.6	2.0	9.5	0.2	3.1	2.8	116	44.5	687	36.5	51.8	143	10.5	16.2	214
1751.14	12.8	0.3	0.7	2.3	7.9	0.2	3.3	2.5	99.7	30.3	306	20.4	50.1	139	11.8	15.0	114
14-22-80-2w6(M[c])																	
2057.80	3.5	0.5	1.0	3.3	0.1	0.4	8.5	3.6	23.9	6.8	642	221	102	91.4	19.6	17.0	12.9
2058.39	2.3	0.5	1.0	3.5	0.1	0.4	9.0	3.5	23.0	6.9	676	331	107	97.7	19.3	19.2	12.1
2058.96	2.2	0.5	1.0	3.4	0.1	0.4	8.5	3.8	19.1	6.1	643	257	105	96.2	19.9	18.8	13.2
2059.60	2.2	0.4	0.9	3.3	0.1	0.4	7.8	2.9	18.3	6.1	570	437	92.4	77.3	16.0	17.6	11.2
2060.08	6.3	0.3	0.3	1.2	0.2	0.1	2.6	1.5	68.3	22.6	719	148	49.1	33.0	7.3	10.4	17.5
2060.37	19.3	0.3	0.8	2.6	1.2	0.3	4.9	3.0	129	66.1	1460	334	97.9	76.1	15.1	27.3	316
6-19-78-25w5(M)																	
2006.33	2.5	0.4	1.2	4.2	0.2	0.4	8.1	3.0	28.7	9.1	802	311	99.1	108	16.5	22.8	23.7
2006.69	3.3	0.3	1.0	4.0	0.3	0.4	7.2	3.5	44.2	10.9	879	472	96.5	97.6	17.1	30.2	36.1
2006.97	3.1	0.3	1.1	3.9	0.3	0.4	7.5	2.9	36.3	10.5	857	673	96.9	91.5	18.7	61.3	36.5
2007.35	11.2	0.2	0.7	2.9	2.3	0.2	3.8	3.0	95.2	31.0	951	104	75.2	89.4	12.7	19.3	135
2007.60	2.9	0.3	1.0	3.5	0.3	0.4	7.4	2.7	31.4	10.6	811	742	97.3	92.0	19.0	15.8	28.3
2008.00	8.7	0.2	0.7	4.2	8.1	0.3	4.6	2.4	91.6	58.9	416	24.2	48.1	131	12.7	20.1	173
2008.37	12.0	0.2	0.8	2.9	5.0	0.3	4.7	2.1	105	30.3	373	36.8	64.8	135	10.6	16.7	123
8-29-78-1w6(M)																	
2099.00	14.3	0.3	0.9	3.6	4.1	0.3	5.7	3.6	68.9	32.1	436	51.5	75.8	108	12.5	25.0	194
2099.12	13.3	0.3	1.2	3.7	4.6	0.4	6.1	2.6	74.6	32.1	447	26.9	77.2	135	11.0	17.6	134

2099.30	14.7	0.3	1.0	3.6	4.1	0.4	5.7	2.4	103	32.3	337	26.7	68.2	109	13.4	18.2	128
4-23-72-10w6(O[d])																	
3559.45	1.7	0.5	2.3	1.9	8.9	0.2	4.4	1.7	1.3	3.3	138	40.5	55.4	229	7.1	6.4	9.6
3559.79	1.3	0.4	4.0	1.0	14.9	0.2	2.4	1.8	1.3	2.1	76.2	24.2	31.9	414	3.4	3.1	6.7
3560.31	1.9	0.5	1.9	2.2	7.4	0.3	4.8	1.9	1.9	3.5	161	62.9	67.2	173	7.0	9.7	10.5
3560.95	1.8	0.5	1.7	2.6	3.8	0.3	5.5	1.5	4.5	4.2	291	78.1	81.5	135	7.4	5.9	18.1
3561.31	2.2	0.5	1.7	2.0	5.5	0.3	4.2	1.8	13.2	4.9	232	74.9	63.1	157	7.0	13.5	18.8
3561.65	1.8	0.6	1.8	2.5	4.2	0.3	5.6	1.9	4.9	4.1	236	42.4	72.4	157	8.1	8.7	16.7
3562.01	2.0	0.4	1.5	2.0	6.9	0.3	3.8	1.9	11.2	4.0	227	29.8	67.2	162	6.7	14.7	18.0
3562.35	1.8	0.5	1.8	2.0	6.1	0.3	4.3	1.5	11.6	5.2	227	167	65.3	173	6.8	8.1	17.7
3562.65	2.3	0.5	1.9	2.1	6.2	0.3	4.4	1.6	14.2	6.0	240	58.3	65.2	188	7.6	9.2	22.5
3562.99	2.2	0.5	1.6	2.0	5.6	0.2	4.1	3.5	19.1	6.0	230	11.4	59.5	166	8.8	23.7	21.1
3563.29	2.3	0.6	2.0	1.9	6.6	0.3	4.3	1.7	17.2	6.5	223	19.5	60.4	185	6.5	9.9	21.1
3563.90	2.2	0.5	1.9	2.5	4.9	0.3	5.0	1.5	23.5	6.4	644	347	91.7	168	7.5	8.6	34.1
3564.36	1.9	0.4	1.4	1.7	7.3	0.3	3.1	1.3	17.4	4.9	289	82.2	64.8	165	5.6	6.5	21.7
3564.76	1.6	0.5	2.0	1.5	10.0	0.3	2.9	2.3	8.9	3.9	333	74.5	62.5	254	4.9	11.7	16.2
3565.34	1.6	0.6	2.2	1.4	10.2	0.2	3.1	1.6	8.1	4.9	246	1417	60.6	248	4.5	8.1	16.8
3565.67	1.9	0.4	1.4	2.6	5.8	0.3	4.7	1.8	46.9	8.2	809	394	104	170	9.6	9.0	36.3
3565.86	2.4	0.4	1.4	2.0	6.6	0.3	3.5	1.4	19.0	5.5	443	244	79.2	173	6.6	6.7	21.5
3566.59	2.9	0.4	1.6	2.4	6.6	0.3	4.3	2.1	22.1	9.6	329	55.0	76.1	219	11.7	12.4	35.3
3567.32	3.5	0.4	1.6	2.6	3.9	0.3	5.1	2.1	44.2	16.9	436	128	75.0	181	13.2	12.5	47.2
3567.65	1.3	0.3	1.6	1.7	3.8	0.2	3.4	1.5	10.7	4.1	325	76.3	50.9	172	5.8	5.3	26.2
3568.23	2.3	0.4	1.4	2.5	4.6	0.3	4.5	2.1	51.9	14.7	431	157	80.1	177	13.9	12.8	50.8
3568.78	2.2	0.5	1.6	3.5	2.4	0.3	7.2	2.5	19.5	7.6	661	173	98.4	144	11.8	21.1	29.9
3569.09	2.1	0.4	1.4	2.2	3.0	0.2	4.7	1.4	24.7	5.8	617	191	80.0	134	7.1	6.8	25.8
3569.39	2.2	0.4	1.2	2.6	3.0	0.3	5.0	1.8	27.3	6.6	696	179	90.1	142	8.3	9.9	30.0
3569.67	1.9	0.4	1.3	3.0	3.0	0.3	5.8	2.4	19.7	6.4	680	195	97.3	144	10.3	20.0	31.6
3570.27	2.8	0.6	1.8	3.9	2.2	0.3	7.8	3.1	62.7	20.7	581	81.2	93.3	153	14.4	22.2	89.3

[a] TOC = Total organic carbon

[b] I = Immature

[c] M = Mature

[d] O = Overmature

Table 2. Comparison of geochemical data from each drill core (ave = average, SD = standard deviation, $_{PY}$ = pyrite)

Drill core[a]	Samples	TOC (wt%) (ave, SD)	Mo (ppm) (ave, SD)	U (ppm) (ave, SD)	V (ppm) (ave, SD)	Re (ppb) (ave, SD)	S_{PY} (wt%) (ave, SD)	Mo/TOC[b] (ave, SD)	δ^{98}Mo (‰) (ave, SD)	δ^{34}S (‰) (ave, SD)
3-19-80-23W5(I)	8	4.6, 5.7	40.1, 33.3	12.8, 12.4	662.8, 378.1	42.2, 37.5	1.1, 0.8	9.2, 5.6	0.88, 0.15	−8.8, 13.8
13-18-80-23W5(I)	8	5.7, 5.2	51.9, 36.1	16.1, 13.8	691.2, 213.3	67.4, 66.4	1.2, 0.1	10.4, 2.4	0.83, 0.11	−9.9, 10.5
14-22-80-2W6(M)	3	6.0, 6.7	47, 44.6	19.1, 23.9	785.5, 334.2	63.8, 123.6	0.6, 0.2	8.6, 1.7	0.36, 0.11	−24.3, 0.6
6-19-78-25W5(M)	6	6.2, 4.2	61.8, 33.8	23.0, 18.5	727.5, 232.9	79.5, 62.3	1.6, 0.5	10.8, 1.8	0.76, 0.34	−11.3, 6.0
8-29-78-1W6(M)	7	14.1, 0.7	82.3, 18.5	32.2, 0.1	407.1, 60.2	152.3, 36.6	0.9, 0.3	5.8, 1.1	0.74, 0.09	−12.1, 3.0
4-23-72-10W6(O)	26	2.1, 0.5	19.5, 15.9	6.8, 4.3	377.4, 202.6	26.7, 16.6	0.7, 0.3	8.8, 6.3	0.87, 0.31	−13.4, 0.6

[a] = I refers to immature; M refers to mature; O refers to overmature

[b] = (ppm/wt%)

Table 3. Enrichment factors and geochemical ratios for the Exshaw Formation black shales

Core depth (m)	Na	Mg	K	Ca	Ti	Fe	Mo	U	V	Zn	Cr	Mn	Co	Pb	Re	Mo/TOC[a]	Mo/U EF[b]	Fe/Al	Re/Mo
3-19-80-23w5(I)																			
1752.00	0.1	0.7	1.5	0.1	1.1	1.0	29.1	3.9	8.8	129	1.3	0.2	1.1	1.6	94.3	12.6	7.6	0.4	0.9
1752.64	0.1	0.8	1.4	0.1	0.9	1.0	28.3	4.0	8.3	7.5	1.2	0.1	1.1	1.9	104	13.6	7.1	0.4	1.0
1752.90	0.1	0.8	1.7	0.2	1.1	1.1	28.2	4.1	9.1	9.9	1.3	0.2	1.2	2.2	162	12.3	6.9	0.5	1.5
1753.78	0.1	0.8	2.1	0.5	1.1	0.8	87.9	18.3	5.9	0.5	1.3	0.2	0.9	2.0	367	5.8	4.8	0.4	1.1
1754.40	0.1	0.7	1.4	0.1	0.9	1.1	20.5	2.9	7.0	5.3	1.2	0.2	1.1	3.9	61.1	11.8	7.1	0.5	0.8
1754.79	0.1	0.9	1.5	0.1	0.9	1.0	23.3	3.5	6.4	5.6	1.1	0.2	1.0	3.7	65.5	15.0	6.7	0.4	0.8
1755.66	0.1	3.3	1.6	2.5	1.3	0.7	1.3	1.2	1.3	0.5	1.1	0.3	0.8	1.5	15.4	1.1	1.1	0.3	3.2
1756.12	0.1	6.0	1.6	4.7	1.3	0.7	1.2	1.3	1.3	0.6	1.1	0.5	0.7	1.8	14.8	1.3	0.9	0.3	3.3
13-18-80-23w5(I)																			
1747.51	0.2	0.7	1.2	0.2	1.0	1.0	22.6	4.4	7.5	5.9	1.2	0.2	1.0	1.3	134	11.7	5.2	0.4	1.6
1747.91	0.2	0.8	1.3	0.3	1.1	1.1	14.9	2.1	5.7	2.9	1.3	0.3	1.1	1.3	108	7.3	6.9	0.5	1.9
1748.06	0.2	0.7	1.4	0.1	1.2	1.1	20.1	3.9	6.8	4.0	1.2	0.2	1.2	1.8	28.4	11.1	5.2	0.5	0.4
1748.61	0.2	0.7	1.3	0.2	1.1	1.1	32.5	4.0	9.7	5.4	1.4	0.2	1.2	1.1	100	12.2	8.2	0.5	0.8
1748.94	0.2	0.8	1.3	0.2	1.2	1.2	33.6	4.1	9.8	5.7	1.5	0.2	1.2	1.3	100	12.5	8.1	0.5	0.8
1749.58	0.2	0.7	1.4	0.2	1.1	1.1	28.1	3.7	9.2	4.8	1.3	0.2	1.2	1.3	126	12.8	7.6	0.5	1.2
1750.59	0.2	1.2	1.9	8.3	1.3	2.1	203	41.5	16.8	1.3	1.6	0.6	1.6	2.5	1398	7.6	4.9	0.9	1.8
1751.14	0.2	1.2	2.0	6.5	1.4	1.8	163	26.7	7.0	0.7	1.5	0.6	1.7	2.2	702	7.8	6.1	0.8	1.1
14-22-80-2w6(M)																			
2057.80	0.2	0.7	1.1	0.0	1.0	1.0	15.0	2.3	5.7	2.9	1.2	0.1	1.1	0.9	30.5	6.7	6.6	0.4	0.5
2058.39	0.1	0.7	1.1	0.0	1.0	0.9	13.7	2.2	5.7	4.2	1.2	0.1	1.0	1.0	27.1	10.1	6.2	0.4	0.5
2058.96	0.2	0.7	1.2	0.0	0.9	1.0	12.0	2.1	5.7	3.4	1.2	0.2	1.1	1.0	31.0	8.7	5.8	0.4	0.7
2059.60	0.2	0.7	1.2	0.0	1.0	0.9	12.5	2.2	5.5	6.3	1.1	0.1	1.0	1.1	28.6	8.4	5.6	0.4	0.6
2060.08	0.3	0.7	1.3	0.2	1.1	1.3	142	25.3	21.1	6.6	1.9	0.2	1.4	1.9	137	10.8	5.6	0.6	0.3
2060.37	0.2	1.0	1.5	0.7	1.1	1.4	142	38.9	22.5	7.8	1.9	0.2	1.5	2.7	1303	6.7	3.7	0.6	2.4
6-19-78-25w5(M)																			
2006.33	0.1	0.9	1.5	0.1	1.0	0.9	19.0	3.2	7.4	4.4	1.2	0.2	1.0	1.3	58.9	11.4	5.9	0.4	0.8
2006.69	0.1	0.8	1.6	0.1	1.1	1.1	33.1	4.4	9.2	7.5	1.3	0.2	1.1	2.0	101	13.6	7.6	0.5	0.8
2006.97	0.1	0.8	1.5	0.1	1.0	0.9	25.9	4.0	8.6	10.1	1.2	0.2	1.2	3.9	97.6	11.9	6.5	0.4	1.0
2007.35	0.2	1.1	2.2	1.6	1.1	1.8	133	23.3	18.7	3.1	1.9	0.3	1.6	2.4	709	8.5	5.7	0.8	1.4
2007.60	0.1	0.9	1.4	0.1	1.0	0.8	22.8	4.1	8.3	11.4	1.3	0.2	1.2	1.0	77.0	11.0	5.5	0.4	0.9
2008.00	0.1	0.9	2.6	4.7	1.4	1.2	106	36.8	6.8	0.6	1.0	0.4	1.3	2.1	757	10.5	2.9	0.5	1.9
2008.37	0.1	1.0	1.8	2.9	1.2	1.0	119	18.4	5.9	0.9	1.3	0.4	1.1	1.7	527	8.7	6.5	0.5	1.2
8-29-78-1w6(M)																			
2099.00	0.2	0.9	1.8	1.9	1.1	1.4	65.3	16.3	5.8	1.0	1.3	0.3	1.0	2.1	691	4.8	4.0	0.6	2.8
2099.12	0.1	1.1	1.7	2.0	1.2	1.0	65.1	15.0	5.5	0.5	1.2	0.3	0.8	1.4	439	5.6	4.3	0.4	1.8
2099.30	0.1	1.0	1.8	2.0	1.2	1.0	97.9	16.4	4.5	0.5	1.2	0.3	1.1	1.5	455	7.0	6.0	0.4	1.2

4-23-72-10w6(O)

3559.45	0.3	3.2	1.2	5.4	1.1	0.9	1.6	2.1	2.4	1.0	1.2	0.7	0.8	0.7	43.7	0.7	0.7	0.4	7.4
3559.79	0.4	10.1	1.2	16.7	1.2	1.8	2.9	2.6	2.4	1.1	1.3	2.3	0.7	0.6	56.8	1.0	1.1	0.8	5.2
3560.31	0.3	2.4	1.3	4.2	1.2	0.9	2.1	2.1	2.5	1.5	1.4	0.5	0.7	1.0	44.1	1.0	1.0	0.4	5.5
3560.95	0.3	1.9	1.3	1.9	1.1	0.6	4.4	2.2	4.0	1.6	1.4	0.3	0.6	0.5	66.1	2.6	2.0	0.3	4.0
3561.31	0.3	2.5	1.3	3.5	1.2	1.0	16.7	3.3	4.1	2.0	1.4	0.5	0.8	1.5	89.2	6.1	5.1	0.4	1.4
3561.65	0.3	1.9	1.3	2.0	1.2	0.8	4.7	2.1	3.2	0.9	1.2	0.4	0.7	0.7	59.9	2.8	2.2	0.3	3.4
3562.01	0.3	2.4	1.5	4.8	1.5	1.2	15.6	3.0	4.5	0.9	1.7	0.6	0.8	1.8	94.6	5.5	5.1	0.5	1.6
3562.35	0.3	2.6	1.3	3.8	1.3	0.8	14.5	3.5	4.0	4.4	1.5	0.5	0.7	0.9	83.2	6.5	4.2	0.4	1.5
3562.65	0.3	2.6	1.4	3.8	1.3	0.8	17.3	3.9	4.1	1.5	1.4	0.6	0.8	1.0	102	6.1	4.4	0.4	1.6
3562.99	0.3	2.4	1.4	3.6	1.1	1.9	24.7	4.1	4.2	0.3	1.4	0.5	1.0	2.7	102	8.6	6.0	0.8	1.1
3563.29	0.4	2.8	1.3	4.1	1.2	0.9	21.6	4.4	3.9	0.5	1.4	0.6	0.7	1.1	99.5	7.5	5.0	0.4	1.2
3563.90	0.3	2.3	1.4	2.6	1.2	0.7	25.0	3.7	9.6	7.8	1.8	0.4	0.7	0.8	136	10.5	6.8	0.3	1.5
3564.36	0.4	2.7	1.6	6.3	1.8	0.9	30.1	4.5	7.0	3.0	2.0	0.7	0.9	1.0	140	9.0	6.7	0.4	1.2
3564.76	0.5	4.3	1.5	9.4	1.8	1.8	16.7	4.0	8.8	3.0	2.1	1.2	0.8	1.9	114	5.7	4.2	0.8	1.8
3565.34	0.6	4.2	1.3	8.7	1.5	1.1	13.9	4.5	5.9	51.3	1.9	1.1	0.7	1.2	108	5.1	3.1	0.5	2.1
3565.67	0.2	1.9	1.6	3.3	1.4	0.9	53.5	5.0	13.0	9.5	2.2	0.5	1.0	0.9	155	24.6	10.7	0.4	0.8
3565.86	0.3	2.3	1.7	5.0	1.5	0.9	28.8	4.4	9.4	7.8	2.2	0.7	0.9	0.9	122	8.1	6.5	0.4	1.1
3566.59	0.3	2.3	1.6	4.2	1.3	1.1	27.7	6.4	5.8	1.5	1.7	0.7	1.3	1.4	165	7.6	4.3	0.5	1.6
3567.32	0.2	1.9	1.5	2.1	1.1	1.0	46.5	9.5	6.4	2.8	1.4	0.5	1.2	1.2	186	12.8	4.9	0.4	1.1
3567.65	0.3	3.0	1.5	3.0	1.0	1.0	17.1	3.5	7.3	2.6	1.5	0.7	0.8	0.8	157	8.2	4.9	0.5	2.5
3568.23	0.2	1.9	1.6	2.7	1.3	1.1	62.3	9.5	7.3	4.0	1.7	0.5	1.5	1.4	228	22.4	6.6	0.5	1.0
3568.78	0.2	1.3	1.4	0.9	0.9	0.8	14.5	3.0	6.9	2.7	1.3	0.3	0.8	1.4	83.3	9.1	4.8	0.3	1.5
3569.09	0.2	1.8	1.4	1.7	1.0	0.7	28.5	3.6	10.0	4.7	1.7	0.4	0.7	0.7	111	12.0	8.0	0.3	1.0
3569.39	0.2	1.5	1.5	1.6	1.0	0.8	29.4	3.8	10.5	4.1	1.8	0.4	0.8	0.9	121	12.5	7.8	0.4	1.1
3569.67	0.2	1.4	1.5	1.4	1.0	0.9	18.2	3.2	8.8	3.8	1.6	0.3	0.8	1.6	109	10.2	5.8	0.4	1.6
3570.27	0.2	1.4	1.4	0.8	0.9	0.9	43.0	7.6	5.6	1.2	1.2	0.3	0.9	1.3	229	22.3	5.7	0.4	1.4

---

[a] TOC = Total organic carbon

[b] EF = Enrichment factor

Table 4. Mo isotope, pyrite S isotope, S content, and Fe_{py}/Fe_T data for the Exshaw Formation black shales

Core depth (m)	$\delta^{98}Mo$[a] (‰)	2SD Measured	2SD[b] Reported	n	$\delta^{34}S_{py}$[c] (‰ VCDT)	S_{PY} (wt%)	Fe_{py}/Fe_T
3-19-80-23w5(I)							
1752.64	0.77	0.05	0.11	3	−18.5	1.7	0.38
1753.78	0.98	0.02	0.11	3	0.9	0.6	0.21
13-18-80-23w5(I)							
1748.94	0.75	0.03	0.11	3	−22.1	1.3	0.32
1750.59	0.78	0.02	0.11	3	−4.1	1.0	0.32
1750.59(rpt)	0.80	0.04	0.11	3	−4.7	1.7	0.54
1751.14	0.95	0.01	0.11	3	−3.6	1.2	0.41
14-22-80-2w6(M)							
2060.08	0.44	0.01	0.11	3	−24.7	0.5	0.29
2060.37	0.28	0.02	0.11	3	−23.9	0.7	0.22
6-19-78-25w5(M)							
2006.69	0.84	0.04	0.11	3	−13.5	2.3	0.59
2007.35	0.26	0.02	0.11	3	−13.5	1.4	0.42
2008.00	0.93	0.02	0.11	3	−15.9	1.4	0.52
2008.37	0.99	0.02	0.11	3	−2.5	1.1	0.46
8-29-78-1w6(M)							
2099.00	0.65	0.04	0.11	3	−10.4	1.3	0.31
2099.12	0.75	0.04	0.11	3	−10.3	0.8	0.27
2099.12(rpt)	0.76	0.02	0.11	3	−6.9	1.3	0.44
2099.30	0.83	0.02	0.11	3	−15.6	0.7	0.26
4-23-72-10w6(O)							
3565.67	0.41	0.00	0.11	3	−13.4	0.4	0.21
3567.32	1.00	0.01	0.11	3	−13.2	0.6	0.24
3568.23	1.11	0.04	0.11	3	−12.9	0.8	0.33
3570.27	0.94	0.03	0.11	3	−14.3	1.0	0.29
3570.27(rpt)	0.94	0.03	0.11	3	−14.3	1.2	0.34

[a] Mo isotope data reported relative to NIST SRM 3134 = +0.25‰.

[b] Reported uncertainty is the 2SD of replicate measurements or 0.11‰, whichever is greater.

[c] S isotope data reported relative to VCDT.

6. Discussion

6.1 Thermal maturation effects

Organic-rich mudrocks are characterized by various levels of authigenic enrichments of redox-sensitive metals based on their depositional conditions. However, post-depositional processes including burial diagenesis and thermal maturation could cause remobilization of some elements in sediments and alter their original signatures, leading to misinterpretation of depositional redox conditions (Lev et al., 2000; Algeo and Maynard, 2004; Abanda and Hannigan, 2006). The organic matter (OM) chemical composition is changed during thermal maturation through loss of functional groups, generation of hydrocarbons, and subsequent restructuring of the molecular composition (Raiswell and Berner, 1987; Seewald, 2003; Ardakani et al., 2016). Among these processes, thermochemical sulfate reduction (TSR) is the redox reaction involving sulfate (SO_4^{2-}) reduction and organic matter oxidation at relatively high temperatures (i.e., $80 < T < 200$ºC; Orr, 1997; Machel et al., 1995; Cross et al., 2004), with the by-products of bitumen/pyrobitumen, hydrogen sulfide, and carbonates (Machel et al., 1995; Machel, 2001; King et al., 2014). TSR also potentially causes the recrystallization of pyrite and subsequent replacement of other diagenetic minerals. Another common reaction for sulfate is microbial sulfate reduction (MSR), driven by microbial activity at relatively lower temperatures ($0 < T < 60$–80ºC; Machel et al., 1995). Both petrographic and geochemical analyses could be used to differentiate TSR and MSR. Framboidal pyrite is usually present in black shales because of MSR whereas cubic or prismatic pyrite are generally found in black shales which have undergone TSR (Machel et al., 1995).

The other effective method to distinguish TSR and MSR is to identify S isotope fractionation. Previous experiments have identified that the sulfur isotope fractionation factors during TSR between sulfate and H_2S ($\Delta^{34}S_{H2S\text{–}sulfate}$) is temperature dependent. The fractionation is –15 to –10‰ at 150–200ºC (overmature conditions) and –20 to –15‰ at 100–150ºC (mature conditions), respectively (Krouse et al., 1988; Machel et al., 1995). By comparison, there is usually a large sulfur isotope fractionation for MSR ($\Delta^{34}S_{H2S\text{–}sulfate}$ = –15 to –65‰; Harrison and Thode, 1958; Cross et al., 2004; Canfield, 2001; Amrani, 2014). From a previous study, the seawater $\delta^{34}S$ values from the Late Devonian to Early Carboniferous likely ranged from ~20 to 30‰ (Kampschulte and Strauss, 2004). In the Exshaw Formation, the immature shales yield $\delta^{34}S$ from –22.1 to 0.9‰ (averaging –9.5 ± 20.3‰; 2SD, n=5). Thus, the S isotope fractionation between the original sulfate and pyrite is –19.1 to –52.1‰ ($\Delta\delta^{34}S_{pyrite\text{-}sulfate}$ = 0.9‰ – 20‰ = –19.1‰, –22.1‰ – 30‰ = –52.1‰), with an average of –35.6‰. Following the same method, the mature and overmature shales have $\delta^{34}S$ from –24.7 to –2.5‰ (averaging –14.5 ± 13.6‰; 2SD, n=9), and –14.3 to –12.9‰ (averaging –13.4 ± 1.2‰; 2SD, n=4), respectively. Thus, S isotope fractionation in mature and overmature shales are calculated to range from –22.5 to –54.7‰ (averaging –38.6‰), and –32.9 to –44.3‰ (averaging –38.6‰), respectively. This large S isotope fractionation in all three areas is consistent with S isotope patterns typical for MSR rather than TSR, suggesting pyrite in black shales were formed microbially but not thermally. As modern analogues, the Black Sea upper Holocene microlaminated deposits yield a mean $\delta^{34}S$ of –37.2 ± 1.8‰ (2SD, n = 18) (Lyons, 1997) and the Cariaco Basin yield an average $\delta^{34}S$ of –32.7 ± 1.8‰ (2SD, n = 17) (Lyons et al., 2003) from Site 1002 of Leg 165 of the Ocean Drilling Program. Compared to modern analogues, the Exshaw Formation black shales have similar pyrite sulfur isotope compositions, consistent with the interpretation of limited effects of hydrothermal maturation. Statistically, an unpaired t-test of Mo and S isotopes yield no statistically significant differences (see results section) between the different maturity levels. This insignificant difference between immature, mature, and overmature shales suggests that the effects of hydrothermal maturation on Mo and S isotopes are minimal. To further understand the effects of thermal maturation on trace metal distribution, geochemical diagrams were created between $\delta^{34}S$ and TOC (Fig. 12). The observation of no significant correlations in these figures is consistent with the minimal influence of TSR, given that this process has been shown previously to cause negative correlations between pyrite $\delta^{34}S$ and TOC content due to the OM depletion caused by TSR (Ardakani et al., 2016).

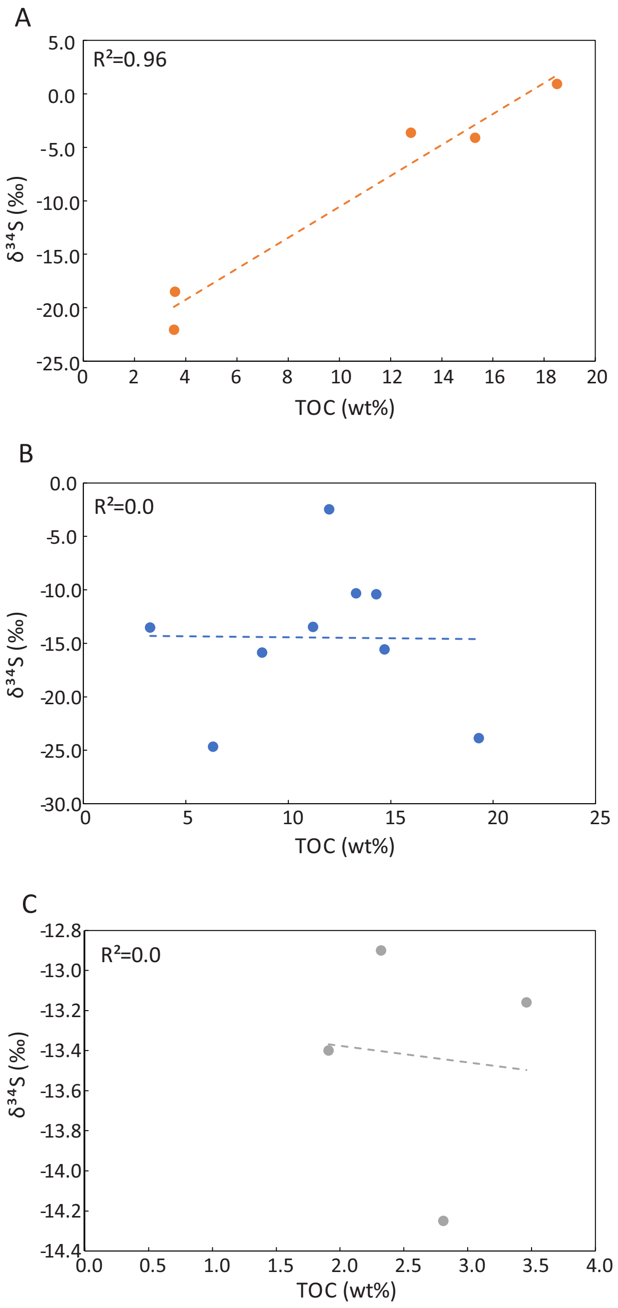

Fig. 12. Geochemical diagrams showing the correlation of δ^{34}S versus TOC for the Exshaw Formation black shales in immature (A), mature (B) and overmature (C). Orange, blue, and grey circles refer to data points in immature cores, mature cores, and overmature core, respectively.

There are also some previous studies that support this interpretation (Raiswell and Berner, 1987; Cruse and Lyons, 2004; Ross and Bustin, 2009). Ross and Bustin (2009) stated that the alteration of the whole rock geochemical signatures in Devonian-Mississippian black shales, from Besa River, Golata, Muskwa and Fort Simpson, is minimal, based on the observation of significant and interpretable relationships between trace metals (eg., Mo, U, Re, V) and TOC content. In addition, although thermal maturation could cause a 40–60% reduction of organic carbon in fine-grained sedimentary rocks (Raiswell and Berner, 1987), the loss of metals is not necessarily associated with this process due to the bond with high weight molecular organics as well as low permeability of shales caused by their fine grain size (Abanda and Hannigan, 2006). Moreover, metals (Mo in particular) might be recaptured in other phases (eg., sulfides) within shales (Helz et al., 1996; Helz and Vorlicek, 2019). Creaser et al. (2002), Selby and Creaser (2003), and Selby and Creaser (2005) have demonstrated that the Re-Os radioactive isotope system is not affected by hydrocarbon maturity, based on the observation of consistent Re-Os depositional ages from the Exshaw Formation black shales that agree with independent U-Pb zircon age constraints for the Devonian-Mississippian boundary. Since Re and Mo have many geochemical similarities, the accurate Re-Os age suggests Mo is not disturbed by post-depositional processes.

In this study, trace metal concentrations (Mo, U, Re, V) in immature shales and mature shales vary widely. Although the overmature shales are characterized by relatively lower trace metal enrichments compared to immature and mature shales, a large number of overmature shales have relatively enriched trace metal concentrations. The TOC contents in both immature and mature areas vary considerably (1.0 to 15.3 wt% and 2.2 to 19.3 wt%, respectively), whereas the overmature core has a relatively small range of TOC contents (1.3 to 3.5 wt%). The overmature shales showed relatively poor correlations between trace metal and TOC contents, compared to immature and mature shales (Fig. 10; Fig. 11). Examples of similar trace metal concentrations but lower TOC content for overmature shales versus immature and mature shales suggests that TOC was lost at overmature conditions, but the trace metals remained largely immobile, which is consistent with the findings by Raiswell and Berner (1987). Creaser et al. (2002) used T_{max} to evaluate sample hydrocarbon maturity level, which represents the temperature of peak hydrocarbon release by kerogen cracking in the Rock-Eval pyrolyzer. The defined T_{max} ranges for immature, mature and overmature shales are below 435ºC, between 435ºC and 465ºC, and above 465ºC, respectively (Peters, 1986). The Exshaw mature shales have T_{max} near 435ºC, which suggest they are early mature shales (Creaser et al., 2002). Thus, the differences in T_{max} suggests that the loss of TOC from the immature and early mature shales was appreciably less than the TOC loss from the overmature shales.

Therefore, based on the observation of petrography, sulfur isotope fractionation, t-test results, and trace metal/TOC ratios, it is suggested that there were no significant overprinting effects of thermal maturity on the inorganic geochemistry of the Exshaw Formation black shales. As such, inorganic redox-sensitive geochemical signatures can be used to make inferences about the local depositional environment.

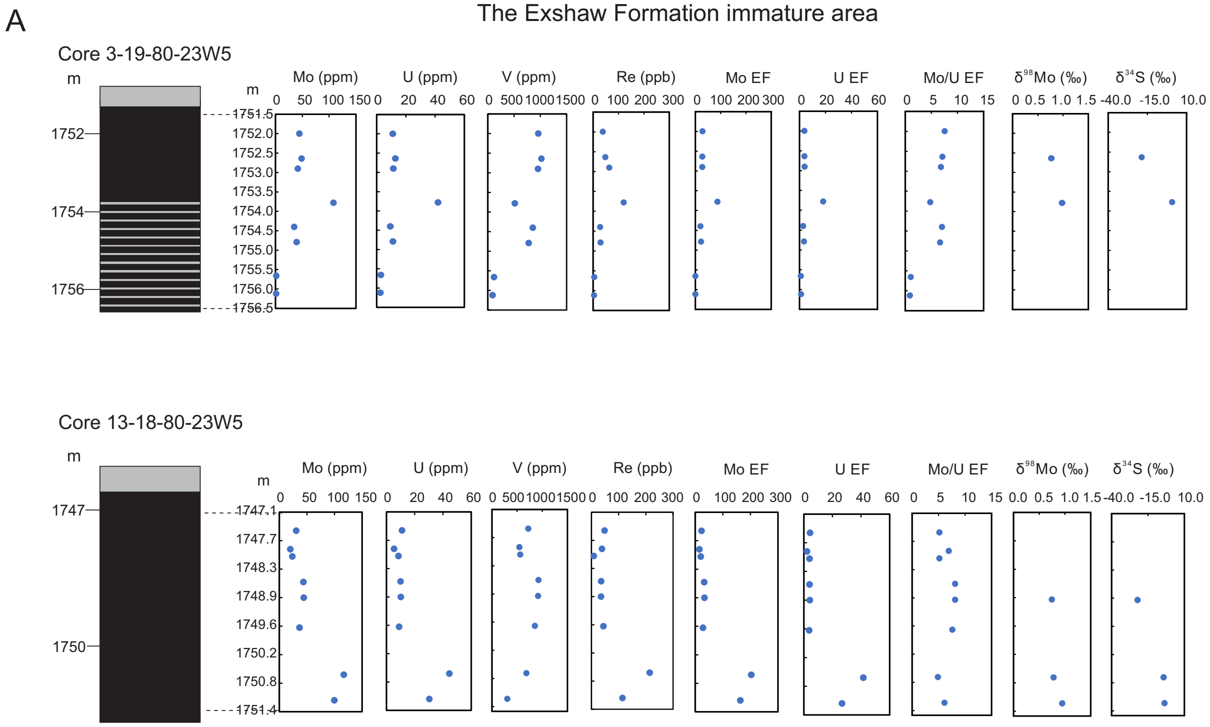

A
The Exshaw Formation immature area
Core 3-19-80-23W5
m
1752
1754
1756
1751.5
1752.0
1752.5
1753.0
1753.5
1754.0
1754.5
1755.0
1755.5
1756.0
1756.5
Mo (ppm)
0 50 100 150
U (ppm)
0 20 40 60
V (ppm)
0 500 1000 1500
Re (ppb)
0 100 200 300
Mo EF
0 100 200 300
U EF
0 20 40 60
Mo/U EF
0 5 10 15
δ98Mo (‰)
0 0.5 1.0 1.5
δ34S (‰)
-40.0 -15.0 10.0
Core 13-18-80-23W5
m
1747
1750
1747.1
1747.7
1748.3
1748.9
1749.6
1750.2
1750.8
1751.4
Mo (ppm)
0 50 100 150
U (ppm)
0 20 40 60
V (ppm)
0 500 1000 1500
Re (ppb)
0 100 200 300
Mo EF
0 100 200 300
U EF
0 20 40 60
Mo/U EF
0 5 10 15
δ98Mo (‰)
0.0 0.5 1.0 1.5
δ34S (‰)
-40.0 -15.0 10.0

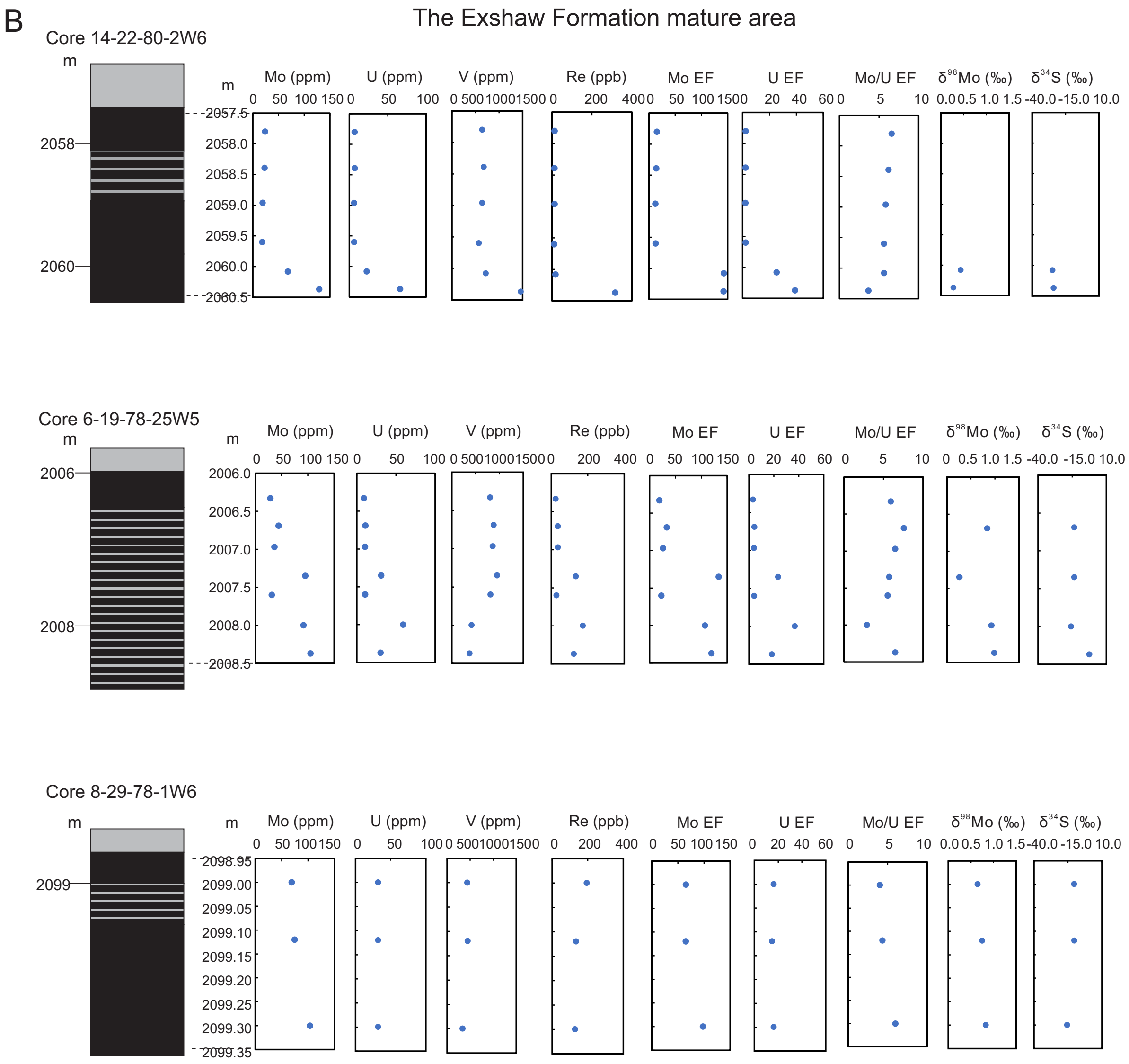
B
The Exshaw Formation mature area
Core 14-22-80-2W6
m
2058
2060
2057.5
2058.0
2058.5
2059.0
2059.5
2060.0
2060.5
Core 6-19-78-25W5
2006
2008
2006.0
2006.5
2007.0
2007.5
2008.0
2008.5
Core 8-29-78-1W6
2099
2098.95
2099.00
2099.05
2099.10
2099.15
2099.20
2099.25
2099.30
2099.35
Mo (ppm)
0 50 100 150
U (ppm)
0 50 100
V (ppm)
0 500 1000 1500
Re (ppb)
0 200 400
Mo EF
0 50 100 150
U EF
0 20 40 60
Mo/U EF
0 5 10
δ98Mo (‰)
0.0 0.5 1.0 1.5
δ34S (‰)
-40.0 -15.0 10.0

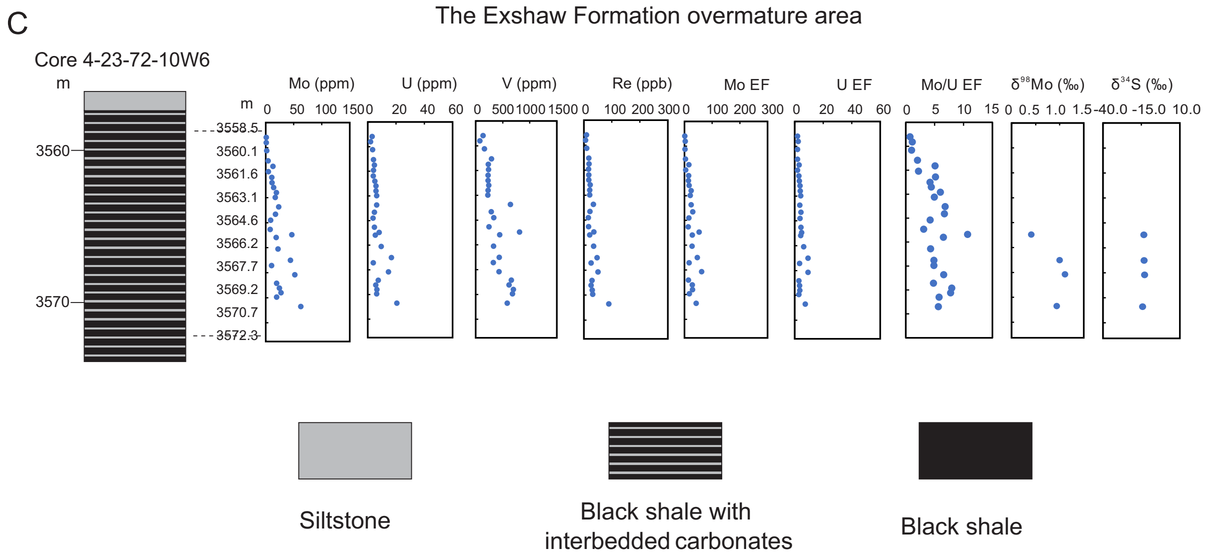

Fig. 13. Geochemical profiles for the Exshaw Formation in drill cores from the immature area (A), mature area (B) and overmature area (C).

6.2 Elemental constraints on local marine redox conditions

6.2.1 Immature area

Trace metals such as Mo, U, Re, and V in sediments are used as proxies to reflect local water column paleoredox conditions and constrain local basin restriction (Tribovillard et al., 2006; Algeo and Tribovillard, 2009; Scott et al., 2017; Sheen et al., 2018). In the two cores from the immature area, the shales are characterized by a wide range of Mo, U and Re abundances (Fig. 13). In core 3-19-80-23W5, large variations of Mo (1.2 to 108.2 ppm), U (2.4 to 41.9 ppm) and Re (3.9 to 120.5 ppb) concentrations record changes in redox conditions during deposition at the Famennian-Tournaisian boundary. Scott and Lyons (2012) stated that modern sediments with Mo concentrations exceeding 100 ppm were deposited under long-lived euxinic conditions in a basin that had a good connection to the open ocean. On the contrary, Mo concentrations below 25 ppm are regarded as representing non-euxinic conditions with any dissolved sulfide restricted to the pore waters. Mo concentrations between 25 and 100 ppm indicate a depositional environment ranging from nitrogenous to euxinic (detailed in section 3). In this scenario, if the coeval seawater Mo inventory during Exshaw deposition is assumed to be similar to today, stratigraphically higher shales from 1752.00 to 1752.90 m and from 1754.40 to 1754.79 m that have relatively enriched Mo (35.0 to 48.8 ppm) concentrations and TOC contents (2.6 to 3.6 wt%) suggest suboxic to anoxic bottom waters or, alternatively, euxinic bottom waters associated with rapid bulk sedimentation rates. The peak in TOC and Mo concentrations at 1753.78 m (TOC: 18.5 wt%; Mo: 108.2 ppm) suggests euxinic bottom waters in a short depositional period. By comparison, relatively low trace metal (Mo: 1.2 to 1.7 ppm) and TOC contents (1.0 to 1.5 wt%) are found in stratigraphically lower shales from 1755.66 to 1756.12 m, most likely suggesting an oxic to weakly suboxic depositional environment.

Similarly, in core 13-18-80-23W5, shales from the shallower interval (1747.51–1749.58 m) have relatively moderate Mo (19.9–44.4 ppm) and TOC (2.6 to 3.6 wt%) enrichments, suggesting suboxic/anoxic to euxinic depositional conditions while shales from the deep interval (1750.59–1751.14 m) are characterized by relatively high Mo (99.7–116.7 ppm) and TOC contents (12.8 to 15.3 wt%), probably recording euxinic conditions. In order to precisely assess local redox conditions, additional multiple proxies are combined to better determine the depositional environment.

Based on a Mo EF versus U EF diagram (Fig. 7), most immature shales fall between 1 and 3 times the modern seawater Mo/U EF ratio, with two samples plotting at ~0.3 times the seawater

Mo/U EF ratio. Sample 1753.78 m (core 3-19-80-23W5), 1750.59 m (core 13-18-80-23W5) and 1751.14 m (core 13-18-80-23W5) have both high Mo EF and U EF and thus were probably deposited under euxinic conditions. By contrast, the two samples at 1755.66 m (core 3-19-80-23W5) and 1756.12 m (core 3-19-80-23W5) characterized by low Mo EF and U EF were likely deposited under oxic to weakly suboxic conditions. For the rest of the samples, their trend on the Mo/U EF diagram suggests more intensely suboxic to anoxic to euxinic conditions. This is consistent with the interpretation from trace metal concentrations.

Unlike Mo, U and Re, the V concentrations in core 3-19-80-23W5 and 13-18-80-23W5 are both high and low and yield poor correlations with TOC ($R^2 = 0.02$) (Fig. 10; Fig. 11). Thus, the interpretation of V is less straightforward. According to Scott et al. (2017), it is regarded as "hyper-enrichment" when V concentrations are > 500 ppm, reflecting "hyper-sulfidic" (H_2S up to 10 mM in pore waters or bottom waters) conditions. The Late Devonian–Early Mississippian Bakken Shale (Williston Basin) may have been deposited under such conditions given that Mo concentrations are also high, commonly >200 ppm (Scott et al., 2017). However, the extent of Mo enrichment in Exshaw shales is not regarded as "hyper-enriched" (Mo concentrations do not exceed 150 ppm), which is contradictory to an interpretation of "hyper-sulfidic" conditions. One possibility to cause such high enrichment of V in most samples is the operation of an Fe-Mn particulate shuttle, which accelerates the delivery of V into sediments (Emerson and Huested, 1991; Zhang et al., 2016). Previous studies stated that vanadate is released into anoxic waters as the Fe-Mn oxides are reduced (Emerson and Huested, 1991; Zhang et al., 2016). With the absence of oxygen, the vanadate is reduced to vanadyl form [VO^{2+}] and removed to the sediment. However, when bottom waters are oxygenated, vanadate is commonly released from sediments and causes the depletion of V in sediments (Emerson and Huested, 1991; Zhang et al., 2016). Hence, high V concentrations (> 500 ppm) in most immature shales suggested their bottom waters were anoxic and that the operation of an Fe-Mn particulate shuttle enhanced V enrichment. Based on the poor correlations between Mo EF and V EF (Fig. 14; $R^2 = 0.3$), it showed the impact of the Fe-Mn particulate shuttle on Mo is not as high as V. This may result from the limited H_2S in bottom waters. In the anoxic sediments, the recapture of Mo released from dissolved Fe-Mn particulates requires H_2S while V can be immobilized in anoxic sediments without dissolved sulfide.

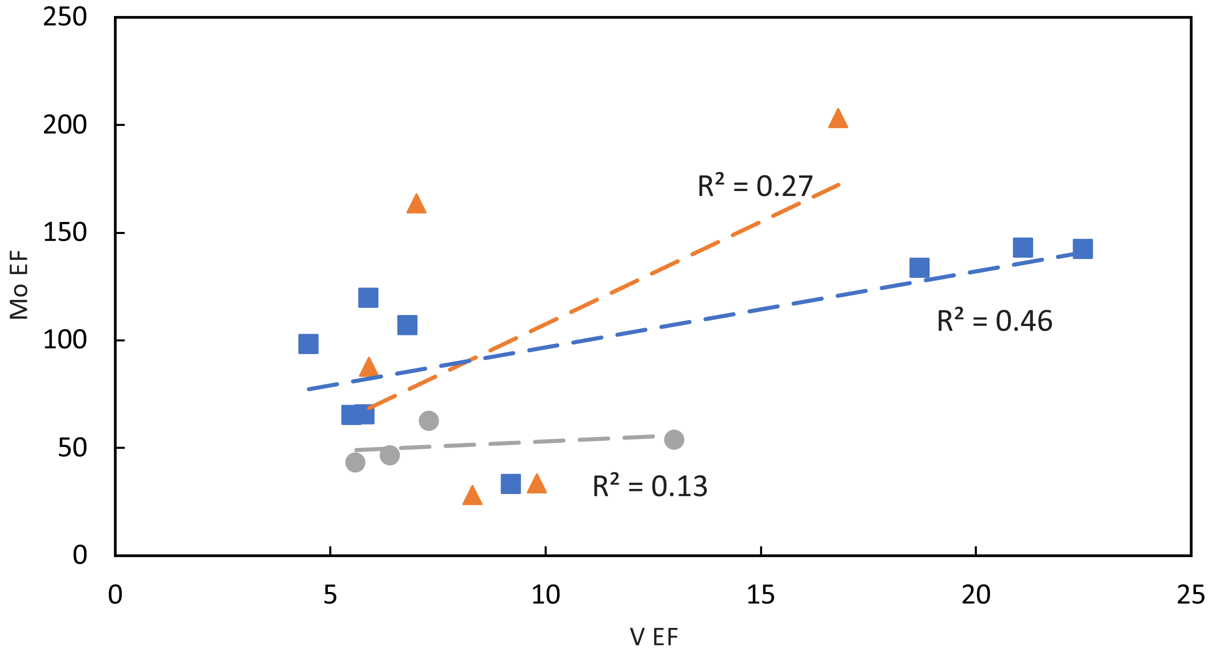

Fig. 14. Geochemical diagram showing cross-plot of Mo EF versus V EF for the Exshaw Formation black shales. Orange triangle refers to data points in immature cores; blue square refers to data points in mature cores; grey circle refers to data points in overmature core.

Both Re/Mo ratios and iron speciation are used to determine local redox conditions (Fig. 8; Crusius et al., 1996). Based on previous studies of modern ocean environments (Crusius et al., 1996; Ross and Bustin, 2009), high Re/Mo ratios ($>15 \times 10^{-3}$) combined with low to negligible Mo enrichments suggested weakly suboxic local conditions while relatively lower Re/Mo ratios (closer to 0.8×10^{-3}) together with high Re and Mo enrichments point to anoxic/sulfidic bottom waters. However, low enrichment of both Re and Mo indicates well-oxygenated bottom waters. Highly reactive Fe, which can react with sulfide in the water column or in sediments, is the aggregation of pyrite Fe, carbonates Fe, ferric oxides Fe, and magnetite Fe ($Fe_{HR} = Fe_{PY} + Fe_{Carb} + Fe_{Ox} + Fe_{Mag}$; Poulton et al., 2004; Poulton and Canfield, 2005). Based on the observation of iron speciation in both modern and ancient sediments, $Fe_{HR}/Fe_{T} > 0.38$ indicates anoxic bottom waters whereas $Fe_{HR}/Fe_{T} < 0.22$ suggests oxic bottom waters (Poulton and Raiswell, 2002; Poulton and Canfield, 2011). Ratios of Fe_{HR}/Fe_{T} between 0.22 and 0.38 point to oxic or anoxic conditions, depending on local factors such as sedimentation rate and depletion of Fe_{HR} during diagenesis and metamorphism (Poulton and Canfield, 2011). Since Fe_{PY} is part of Fe_{HR}, Fe_{PY} is regarded as a minimum for Fe_{HR} and thus Fe_{PY}/Fe_{T} is a minimum value for the Fe_{HR}/Fe_{T} ratio and is used to estimate local redox conditions here. Thus, $Fe_{PY}/Fe_{T} > 0.22$ suggest that no samples unambiguously record oxic bottom water conditions and $Fe_{PY}/Fe_{T} > 0.38$ firmly points to anoxic conditions. In immature shales, a range of Re/Mo ratios (Table 2; 0.4×10^{-3} to 3.3×10^{-3}, averaging $1.4 \times 10^{-3} \pm 1.7 \times 10^{-3}$; 2SD, n = 16) as well as a wide range of Fe_{PY}/Fe_{T} ratios (Fig. 9; 0.21 to 0.41) suggests most samples were deposited under suboxic/anoxic to euxinic conditions.

Mo/TOC ratios are used to evaluate the extent of basin restriction (Algeo and Lyons, 2006; Algeo and Lyons, 2009). The Mo/TOC ratio of euxinic sediments is a function of the uptake of Mo per unit organic matter, and have a positive correlation with the aqueous Mo concentration in bottom waters (Algeo and Lyons, 2006). Thus, a high extent of basin restriction leads to a reduced Mo/TOC ratio in euxinic sediments (Algeo and Lyons, 2006). Immature shales yield a good positive correlation between Mo and TOC ($R^2 = 0.89$), U and TOC ($R^2 = 0.96$), and Re and TOC ($R^2 = 0.78$). Excluding the two low-Mo samples (deposited from oxygenated bottom waters) from 1755.66 m (1.7 ppm) and 1756.12 m (1.2 ppm), the rest of the immature shales yield an Mo/TOC average of 11.0 ± 5.4 ppm/wt% (2SD, n = 14) and a slope of 6.0 ppm/wt% for the regression line on a plot of Mo versus TOC content. The latter value falls between the Black Sea (4.5 ± 1 ppm/wt%) and Cariaco Basin (25 ± 5 ppm/wt%), thus corresponding to a moderately restricted basin. However, this scenario assumes that the Devonian-Mississippian ocean had similar oxygenation levels as today. If the Devonian-Mississippian ocean was more anoxic than today, the global seawater Mo inventory would be smaller. In this case, Mo concentrations in euxinic organic-rich mudrocks would be lower and hence the basin restriction would be weaker than assumed here. Overall, the Exshaw Formation, within the Western Canada Sedimentary Basin, had at least a relatively good connection to open ocean, consistent with paleogeographic reconstructions and higher eustatic sea-level at the Devonian-Mississippian boundary (Smith and Bustin, 1998; Caplan and Bustin, 1999).

6.2.2 Mature area

Similar to the immature area, mature shales are also characterized by fluctuating trace metal concentrations with depth, indicating changes of the chemocline position and redox conditions during deposition. The relatively moderate Mo, U and Re concentrations in shallower intervals of core 14-22-80-2W6 (depth: 2057.80–2059.60 m, Mo: 18.3–23.9 ppm, U: 6.1–6.9 ppm, Re: 11.2–13.2 ppb) and core 6-19-78-25W5 (depth: 2006.33–2007.60 m, Mo: 28.7–95.2 ppm, U:

9.1–31.0 ppm, Re: 23.7–135.1 ppb) indicated generally limited H_2S or intermittently euxinic conditions in the water column. High vanadium (>500 ppm) in shallower intervals suggest an anoxic depositional environment and the operation of Fe-Mn particulate shuttle.

The stratigraphically deeper Exshaw intervals of core 14-22-80-2W6 (2060.08–2060.37 m), core 6-19-78-25W5 (2008.00–2008.37 m) and the whole core 8-29-78-1W6 (2099.0–2099.30 m) are marked by higher Mo concentrations (68.3–129.3 ppm, 91.6–105.0 ppm, and 68.9–103.5 ppm, respectively), U concentrations (22.6–66.1 ppm, 30.3–58.9, and 32.1–32.3 ppm, respectively), and Re concentrations (17.5–316.0 ppb, 123.6–173.3 ppb, and 128.2–194.3 ppb, respectively). These higher concentrations suggest the chemocline was in the water column, indicating more reducing conditions compared to the shallower stratigraphic intervals of cores 14-22-80-2W6 and 6-19-78-25W5. However, samples in the deep interval of core 6-19-78-25W5 and whole core 8-29-78-1W6 showed relatively low vanadium (<500 ppm) but enriched Mo. This is probably because the chemocline moved upwards in the water column, which causes a decrease in delivery of trace metals to sediments via the particulate shuttle because the Fe-Mn oxides dissolved in the anoxic water column (rather than in the sediments), thus released metals back into the water column. In this scenario, the euxinic bottom water conditions permits greater authigenic Mo enrichment than V, as is observed in modern euxinic basins (Scott and Lyons, 2012).

The Re/Mo ratios of samples from the mature area range from 0.2×10^{-3} to 2.8×10^{-3}, averaging $1.2 \pm 1.44 \times 10^{-3}$ (2SD, n = 16), suggesting most mature shales were deposited under anoxic to euxinic conditions. High Fe_{PY}/Fe_T (>0.38) ratios for samples at 2006.69 m, 2007.35 m, 2008.0 m and 2008.37 m in core 6-19-78-25W5 suggest deposition from anoxic bottom waters, whereas other samples with relatively moderate Fe_{PY}/Fe_T (0.22 to 0.31) values are more ambiguous with respect to the redox state of local bottom waters but are consistent with either suboxic or anoxic bottom waters.

The mature shales also yield a good correlation between Mo EF and U EF ($R^2 = 0.83$). All data points are restricted between 1 and 3 times the modern seawater Mo/U EF ratio (Fig. 7). The data points are clearly distributed into two groups. The deeper stratigraphic intervals have higher Mo EF and U EF and shallower stratigraphic intervals are characterized by relatively lower Mo EF and U EF, which is consistent with the previous interpretation of moderate restriction and oxic to weakly suboxic conditions at shallower depths but more intensely suboxic to anoxic to euxinic conditions at deeper depths.

6.2.3 Overmature area

Unlike the mature and immature areas, overmature shales (core 4-23-72-10W6) are characterized by lower TOC and relatively low to moderate trace metal concentrations. The TOC content ranges from 1.3 to 3.5 wt%. Trace metal concentrations are scattered and relatively low to moderate: Mo (1.3–62.7 ppm), U (2.1–20.7 ppm), and Re (6.8–89.3 ppb). Lower TOC and poorer metal-TOC correlations for the overmature shales than other areas suggested the loss of TOC but retention of trace metals (see section 6.1).

The overmature shales are divided into two intervals (shallower interval: 3559.45 to 3565.34 m; deeper interval: 3565.67 to 3570.27 m). The shallower interval is characterized by relatively low Mo (1.3–23.5 ppm), U (2.1–6.5 ppm) and Re (6.7–34.1 ppb) concentrations, as well as relatively high Re/Mo ratios (1.1×10^{-3} to 7.4×10^{-3}, averaging $2.7 \pm 3.92 \times 10^{-3}$; 2SD, n = 15), suggesting that the bottom waters were oxic to suboxic.

By contrast, the deeper shales with relatively higher Mo (10.7–62.7 ppm), U (4.1–20.7 ppm), Re (21.5–89.3 ppb), as well as relatively lower Re/Mo ratios (0.77×10^{-3} to 2.45×10^{-3}, averaging $1.34 \pm 0.92 \times 10^{-3}$; 2SD, n = 11) suggests that local redox conditions were generally more reducing compared to the shallower interval, though there are some overlaps. However, it is difficult to distinguish whether their depositional environment is suboxic or intermittently euxinic. The wide range of vanadium concentrations suggests the operation of an Fe-Mn particulate shuttle was intermittent. High V concentrations (> 500 ppm) in the deeper interval suggest greater delivery of V to sediments by an intense Fe-Mn particulate shuttle than those samples with low V (< 500 ppm) in the shallower interval. Relatively low Fe_{PY}/Fe_T ratios for black shales from the deeper interval (0.21 to 0.31) is consistent with the interpretation of suboxic to anoxic depositional conditions.

The distributions of Mo/U EF ratios are split into two groups. One group is scattered between 0.1 times to 1 times seawater Mo/U EF ratios and the other group is restricted between 1 time to 3 times seawater Mo/U EF ratios. Relatively low Mo/U EF ratios correspond to stratigraphically shallower shales, while high Mo/U EF ratios represent most stratigraphically deeper shales, though there are some overlaps in redox conditions between two intervals.

Based on the observation of geochemical data from the three areas with different maturity, some main observations are summarized here: 1) most samples are deposited under suboxic to anoxic to euxinic conditions and there are some overlaps in redox conditions between the three areas; 2) although the local redox conditions fluctuated, there is a general stratigraphic trend from more reducing to less reducing conditions upwards; 3) the operation of an Fe-Mn particulate shuttle may have had significant impact on the transfer of V to sediments but weaker impact on Mo; and 4) the local sedimentary basin had at least a moderate connection to the open ocean.

6.3 Constraints on the extent of Famennian-Tournaisian ocean anoxia from Mo isotopes and elemental Re and Mo mass balance models

Mo isotopes have been utilized to reconstruct paleo-redox conditions for nearly two decades (e.g., Barling et al., 2001; Siebert et al., 2003, 2006; Arnold et al., 2004; Poulson et al., 2006; Kendall et al., 2009, 2011, 2015; Dahl et al., 2010; Duan et al., 2010; Zhou et al., 2012, 2015; Chen et al., 2015). In the Exshaw Formation, the Mo isotope compositions are relatively low and widely distributed (0.26 to 1.11‰, averaging 0.76 ± 0.51‰, 2SD, n=18) compared to the modern global seawater Mo isotope composition (δ^{98}Mo = ~2.34 ± 0.10‰; Barling et al., 2001; Siebert et al., 2003; Nakagawa et al., 2012; Nägler et al., 2014). Since the samples selected for Mo isotope analysis have elevated Mo and Mo/Al ratios (Table 4), compared to the average crustal value (~1.5 ppm and ~0.19 ppm/wt%, respectively; Taylor et al., 1995), the impact of detrital Mo on the bulk shale δ^{98}Mo is negligible. However, local Mo isotope fractionation between seawater and euxinic sediments could result in fluctuations of Mo isotope compositions in the Exshaw black shales. Thus, to determine whether δ^{98}Mo can represent the coeval global seawater Mo isotope composition, fractionation between the local sediments and seawater during deposition of the Exshaw Formation should be determined. Notably, all immature, mature and overmature areas have some low Mo isotope values and some of them are even conspicuously lower than the modern oceanic input value (~0.55‰; Neely et al., 2018). Isotopically light Mo is preferentially removed to sediments and there is no marine environment where heavy Mo isotopes are preferentially removed from seawater to sediments. Since the oceanic input δ^{98}Mo at the D-M boundary was likely similar to today (because the upper continental crust likely had a similar chemical composition; Kendall et al., 2017) and it is not possible for global seawater to have lower δ^{98}Mo

(< 0.55‰) than the oceanic input value, it is likely that Mo isotope fractionation did occur between the Exshaw Formation black shales and coeval Devonian-Mississippian seawater.

The δ^{98}Mo values in the Exshaw Formation lower black shale member have a wide range from 0.26‰ to 1.11‰, with an average of 0.76 ± 0.51 ‰ (2SD, n=18). As isotopically lighter Mo isotopes are always preferentially removed into sediments, the highest δ^{98}Mo from the Exshaw black shales is most likely to capture the coeval seawater δ^{98}Mo or at least the smallest Mo isotope fractionation between the sediments and seawater. The previous section discussed that the samples chosen for the Mo isotope analysis are characterized by enriched trace metals (Mo, U, Re, V) and most likely to represent an euxinic depositional environment. The highest δ^{98}Mo of 1.11‰ occurs in a sample with relatively low V EF (<10) and suggests that the effects of an Fe-Mn particulate shuttle were limited. Thus, this sample likely comes closest to the coeval seawater δ^{98}Mo.

Bura-Nakić et al. (2018) stated that there is a Mo isotope fractionation of 0.3‰ between dissolved Mo and particulate Mo, even for near-quantitative removal to sediments at high sulfide concentrations. Thus, here I apply a minimum Mo isotope fractionation of 0.3‰ for the Exshaw shales. Although the Exshaw Formation was deposited in an epicontinental sea, it had a relatively good connection to open ocean. Compared to modern analogues (the Black Sea; Cariaco Basin, Saanich Inlet), the Exshaw Formation may be more similar to the deep Cariaco basin or Saanich Inlet with respect to bottom water redox state, specifically weakly euxinic conditions. The Cariaco Basin is characterized by a Mo isotope fractionation of up to 0.8‰. The Saanich Inlet has the Mo isotope fractionation of 1.0‰. Thus, a highest Mo isotope fractionation factor of 1.0‰ is applied for the Exshaw Formation black shales. Then, the coeval seawater δ^{98}Mo is calculated to be 1.4 to 2.1‰. This estimate is consistent with the geographically widespread deposition of black shales during the Hangenberg event, which suggests that the coeval seawater δ^{98}Mo at the D-M boundary should be lower than today (2.34‰).

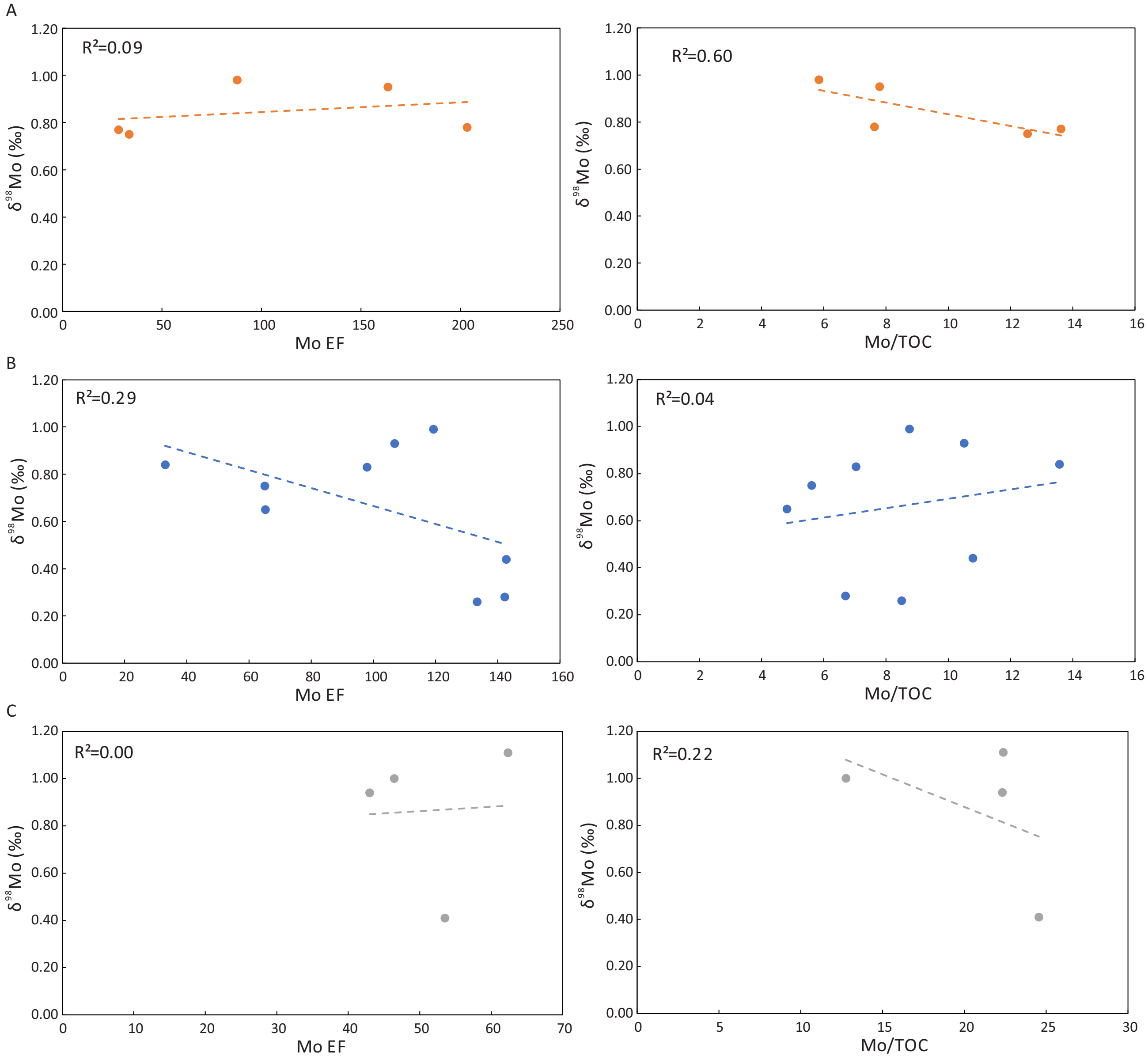

Fig. 15. Geochemical diagrams showing the correlation of δ^{98}Mo versus Mo EF and δ^{98}Mo versus Mo/TOC ratio for the Exshaw Formation black shales. Orange, blue, and grey circles

refer to data points in immature cores (A), mature cores (B) and overmature core (C), respectively. R square values for each sub-diagram are displayed.

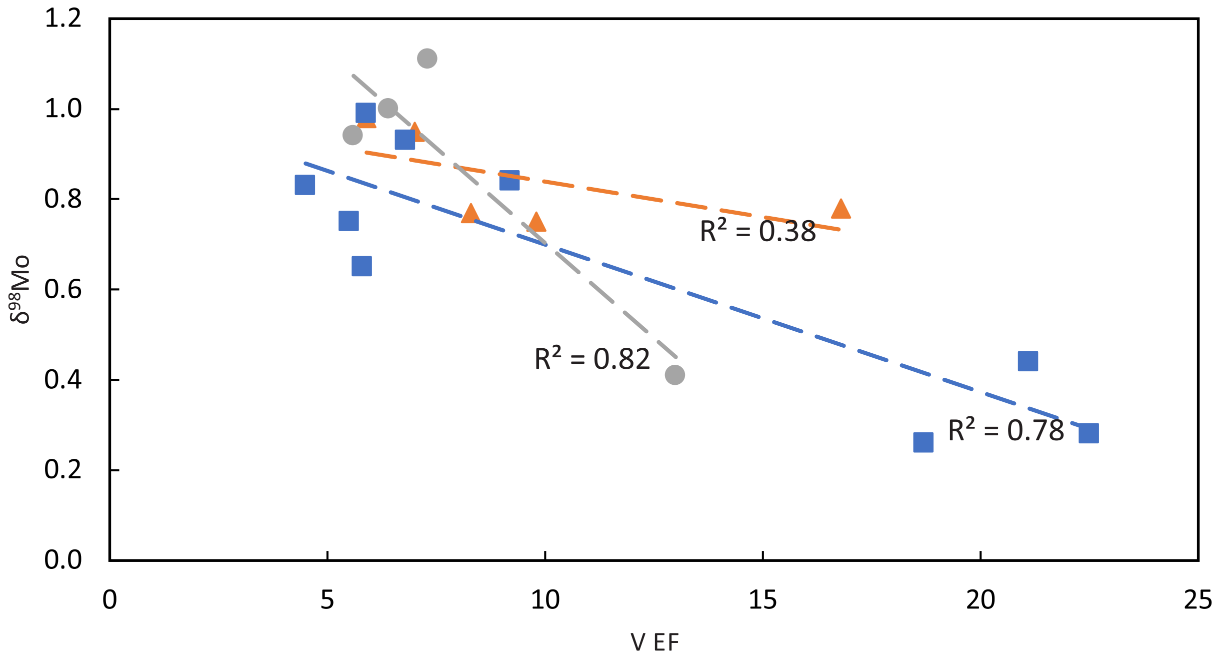

Fig. 16. Geochemical diagram showing cross-plot of δ^{98}Mo versus V EF for the Exshaw Formation black shales. Orange triangle refers to data points in immature cores; blue square refers to data points in mature cores; grey circle refers to data points in overmature core.

There are some conspicuously low δ^{98}Mo values from samples at 2060.08 m (0.44‰) and 2060.37 m (0.28‰) in core 14-22-80-2W6, 2007.35 m (0.26‰) in core 6-19-78-25W5, and 3565.67 m (0.41‰) in core 4-23-72-10W6 but with relatively high Mo concentrations (68.3 ppm, 129.3 ppm, 133.4 ppm, and 46.9 ppm, respectively). Low δ^{98}Mo values in black shales point to widespread ocean euxinia whereas enriched Mo concentrations suggest ocean oxygenation (Barling et al., 2001; Arnold et al., 2004; Scott et al., 2008; Dahl et al., 2010; Kendall et al., 2015).

Thus, a larger Mo isotope fractionation likely occurred during deposition of these samples. This may have happened because of both the non-quantitative removal of Mo from bottom waters, and/or incomplete conversion of molybdate to tetrathiomolybdate under weakly euxinic conditions, and the operation of an Fe-Mn particulate shuttle. Although correlations between δ^{98}Mo and Mo/TOC as well as between δ^{98}Mo and Mo EF in the three areas (Fig. 15) are not significant, there are some correlations between δ^{98}Mo and V EF (Fig. 16; $R^2>0.4$). Those four samples with low δ^{98}Mo have relatively high Mo EF (>50) and V EF (>10). This observation suggests an Fe-Mn particulate shuttle occurred at that depositional period and delivered isotopically light Mo to sediments (Herrmann et al., 2012; Kendall et al., 2015). There could be an impact by an Fe-Mn particulate shuttle on other samples with relatively low Mo isotope compositions (<1.0‰) and high V concentrations (>500 ppm), but the extent is not as high as those four V-rich samples. For the samples with low V concentrations (<500 ppm), the effects of an Fe-Mn particulate shuttle on their Mo isotope compositions are probably more limited.

Therefore, summarizing the above cases, the contemporary seawater Mo isotope composition at the Devonian-Mississippian boundary was estimated to be 1.4 to 2.1‰, which is generally consistent with some other studies that suggested seawater δ^{98}Mo values of ~1.5 to 2.0‰ in the Famennian (Dahl et al., 2010; Magnall et al., 2018).

A Mo isotope mass balance model was utilized to estimate the global extent of ocean euxinia. A summary of the model is described below, with further details provided in Goldberg et al. (2016).

Under steady state conditions, the total Mo fluxes to the ocean ($F_{sources}$) is assumed to be equal to the total Mo output (F_{sinks}) to various sinks (Rodhe, 1992; Sarmiento and Gruber, 2006).

The residence time (τ) of Mo in seawater is assigned to the global marine Mo inventory (M) in proportion to all source or sink fluxes (F):

$$M/\tau = F_{sources} = F_{sinks}$$

The flux of each sink has a relationship with the areal extent (A) of each sink (i) and the burial rate *(R)* into each sink:

$$F_i = A_i \times R_i$$

There are three sinks for Mo: oxic sink (f_{ox}), intermediate sink (“sulfidic at depth”, f_{sad}), and euxinic sink (f_{eux}). Thus,

$$F_{sinks} = f_{ox} + f_{sad} + f_{eux}$$

The respective Mo isotope signatures (δ_{ox}, δ_{sad} and δ_{eux}) are linked with a Mo isotope mass balance equation, where input δ^{98}Mo is equal to the sinks:

$$\delta_{input} = f_{ox}\delta_{ox} + f_{sad}\delta_{sad} + f_{eux}\delta_{eux}$$

Seawater Mo isotope signature is denoted as δ_{SW}. Thus, oceanic δ^{98}Mo is defined as:

$$\delta_{SW} = \delta_{input} - f_{ox}\delta_{ox} + f_{sad}\delta_{sad} + f_{eux}\delta_{eux}$$

In order to calculate the ancient (k) Mo budget, a function is applied, where the Mo burial rates are first-order proportional to the Mo inventory:

$$R_{i(k)} = (R_i \times M)/M_{(k)}$$

Then, the rate of change of the Mo inventory is showed as:

$$\mathrm{d}M/\mathrm{d}t = F_{sinks} - M/\tau$$

Then, the burial forcing function is converted to:

$$\frac{\tau}{\tau_{(k)}} = \frac{f_{ox}A_{ox(k)}}{A_{ox}} + \frac{f_{sad}A_{sad(k)}}{A_{sad}} + \frac{f_{eux}A_{eux(k)}}{A_{eux}}$$

Applying this Mo isotope mass balance model, the estimated coeval seawater Mo isotope composition (1.4 to 2.1‰) suggests that the euxinic seafloor covered less than 5% at the Famennian-Tournaisian boundary (Dahl et al., 2011; Goldberg et al., 2016).

Some other models related to seafloor redox distribution were established to estimate ocean anoxia and euxinia: Re mass balance model (Sheen et al., 2018) and Mo mass balance model (Reinhard et al., 2013). The Mo mass balance model is very similar to Re expect for one of the marine sinks (euxinic for Mo but anoxic for Re). Here, a summary of the Re mass balance model is presented, with full details provided in Sheen et al. (2018).

The global seawater Re reservoir can be expressed as the difference between mass entering (M_{in}) and exiting (M_{out}) the system:

$$M_{in} - M_{out} = \int_0^V [\mathrm{Re}]\, dV, \text{ (I)}$$

where [Re] refers to dissolved Re concentrations, V refers to global ocean volume. By taking the derivative with respect to time t, the equation converts to

$$F_{in} - F_{out} = \frac{d}{dt}\int_0^V [\mathrm{Re}]\, dV, \text{ (II)}$$

where F_{in} and F_{out} represents source and sink, respectively. Assuming a steady-state condition, the flux entering is equal to the flux out ($F_{in} = F_{out}$).

Rivers are the major input flux of Re to the oceans and is assumed to be broadly constant for an oxygenated Phanerozoic atmosphere. There are three main sinks (oxic, suboxic, anoxic) for Re removal to sediments. Thus,

$$F_{in} = F_{oxic} + F_{suboxic} + F_{anoxic}, \text{ (III)}$$

the sink terms are each defined as:

$$F_i = kA_ib_i, \text{ (IV)}$$

where A_i is the seafloor area for each setting; b_i is the burial rate for each setting in the modern ocean. The non-dimensional coefficient k relates Re burial flux to seawater concentration is showed as:

$$k = \left(\frac{[\mathrm{Re}]'}{[\mathrm{Re}]_{\mathrm{M}}}\right)^{\alpha}, \text{(V)}$$

where $[\mathrm{Re}]'$ refers to seawater Re concentrations for the investigated time interval; $[\mathrm{Re}]_{\mathrm{M}}$ refers to the modern seawater Re concentration. For a first order mass-balance approach, α is set to unity and represent that the burial rate of a metal within a specific sink setting have a linear relationship with the size of its seawater reservoir.

Combining and rearranging equations (III)-(V), a generalized expression for seawater Re concentration under new steady-state conditions, with respect to the global Re oceanic mass balance, is yielded here:

$$[\mathrm{Re}]' = [\mathrm{Re}]_{\mathrm{M}} \left(\frac{F_{in}}{\sum A_i b_i}\right), \text{(VI)}$$

where $[\mathrm{Re}]'$ changes as a function of A_i and b_i.

Authigenic Re enrichment in anoxic sediments thus is controlled by the general equation:

$$b_a' = b_a \left(\frac{[\mathrm{Re}]'}{[\mathrm{Re}]_{\mathrm{M}}}\right), \text{(VII)}$$

where b_a' is the anoxic burial rate; b_a is the modern average anoxic burial rate. A perturbation in the form of progressive expansion of anoxia is assumed to model change to the marine Re cycle in ancient oceans. Predicted authigenic Re enrichment in open-ocean anoxic sediments is defined as $[\mathrm{Re}]_{\mathrm{pred}}$, and is the output of the model.

Since Re is not affected by an Fe-Mn particulate shuttle (Colodner et al., 1993), the anoxic shales from the Exshaw Formation are used to estimate the global extent of ocean anoxia using Re mass balance model in Sheen et al. (2018) (Fig. 17). It yields an average Re concentration of 103

± 86 ppb (1SD, n=18), suggesting that the average ocean area of anoxic seafloor at Famennian-Tournaisian boundary was between 0.1% and 2%. For the Mo mass balance model, in order to minimize the effects of an Fe-Mn particulate shuttle, samples with Mo enrichment >25 ppm and V enrichment <500 ppm were selected to estimate the global extent of ocean euxinia. The average Mo enrichment of these samples is 81 ± 24 ppm (1SD, n=7). Inputting this value into the Mo mass balance model (Fig. 18) yields an average estimate of 0.4% to 1.6% for the extent of ocean euxinia. Since the Exshaw Formation was deposited in a partially restricted epeiric sea rather than a fully open-ocean setting, the global extent of anoxic and euxinic seafloor could be lower than the estimation from these models. Some other black shale formations (e.g., Bakken Formation Shale; Sunbury Shale) at the D-M boundary yield similar or higher Mo and Re concentrations, which points to an overall well-oxygenated global ocean (Rimmer, 2004; Scott et al., 2017).

The extent of modern euxinic seafloor is suggested to be 0.021 to 0.063% (Poulson Brucker et al., 2009; Kendall et al., 2009; Scott et al., 2008) and the extent of modern anoxic seafloor is proposed to be ~0.35% (Veeh, 1967; Bertine and Turekian, 1973; Anbar, 2004). Compared to modern ocean seafloor, our geochemical data suggests that the extent of ocean anoxia/euxinia at Famennian-Tournaisian boundary is wider than the modern ocean but also that the majority of the Famennian-Tournaisian ocean was oxygenated.

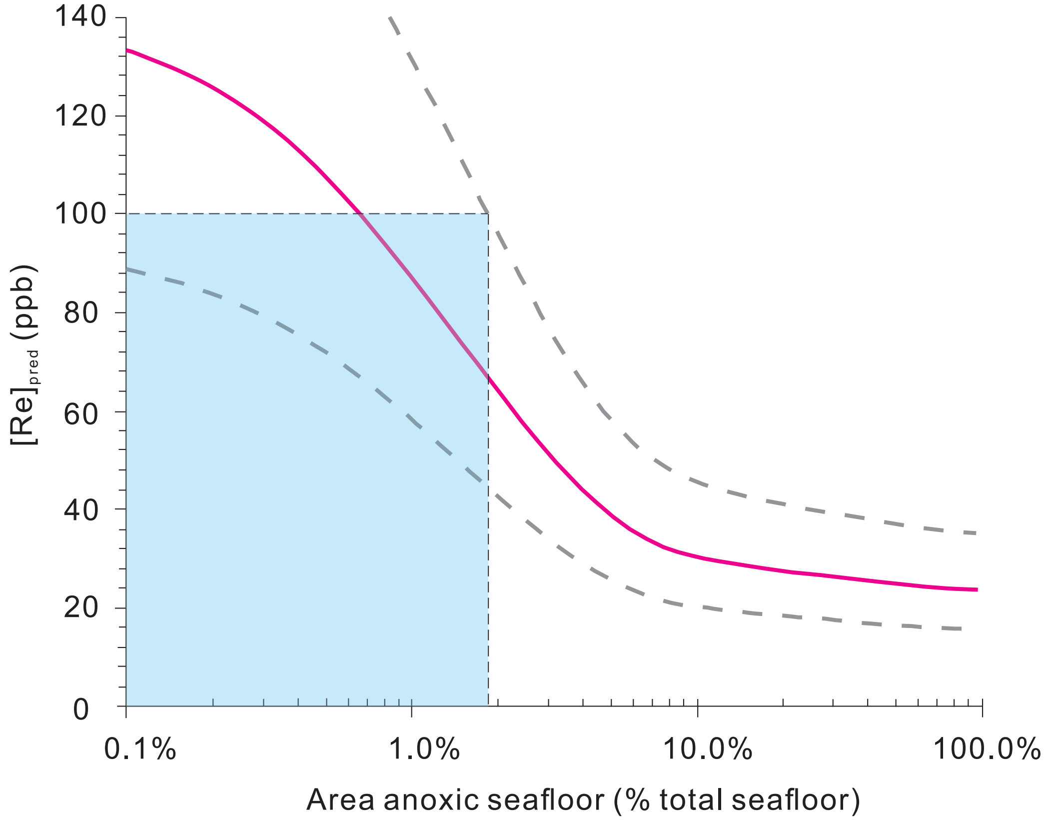

Fig. 17. Re mass balance model for Devonian-Mississippian Exshaw Formation. [Re]$_{pred}$ versus area of anoxic seafloor (red curve). Dashed lines refer to a factor of 1.5 above and below a bulk mass accumulation rate of 0.01 g cm^{-2}yr^{-1}, constrained from the Cariaco Basin. Modified from Sheen et al. (2018).

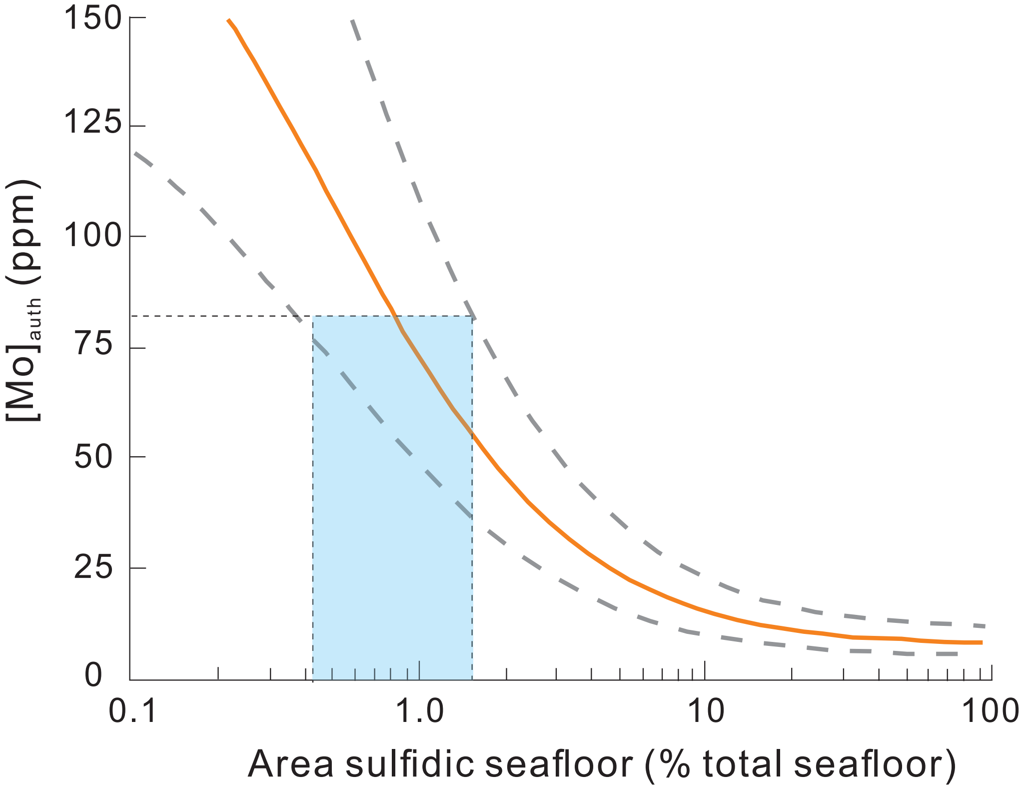

Fig. 18. Mo mass balance model for Devonian-Mississippian Exshaw Formation. Authigenic Mo versus area sulfidic seafloor (orange curve). Dashed lines refer to a factor of 1.5 above and below a bulk mass accumulation rate of 0.01 g cm^{-2}yr^{-1}. Modified from Reinhard et al. (2013).

6.4. Implications for the Famennian-Tournaisian Hangenberg mass extinction

In this study, the geochemical data from the Exshaw Formation suggested the seawater at the Famennian-Tournaisian boundary was overall well-oxygenated but the extent of ocean anoxia and euxinia was wider than today. Although the mechanisms for triggering the Hangenberg mass extinction event are still being debated, ocean anoxia/euxinia is a leading cause among them. Some previous studies also reported evidence for expanded ocean anoxia, including the observation of changes in faunal composition, lithological facies, geochemical and isotope data (Caplan et al., 1996; Caplan and Bustin, 1999; Caplan and Bustin, 2001; Marynowski and Filipiak, 2007; Marynowski et al., 2012; Formolo et al., 2014; Matyja et al., 2015; Carmichael et al., 2016; Martinez et al., 2018; Kumpan et al., 2019; Paschall et al., 2019). The globally distributed Hangenberg Shale event covered ~21% of the Famennian depositional area within epicontinental seas, including shales at Montagne Noire, France (Feist, 1990), Bohemian region (Chlupac, 1988), former Yugoslavia (Krstic et al., 1988), Exshaw shales of western Canada, Woodford shales of the Anadarko Platform, Antrim shales and Bakken Formation of the Williston Basin, Michigan and Illinois, and Changshun shales of South China (Bai and Ning, 1988; Xu et al., 1989). The changes of the global carbon cycle and expanded hypoxia/anoxia were recorded by both positive carbonate and organic carbon isotope excursions in Hangenberg black shales and equivalents around the D-M boundary (Kaiser 2005; Kumpan et al., 2013; Qie et al., 2015; Kaiser et al., 2016). In addition, the presence of green sulfur bacteria suggested the expansion of anoxia into the photic zone in continental margins (Marynowski and Filipiak, 2007; Marynowski et al., 2012).

Although the triggering mechanisms for the Late Devonian ocean anoxia are still contentious, some previous hypotheses were proposed to explain the ocean anoxia. For instance, the upwelling of nutrient-rich waters associated with eustatic transgression and a sea-level rise is regarded a mechanism for ocean anoxia with the Hangenberg Black Shale (HBS) event (Caplan et al., 1996; Smith and Bustin, 1998; Caplan and Bustin, 1999; Algeo et al., 2007; Cramer et al., 2008; Formolo et al., 2014; Komatsu et al., 2014). Both geochemical data (e.g., $\delta^{18}O_{carb}$, $\delta^{13}C_{carb}$ isotope positive excursion in carbonates) and paleontological evidence (e.g., the appearance of diversification of small-eyed/blind trilobites and zooplankton) suggested nutrient-rich conditions just prior to D-M boundary (Caplan and Bustin, 1999). Some other studies suggested that the eutrophication from the runoff from terrestrial sources leads to HBS anoxia (Caplan and Bustin, 1998; Averbuch et al., 2005; Qie et al., 2015; Bábek et al., 2016; Carmichael et al., 2016; Liu et al., 2016). Liu et al. (2016) stated that relatively low $\delta^{15}N$ indicated strong microbial nitrogen fixation, probably resulting from increased denitrification and marine anoxia.

Climate cooling as well as expanded glaciation at the D-M boundary could also be factors to cause the mass extinction (Brezinski et al., 2008; Isaacson et al., 2008). A positive carbon isotope excursion in carbonates response to the Hangenberg mass extinction event was reported from Nevada, Utah (Saltzman, 2005) and Colorado (Myrow et al., 2011, 2014), suggesting the elevated organic burial rates, consistent with the drawdown of CO_2 and global cooling. Subsequently, a worldwide regression followed and triggered glaciation on Gondwana (Kaiser et al., 2006). Previous studies stated that the Hangenberg Sandstone is linked to Gondwana glaciation and glacio-eustatic sea-level fall, evidenced from glaciogenic deposits as well as the presence of regressive marine deposits (Caputo et al., 2008; Isaacson et al., 2008; Kaiser et al., 2016). Some other studies stated the D-M boundary glaciation was a multiphase event with several glacial/interglacial phases (Marshall 2010; Wicander et al., 2011). The first glaciation episode of Bolivia probably occurred in the upper Famennian with subsequent glacial and interglacial episodes in the LL, LE and LN miospore zones (Wicander et al., 2011). The widespread deposition of regressive sediments (e.g., Rhenish Hangenberg Shales and Hangenberg Sandstone) (Paproth, 1986; Kaiser et al., 2011; Kaiser et al., 2016) is linked to the major sea-level fall and high-latitude glaciation pulse, which is time-equivalent to the deposition of the top of the Exshaw black shale member and overlying siltstone member.

Although the volcanism at the D-M boundary is still being debated, the presence of volcanic ash/tuff in Spain and Portugal (Gonzalez et al., 2006), South China (Liu et al., 2012), Poland (Filipiak and Racki, 2010; Marynowski et al., 2012) and Ireland (Pracht and Batchelor, 1998) suggested that volcanic activity occurred both locally and globally at the D-M boundary. Massive volcanism may be a factor to trigger the Hangenberg mass extinction event, based on the observation of abnormally high bulk Hg concentrations in different lithologies in Uzbekistan, Germany (Racki et al., 2018) and Vietnam (Paschall et al., 2019). Large Igneous Provinces (LIPs) in the Late Devonian, represented by the Viluy Traps (364.4 ± 1.7 Ma) on the Siberian Platform as well as magmatic activity in the south China Terrane were also reported (Chen et al., 2001, Chen et al., 2006; Kravchinsky, 2012; Liu et al., 2012; Ricci et al., 2013).

Therefore, from the above discussion, the Late Devonian Hangenberg mass extinction events were probably driven by multiple factors rather than one single mechanism. Our geochemical data suggested that ocean anoxia/euxinia may play a role in triggering the event.

7. Conclusions

The Exshaw Formation has experienced hydrocarbon maturation and been divided into three districts from east to west: immature area, mature area, and overmature area, respectively. The geochemical data (trace metals as well as Mo and S isotopes) from the Exshaw Formation provide insights for the local and global redox conditions at the D-M boundary. Statistically, the unpaired t-test results for Mo and S isotope data among each area indicated that there is no significant difference with the degree of maturity. The low pyrite sulfur isotope values and large sulfur isotope fractionation between pyrite and original seawater sulfate indicated that microbial sulfate reduction (MSR) occurred during early diagenesis rather than thermochemical sulfate reduction (TSR). Although there is some loss of TOC from the overmature shales, the trace metals likely remained immobilized. Thus, the effects of hydrocarbon maturation on trace metals as well as Mo and S isotopes are limited and the depositional environment of the Exshaw Formation can be reconstructed using these geochemical proxies.

Although all immature, mature and overmature shales are characterized by fluctuations in the TOC content and trace metal concentrations, recording changes of chemocline and redox conditions during the depositional process, there is a general upward stratigraphic trend from more reducing to less reducing conditions. Most samples in three areas are marked by moderate to high Mo, U, Re enrichments, indicating that their depositional environment was probably suboxic to anoxic to euxinic. High enrichment of V (>500 ppm) in some samples suggested that there is an operation of Fe-Mn particulate shuttle. Re/Mo ratios and iron speciation also provides the evidence of suboxic, anoxic, and euxinic bottom waters for each area. Moderate Mo/TOC and Mo/U EF ratios for the more Mo-rich samples in all three areas suggest the basin was equal to or less than moderately restricted.

The most Mo-rich black shales in all three areas are most likely to be deposited from euxinic bottom waters and yield δ^{98}Mo values from 0.3‰ to 1.1‰. The conspicuously low values could result from large Mo isotope fractionations at the depositional locality because of weakly euxinic conditions and/or the operation of an Fe-Mn particulate shuttle. Applying a Mo isotope fractionation factor of 0.3‰ to 1.0‰ to the highest δ^{98}Mo in the Exshaw black shales, the coeval seawater δ^{98}Mo at the Famennian-Tournaisian boundary may have been 1.4‰ to 2.1‰, which is less than today's seawater δ^{98}Mo. A Mo isotope mass balance model suggests ocean euxinia was less than 5%. Mass-balance models coupled with the magnitude of Mo and Re enrichments in the most euxinic/anoxic Exshaw shales suggest that the extent of euxinic and anoxic seafloor was each <2%. Thus, although the ocean at the Famennian-Tournaisian boundary is overall well-oxygenated, the ocean anoxia/euxinia was wider at that time than today.

Thus, the end-Devonian Hangenberg mass extinction event was probably driven by multiple factors such as sea-level change, glaciation, climate cooling, volcanism, and ocean anoxia. Our geochemical data support that the ocean anoxia may play a role in triggering the event.

References

Abanda, P. A. and Hannigan, R. E. (2006). Effect of diagenesis on trace element partitioning in shales. *Chemical Geology*. 230, 42-59.

Algeo, T. J. Lyons, T. W. Blakey, R. C. and Over, D. J. (2007). Hydrographic conditions of the Devono–Carboniferous North American Seaway inferred from sedimentary Mo–TOC relationships. *Palaeogeography, Palaeoclimatology, Palaeoecology*. 256(3-4), 204-230.

Algeo, T. J. and Lyons, T. W. (2006). Mo-total organic carbon covariation in modern anoxic marine environments: Implications for analysis of paleoredox and paleohydrographic conditions. *Paleoceanography*. 21(1).

Algeo, T. J. and Tribovillard, N. (2009). Environmental analysis of paleoceanographic systems based on molybdenum-uranium covariation. *Chemical Geology*. 268(3), 211-225.

Algeo, T. J. and Maynard, J. B. (2004). Trace-element behavior and redox facies in core shales of Upper Pennsylvanian Kansas-type cyclothems. *Chemical Geology*. 206, 289-318.

Amrani, A. (2014). Organosulfur compounds: molecular and isotopic evolution from biota to oil and gas. *Annual Review Earth and Planetary Sciences*. 42, 733-768.

Anbar, A. D., Creaser, R. A., Papanastassiou, D. A. and Wasserburg, G. J. (1992). Rhenium in seawater: Confirmation of generally conservative behavior. *Geochimica et Cosmochimica Acta*. 56, 4099-4103.

Andersen, M. B., Matthews, A., Vance, D., Bar-Matthews, M., Archer, C., and de Souza, G. F. (2018). A 10-fold decline in the deep Eastern Mediterranean thermohaline overturning circulation during the last interglacial period. *Earth and Planetary Science Letters*. 503, 58-67.

Anderson, R. F., Fleisher, M. Q., and LeHuray, A. P. (1989). Concentration, oxidation state, and particulate flux of uranium in the Black Sea. *Geochimica et Cosmochimica Acta*. 53(9), 2215-2224.

Ardakani, O. H., Chappaz, A., Sanei, H., and Mayer, B. (2016). Effect of thermal maturity on remobilization of molybdenum in black shales. *Earth and Planetary Science Letters*. 449, 311-320.

Armstrong, J. G., Parnell, J., Bullock, L. A., Perez, M., Boyce, A. J., and Feldmann, J. (2018). Tellurium, selenium and cobalt enrichment in Neoproterozoic black shales, Gwna Group, UK: Deep marine trace element enrichment during the Second Great Oxygenation Event. *Terra Nova*. 30(3), 244-253.

Arnold, G. L., Anbar, A. D., Barling, J. and Lyons, T. W. (2004). Molybdenum isotope evidence for widespread anoxia in mid-Proterozoic oceans. *Science*. 304(5667), 87-90.

Arnold G., Lyons T., Gordon G. and Anbar A. (2012) Extreme change in sulfide concentrations in the Black Sea during the Little Ice Age reconstructed using molybdenum isotopes. *Geology*. 40:59-598.

Averbuch, O., Tribovillard, N., Devleeschouwer, X., Riquier, L., Mistiaen, B. and Van Vliet-Lanoe, B. (2005). Mountain building-enhanced continental weathering and organic carbon burial as major causes for climatic cooling at the Frasnian–Famennian boundary (c. 376 Ma)?. *Terra nova*, 17(1), 25-34.

Azrieli-Tal, I., Matthews, A., Bar-Matthews, M., Almogi-Labin A., Vance, D., Archer, C. and Teutsch, N. (2014). Evidence from molybdenum and iron isotopes and molybdenum-uranium covariation for sulphidic bottom waters during Eastern Mediterranean sapropel S1 formation. *Earth and Planetary Science Letters*. 393, 231-242.

Bábek, O., Kumpan, T., Kalvoda, J., and Grygar, T. M. (2016). Devonian/Carboniferous boundary glacioeustatic fluctuations in a platform-to-basin direction: A geochemical approach of sequence stratigraphy in pelagic settings. Sedimentary geology, 337, 81-99.

Bai, S., Ning, Z. (1988). Faunal change and events across the Devonian–Carboniferous boundary of Huangmao Section, Guangxi, South China. In: McMillan, N.J., Embrey, A.F., Glass, D.J. (Eds.), Devonian of the World. *Proc. Can. Soc. Pet. Geol. Int. Symp.*, Devonian System III, pp. 147–157.

Barling, J., Arnold, G. L. and Anbar, A. D. (2001). Natural mass-dependent variations in the isotopic composition of molybdenum. *Earth and Planetary Science Letters.* 193, 447-457.

Barnes, C. E., and Cochran, J. K. (1990). Uranium removal in oceanic sediments and the oceanic U balance. *Earth and Planetary Science Letters.* 97(1), 94-101.

Becker, R. T., House, M. R. (1994). Kellwasser events and goniatite successions in the Devonian of the Montagne Noire with comments on possible causations. *Courier Forschungsinstitut Senckenberg*. 169, 112-114.

Berner, R. A. and Raiswell, R. (1983). Burial of organic carbon and pyrite sulfur in sediments over Phanerozoic time: a new theory. *Geochimica et Cosmochimica Acta.* 47, 855-862.

Bertine, K. K., and Turekian, K. K. (1973). Molybdenum in marine deposits. *Geochimica et Cosmochimica Acta*, 37(6), 1415-1434.

Bond, D., Wignall, P. B. and Racki, G. (2004). Extent and duration of marine anoxia during the Frasnian-Famennian (Late Devonian) mass extinction in Poland, Germany, Austria and France. *Geological Magazine*. 141, 173-193.

Brand, U., Legrand-Blain, M. and Streel, M. (2004). Biochemostratigraphy of the DCB global stratotype section and point, Griotte Formation, La Serre, Montagne Noire, France. *Palaeogeography, Palaeoclimatology, Palaeoecology*. 205, 337-357.

Breit, G. N. and Wanty, R. B. (1991). Vanadium accumulation in carbonaceous rocks: a review of geochemical controls during deposition and diagenesis. *Chemical. Geology*. 91, 83-97.

Brezinski, D. K., Cecil, C. B., Skema, V. W., and Stamm, R. (2008). Late Devonian glacial deposits from the eastern United States signal an end of the mid-Paleozoic warm period. Palaeogeography, Palaeoclimatology, Palaeoecology, 268(3-4), 143-151.

Brown, S. T., Basu, A., Ding, X., Christensen, J. N. and DePaolo, D. J. (2018). Uranium isotope fractionation by abiotic reductive precipitation. Proceedings of the National Academy of Sciences, 115(35), 8688-8693.

Brumsack, H. J. (1980). Geochemistry of Cretaceous black shales from the Atlantic Pcean (DSDP Legs 11, 14, 36 and 41). Chemical Geology, 31, 1-25.

Buggisch, W. and Joachimski, M. M. (2006). Carbon isotope stratigraphy of the Devonian of Central and Southern Europe. *Palaeogeography, Palaeoclimatology, Palaeoecology*. 240, 68-88.

Bura-Nakić, E., Andersen, M. B., Archer, C., De Souza, G. F., Marguš, M., and Vance, D. (2018). Coupled Mo-U abundances and isotopes in a small marine euxinic basin: Constraints on processes in euxinic basins. Geochimica et Cosmochimica Acta, 222, 212-229.

Calvert, S.E., Thode, H.G., Yeung, D., Karlin, R.E. (1996). A stable isotope study of pyrite formation in the late Pleistocene and Holocene sediments of the Black Sea. *Geochimica et Cosmochimica Acta.* 60, 1261–1270.

Canfield, D. E. (2001). Isotope fractionation by natural populations of sulfate-reducing bacteria. *Geochimica et Cosmochimica Acta.* 65, 1117-1124.

Caplan, M. L. and Bustin, R. M. (1998). Palaeoceanographic controls on geochemical characteristics of organic-rich Exshaw mudrocks: role of enhanced primary production. *Organic Geochemistry*. *30*(2-3), 161-188.

Caplan, M. L., and Bustin, R. M. (1999). Devonian–Carboniferous Hangenberg mass extinction event, widespread organic-rich mudrock and anoxia: causes and consequences. Palaeogeography, Palaeoclimatology, Palaeoecology, 148(4), 187-207.

Caplan, M. L., and Bustin, R. M. (2001). Palaeoenvironmental and palaeoceanographic controls on black, laminated mudrock deposition: example from Devonian–Carboniferous strata, Alberta, Canada. Sedimentary Geology, 145(1-2), 45-72.

Caplan, M. L., Marc Bustin, R., and Grimm, K. A. (1996). Demise of a Devonian-Carboniferous carbonate ramp by eutrophication. Geology, 24(8), 715-718.

Caputo, M. V., de Melo, J. H. G., Streel, M., Isbell, J. L., and Fielding, C. R. (2008). Late Devonian and early Carboniferous glacial records of South America. Geological Society of America Special Papers, 441, 161-173.

Carmichael, S. K., Waters, J. A., Batchelor, C. J., Coleman, D. M., Suttner, T. J., Kido, E., ... and Chadimová, L. (2016). Climate instability and tipping points in the Late Devonian: detection of the Hangenberg Event in an open oceanic island arc in the Central Asian Orogenic Belt. Gondwana Research, 32, 213-231.

Carmichael, S. K., Waters, J. A., Suttner, T. J., Kido, E., DeReuil, A. A. (2014). A new model for the Kellwasser anoxia events (Late Devonian): shallow water anoxia in an open oceanic setting in the Central Asian Orogenic Belt. *Palaeogeography, Palaeoclimatology, Palaeoecology*. 399, 394-403.

Chappaz, A., Lyons, T. W., Gregory, D. D., Reinhard, C. T., Gill, B. C., Li, C. and Large, R. R. (2014). Does pyrite act as an important host for molybdenum in modern and ancient euxinic sediments. *Geochimica et Cosmochimica Acta.* 126, 112-122.

Chen, D., Tucker, M.E., Zhu, J., Jiang, M., 2001. Carbonate sedimentation in a starved pull-apart basin, Middle to late Devonian, southern Guilin, South China. Basin Res. 13, 141–167.

Chen, D.Z., Qing, H.R., Yan, X., Li, H., 2006. Hydrothermal venting and basin evolution (Devonian, South China): Constraints from the rare earth element geochemistry of chert. Sediment. Geol. 183, 203–216

Chen, X., Wu, Z., Xu, S., Wang, L., Huang, R., Han, Y., Ye, W., Xiong, W., Han, T., Long, G., Wang, Y., He, Y., Cai, Y., Sheng, P. and Wang, Y. (2015). Probing the electron states and metal-insulator transition mechanisms in molybdenum disulphide vertical heterostructures. *Nature communications*. 6.

Chen, D. Z. and Tucker, M. E. (2004). Palaeokarst and its implication for the extinction event at the Frasnian–Famennian boundary (Guilin, South China). *Journal of the Geological Society of London.* 161, 895-898.

Chen, J., Zhao, L., Algeo, T. J., Zhou, L., Zhang, L., and Qiu, H. (2019). Evaluation of paleomarine redox conditions using Mo-isotope data in low-[Mo] sediments: A case study from the Lower Triassic of South China. Palaeogeography, Palaeoclimatology, Palaeoecology, 519, 178-193.

Cheng, M., Li, C., Chen, X., Zhou, L., Algeo, T. J., Ling, H. F., ... and Jin, C. S. (2018). Delayed Neoproterozoic oceanic oxygenation: evidence from Mo isotopes of the Cryogenian Datangpo Formation. Precambrian Research, 319, 187-197.

Chlupac, I. (1988). The Devonian of Czechoslovakia and its stratigraphic significance.

Clark, S., Day, J., Ellwood, B., Harry, R. and Tomkin, J. (2009). Astronomical tuning of integrated Upper Famennian–Early Carboniferous faunal, carbon isotope and high resolution magnetic susceptibility records: Western Illinois Basin. *SDS Newsletter*. 24, 27–35.

Copper, P. (2002). Reef development at the Frasnian/Famennian mass extinction boundary. *Palaeogeography, Palaeoclimatology, Palaeoecology*. 181(1-3), 27-65.

Cole, D., Myrow, P. M., Fike, D. A., Hakim, A. and Gehrels, G. E. (2015). Uppermost Devonian (Famennian) to Lower Mississippian events of the western U.S.: stratigraphy, sedimentology, chemostratigraphy, and detrital zircon geochronology. *Palaeogeography,* Palaeoclimatology, Palaeoecology. 427, 1-19.

Coleman, M.L., Raiswell, R. (1995). Source of carbonate and origin of zonation in pyritiferous carbonate concretions: evaluation of a dynamic model. Am. J. Sci. 295, 282–308.

Colodner D., Sachs J., Ravizza G., Turekian K., Edmond J. and Boyle E. (1993) The geochemical cycle of rhenium: a reconnaissance. *Earth and Planetary Science Letters*. 117, 205-221.

Courtillot, V., Kravchinsky, V. A., Quidelleur, X., Renne, P. R. and Gladkochub, D. P. (2010). Preliminary dating of the Viluy traps (eastern Siberia): eruption at the time of Late Devonian extinction events? *Earth and Planetary Science Letters*. 300, 239-245.

Cramer, B. D., Saltzman, M. R., Day, J. E. and Witzke, B. J. (2008). Record of the Late Devonian Hangenberg global positive carbon-isotope excursion in an epeiric sea setting: carbonate production, organic-carbon burial and paleoceanography during the Late Famennian. In:

Holmden, H. and Pratt, B. R. (eds) Dynamics of Epeiric Seas: Sedimentological, Paleontological and Geochemical Perspectives. *Geological Association of Canada*. 48, 103-118.

Creaney S. and Allan J. (1991). Hydrocarbon generation and migration in the Western Canada Sedimentary Basin. In Classic Petroleum Provinces (ed. J. Brooks). *Geological Society Specical. Publications*. 50, 189–202.

Creaser, R. A., Sannigrahi, P., Chacko, T. and Selby, D. (2002). Further evaluation of the Re-Os geochronometer in organic-rich sedimentary rocks: A test of hydrocarbon maturation effects in the Exshaw Formation, Western Canada Sedimentary Basin. *Geochimica et Cosmochimica Acta*. *66*(19), 3441-3452.

Cross, M. M., Manning, D. A., Bottrell, S. H., Worden, R. H. (2004). Thermochemical sulphate reduction (TSR): experimental determination of reaction kinetics and implications of the observed reaction rates for petroleum reservoirs. *Organic Geochemistry*. 35, 393–404.

Cruse, A. M. and Lyons, T. W. (2004). Trace metal records of regional paleoenvironmental variability in Pennsylvanian (Upper Carboniferous) black shales. *Chemical Geology.* 206, 319–345.

Crusius J., Calvert S., Pedersen T. and Sage D. (1996). Rhenium and molybdenum enrichments in sediments as indicators of oxic, suboxic and sulfidic conditions of deposition. Earth and Planetary Science Letters. 145, 65-78.

Dahl, T. W., Canfield, D. E., Rosing, M. T., Frei, R. E., Gordon, G. W., Knoll, A. H., and Anbar, A. D. (2011). Molybdenum evidence for expansive sulfidic water masses in~ 750 Ma oceans. Earth and Planetary Science Letters, 311(3-4), 264-274.

Dahl, T. W., Hammarlund, E. U., Anbar, A. D., Bond, D. P., Gill, B. C., Gordon, G. W. and Canfield, D. E. (2010). Devonian rise in atmospheric oxygen correlated to the radiations of terrestrial plants and large predatory fish. *Proceedings of the National Academy of Sciences*. 107(42), 17911-17915.

Dahl, T. W., Chappaz, A., Fitts, J. P. and Lyons, T. W. (2013). Molybdenum reduction in a sulfidic lake: Evidence from X-ray absorption fine-structure spectroscopy and implications for the Mo paleoproxy. *Geochimica et Cosmochimica Acta.* 103, 213-231.

Day, J., Witzke, B. and Rowe, H. (2011). Development of an epeirical subtropical paleoclimate record from western Euramerica: late Frasnian-earliest Tournaisian stable carbon isotope record from the Yellow Spring-NeW Albany Groups of the northwestern Illinois Basin. In: Geological Society of America Annual Meeting.

Dean, W.E., Gardner, J.V., Piper, D.Z. (1997). Inorganic geochemical indicators of glacial–interglacial changes in productivity and anoxia on the California continental margin. Geochimica et Cosmochimica Acta 61, 4507–4518.

Duan, Y., Anbar A. D., Arnold, G. L., Lyons, T. W., Gordon, G. W. and Kendall, B. (2010). Molybdenum isotope evidence for mild environmental oxygenation before the Great Oxidation Event. *Geochimica et Cosmochimica Acta.* 74, 6655-6668.

Duke M. J. M. (1983). Geochemistry of the Exshaw Shale of Alberta: An application of neutron activation analysis and related techniques. M.Sc. thesis, University of Alberta.

Dunk, R. M., Mills R. A. and Jenkins, W. J. (2002). A revaluation of the oceanic uranium budget for the Holocene. Chemical Geology. 190, 45-67.

Emerson, S. R., and Huested, S. S. (1991). Ocean anoxia and the concentrations of molybdenum and vanadium in seawater. Marine Chemistry, 34(3-4), 177-196.

Erickson, B. E., and Helz, G. R. (2000). Molybdenum (VI) speciation in sulfidic waters:: stability and lability of thiomolybdates. Geochimica et Cosmochimica Acta, 64(7), 1149-1158.

Feist, R. (1990). Guidebook of the Field Meeting Montagne Noire 1990.

Filipiak, P., Racki, G., 2010. Proliferation of abnormal palynoflora during the end- Devonian biotic crisis. Geol. Quart. 54 (1), 1–14.

Formolo, M. J., Riedinger, N. and Gill, B. C. (2014). Geochemical evidence for euxinia during the Late Devonian extinction events in the Michigan Basin (USA). *Palaeogeography, palaeoclimatology, palaeoecology*. 414, 146-154.

Gautier, D.L. (1986). Cretaceous shales from the western interior of North America: sulfur/carbon ratios and sulfur-isotope composition. *Geology* 14, 225–228.

Goldberg, T., Archer, C., Vance, D., Thamdrup, B., McAnena, A., and Poulton, S. W. (2012). Controls on Mo isotope fractionations in a Mn-rich anoxic marine sediment, Gullmar Fjord, Sweden. Chemical Geology, 296, 73-82.

Goldberg, T., Gordon, G., Izon, G., Archer, C., Pearce, C. R., McManus, and Rehkämper, M. (2013). Resolution of inter-laboratory discrepancies in Mo isotope data: an intercalibration. *Journal of Analytical Atomic Spectrometry.* 28(5), 724-735.

Goldberg, T., Poulton, S. W., Wagner, T., Kolonic, S. F., and Rehkämper, M. (2016). Molybdenum drawdown during cretaceous oceanic anoxic event 2. Earth and Planetary Science Letters, 440, 81-91.

Gomes, M. L., and Hurtgen, M. T. (2015). Sulfur isotope fractionation in modern euxinic systems: Implications for paleoenvironmental reconstructions of paired sulfate–sulfide isotope records. Geochimica et Cosmochimica Acta, 157, 39-55.

Gong, Y. M., Li, B. H., Si, Y. L., Wu, Y. (2002). Late Devonian red tide and mass extinction. *Chinese Science Bulletin*. 47, 1138-1144.

Gonzalez, F., Moreno, C., and Santos, A. (2006). The massive sulphide event in the Iberian Pyrite Belt: confirmatory evidence from the Sotiel-Coronada Mine. Geological Magazine, 143(6), 821-827.

Habicht, K.S., Canfield, D.E. (1997). Sulfur isotope fractionation during bacterial sulate reduction in organic-rich sediments. Geochim. Cosmochim. Acta 61, 5351–5361.

Habicht, K.S., Canfield, D.E. (2001). Isotope fractionation by sulfate-reducing natural populations and the isotopic composition of sulfide in marine sediments. Geology 29, 555–558.

Harrison, A.G., Thode, H.G. (1958). Mechanisms of the bacterial reduction of sulfate from isotope fractionation studies. Trans. Faraday Soc.53, 84–92.

Helz, G. R., Bura-Nakić, E., Mikac, N., and Ciglenečki, I. (2011). New model for molybdenum behavior in euxinic waters. Chemical Geology, 284(3-4), 323-332.

Helz, G. R., Miller, C. V., Charnock, J. M., Mosselmans, J. F. W., Pattrick, R. A. D., Garner, C. D., and Vaughan, D. J. (1996). Mechanism of molybdenum removal from the sea and its concentration in black shales: EXAFS evidence. Geochimica et Cosmochimica Acta, 60(19), 3631-3642.

Helz, G. R., and Vorlicek, T. P. (2019). Precipitation of molybdenum from euxinic waters and the role of organic matter. Chemical Geology, 509, 178-193.

Herrmann, A. D., Kendall, B., Algeo, T. J., Gordon, G. W., Wasylenki, L. E., and Anbar, A. D. (2012). Anomalous molybdenum isotope trends in Upper Pennsylvanian euxinic facies: Significance for use of δ98Mo as a global marine redox proxy. Chemical Geology, 324, 87-98.

Higgins, A. C., Richards, B. C., Henderson, C. M. (1991). Conodont biostratigraphy and paleoecology of the uppermost Devonian and Carboniferous of the Western Canada Sedimentary Basin. In: Orchard, M.J., McCracken, A.D. (Eds.), Ordovician to Triassic Conodont Paleontology of the Canadian Cordillera. *Geological Survey of Canada*. Calgary, Canada. 215-251.

Hiyagon, H. and Kennedy, B. M. (1992). Noble gases in natural gas of Alberta, Canada. *Geochimica et Cosmochimica Acta.* 56, 1569-1589.

Huang, C., Song, J., Shen, J., and Gong, Y. (2018). The influence of the Late Devonian Kellwasser events on deep-water ecosystems: Evidence from palaeontological and geochemical records from South China. *Palaeogeography, Palaeoclimatology, Palaeoecology*. 504, 60-74.

Isaacson, P. E., Diaz-Martinez, E., Grader, G. W., Kalvoda, J., Babek, O., and Devuyst, F. X. (2008). Late Devonian–earliest Mississippian glaciation in Gondwanaland and its biogeographic consequences. Palaeogeography, Palaeoclimatology, Palaeoecology, 268(3-4), 126-142.

Joachimski, M. M., Buggisch, W. (1993). Anoxic events in the Late Frasnian-causes of the Frasnian-Famennian faunal crisis? *Geology.* 21, 675-678.

Joachimski, M. M., Buggisch, W. (2002). Conodont apatite $\delta^{18}O$ signatures indicate climatic cooling as a trigger of the Late Devonian mass extinction. *Geology.* 30, 711-714.

Johnson, J. G., Klapper, G. and Sandberg, C. A. (1985). Devonian eustatic fluctuations in Euramerica. *Geological Society of America Bulletin*. 96, 567-587.

Kaiser, S. I. (2005). Mass Extinctions, Climatic and -Oceanographic Changes at the Devonian-Carboniferous Boundary. PhD thesis, Fakultatfur Geowissenschaften, Ruhr-Universitat Bochum.

Kaiser, S. I., Steuber, T., Becker, R. T. and Joachimski, M. M. (2006). Geochemical evidence for major environmental change at the Devonian–Carboniferous boundary in the Carnic Alps and the Rhenish Massif. *Palaeogeography, Palaeoclimatology, Palaeoecology*. 240, 146-160.

Kaiser, S. I., Steuber, T. and Becker, R. T. (2008). Environmental change during the Late Famennian and Early Tournaisian (Late Devonian-Early Carboniferous)-implications from stable isotopes and conodont biofacies in southern Europe. In: Aretz, M., Herbig, H.-G. and Somerville, I. D. (eds) Carboniferous Platforms and Basins. *Geological Journal*. 43, 241-260

Kaiser, S. I., Aretz, M. and Becker, R. T. (2016). The global Hangenberg Crisis (Devonian-Carboniferous transition): review of a first-order mass extinction. *Geological Society, London, Special Publications*. 423(1), 387-437.

Kampschulte, A. and Strauss, H. (2004). The sulfur isotopic evolution of Phanerozoic sea-water based on the analysis of structurally substituted sulfate in carbonates. *Chemical Geology*. 204, 255-286.

Kaplan, I.R., Rittenberg, S.C. (1964). Microbiological fractionation of sulfur isotopes. J. Gen. Microbiol. 34, 195–212.

Kazmierczak, J., Kremer, B. and Racki, G. (2012). Late Devonian marine anoxia challenged by benthic cyanobacterial mats. *Geobiology*. 10(5), 371-383.

Kendall B., Creaser R. A., Gordon G. W. and Anbar A. D. (2009). Re-Os and Mo isotope systematics of black shales from the Middle Proterozoic Velkerri and Wollogorang Formations, McArthur Basin, northern Australia. *Geochimica et Cosmochimica Acta*. 73, 2534-2558.

Kendall, B., Dahl, T. W. and Anbar, A. D. (2017). The stable isotope geochemistry of molybdenum. *Reviews in Mineralogy and Geochemistry*. 82(1), 683-732.

Kendall, B., Gordon, G. W., Poulton, S. W. andAnbar, A. D. (2011). Molybdenum isotope constraints on the extent of late Paleoproterozoic ocean euxinia. Earth and Planetary Science Letters, 307(3), 450-460.

Kendall, B., Komiya, T., Lyons, T. W., Bates, S. M., Gordon, G. W., Romaniello, S. J. and Jiang, G. (2015). Uranium and molybdenum isotope evidence for an episode of widespread ocean oxygenation during the late Ediacaran Period. *Geochimica et Cosmochimica Acta*. 156, 173-193.

King, H. E., Walters, C. C., Horn, W. C., Zimmer, M., Heines, M. M., Lamberti, W. A., Kliewer, C., Pottorf, R. J. and Macleod, G. (2014). Sulfur isotope analysis of bitumen and pyrite associated with thermal sulfate reduction in reservoir carbonates at the Big Piney-La Barge production complex. Geochimica et Cosmochimica Acta. 134, 210-220.

Kiyosu Y., Krouse H. R. and Viau C. A. (1990) Carbon isotope fractionation during oxidation of light hydrocarbon gases. In Geochemistry of Sulfur in Fossil Fuels (eds Orr W. L. and White C. M.), ACS Symposium Series No. 429, pp. 633-641. American Chemical Society. Washington, DC.

Komatsu, T., Kato, S., Hirata, K., Takashima, R., Ogata, Y., Oba, M., ... and Doan, T. N. (2014). Devonian–Carboniferous transition containing a Hangenberg Black Shale equivalent in the

Pho Han Formation on Cat Ba Island, northeastern Vietnam. Palaeogeography, Palaeoclimatology, Palaeoecology, 404, 30-43.

Ku, T. L., Knauss, K. and Mathieu, G. G. (1977). Uranium in the open ocean: concentration and isotopic composition. *Deep Sea Research*. 24, 1005-1017.

Kumpan, T., Babek, O., Kalvoda, J., Fryda, J. and Grygar, T. M. (2013). A high-resolution, multiproxy stratigraphic analysis of the Devonian–Carboniferous boundary sections in the Moravian Karst (Czech Republic) and a correlation with the Carnic Alps (Austria). *Geological Magazine*. 151, 201-215.

Kumpan, T., Babek, O., Kalvoda, J., Grygar, T. M. and Fryda, J. (2014). Sea-level and environmental changes around the Devonian-Carboniferous boundary in the Namur-Dinant Basin (S Belgium, NE France): a multiproxy stratigraphic analysis of carbonate ramp archives and its use in regional and interregional correlations. *Sedimentary Geology*. 311, 43-59.

Kumpan, T., Kalvoda, J., Bábek, O., Holá, M., and Kanický, V. (2019). Tracing paleoredox conditions across the Devonian–Carboniferous boundary event: A case study from carbonate-dominated settings of Belgium, the Czech Republic, and northern France. Sedimentary Geology, 380, 143-157.

Krouse, H. R., Viau, C. A., Eliuk, L. S., Ueda, A., Halas, S. (1988). Chemical and isotopic evidence of thermochemical sulfate reduction by light hydrocarbon gases in deep carbonate reservoirs. *Nature*. 333, 415-419.

Kravchinsky, V. A. (2012). Paleozoic large igneous provinces of Northern Eurasia: Correlation with mass extinction events. Global and Planetary Change, 86, 31-36.

Krstic, B., Grubic, A., Ramovs, A., and Filipovic, I. (1988). The Devonian of Yugoslavia.

Langmuir, D. (1978). Uranium solution-mineral equilibria at low temperatures with applications to sedimentary ore deposits. *Geochimica et Cosmochimica Acta*. 42(6), 547-569.

Leenheer, M. J. (1984) Mississippian Bakken and other equivalent formations as source rocks in the Western Canada basin. *Organic Geochemistry*. 6, 521-533.

Lev, S. M., McLennan, S. M. and Hanson, G. N. (2000). Late diagenetic redistribution of uranium and disturbance of the U-Pb whole rock isotope system in a black shale. *Journal of Sedimentary. Research*. 70, 1234-1245.

Leventhal, J. S. (1987). C and S relationships in Devonian shales from the Appalachian basin as an indicator of environment of deposition. *American Journal of Science*. 287: 33-49.

Lewan, M.D. (1984). Factors controlling the proportionality of vanadium to nickel in crude oils. *Geochimica et Cosmochimica Acta*. 48, 2231-2238.

Lewan, M.D. and Maynard, J.B. (1982). Factors controlling enrichment of vanadium and nickel in the bitumen of organic sedimentary rocks. *Geochimica et Cosmochimica Acta*. 46, 2547-2560.

Liu, X., Fike, D., Li, A., Dong, J., Xu, F., Zhuang, G., ... and Wan, S. (2019). Pyrite sulfur isotopes constrained by sedimentation rates: Evidence from sediments on the East China Sea inner shelf since the late Pleistocene. Chemical Geology, 505, 66-75.

Liu, J., Qie, W., Algeo, T. J., Yao, L., Huang, J., and Luo, G. (2016). Changes in marine nitrogen fixation and denitrification rates during the end-Devonian mass extinction. Palaeogeography, palaeoclimatology, palaeoecology, 448, 195-206.

Liu, Y. Q., Ji, Q., Kuang, H. W., Jiang, X. J., Xu, H., and Peng, N. (2012). U–Pb zircon age, sedimentary facies, and sequence stratigraphy of the Devonian–Carboniferous boundary, Daposhang Section, Guizhou, China. Palaeoworld, 21(2), 100-107.

Lu, X., Kendall, B., Stein, H. J., Li, C., Hannah, J. L., Gordon, G. W., and Ebbestad, J. O. R. (2017). Marine redox conditions during deposition of Late Ordovician and Early Silurian organic-rich mudrocks in the Siljan ring district, central Sweden. *Chemical Geology*. 457, 75-94.

Lyons, T.W. (1997). Sulfur isotopic trends and pathways of iron sulfide formation in upper Holocene sediments of the anoxic Black Sea. *Geochimica et Cosmochimica Acta*. 61, 3367–3382.

Lyons, T. W., Werne, J. P., Hollander, D. J., and Murray, R. W. (2003). Contrasting sulfur geochemistry and Fe/Al and Mo/Al ratios across the last oxic-to-anoxic transition in the Cariaco Basin, Venezuela. Chemical Geology, 195(1-4), 131-157.

Ma, X. P., Gong, Y. M., Chen, D. Z., Racki, G., Chen, X. Q. and Liao, W. H. (2016). The Late Devonian Frasnian-Famennian event in South China—patterns and causes of extinctions, sea level changes, and isotope variations. *Palaeogeography, Palaeoclimatology, Palaeoecology*. 448, 224-244.

Macdonald, D. E. (1985). Sedimentary phosphate rock in Alberta and southeastern British Columbia: resource potential, the industry, technology and research needs. *CIM Bull* 81: 46-52

Machel, H. G. (2001). Bacterial and thermochemical sulfate reduction in diagenetic settings—old and new insights. *Sedimentary Geology*.140, 143-175.

Machel, H. G., Krouse, H. R. and Sassen, R. (1995). Products and distinguishing criteria of bacterial and thermochemical sulfate reduction. *Applied Geochemistry*.10, 373-389.

MacQueen R. A. and Sandberg C. A. (1970). Stratigraphy, age, and interregional correlation of the Exshaw Formation, Alberta Rocky Mountains. *Bulletin of Canada Petroleum Geology*. 18, 32-66.

Magnall, J. M., Gleeson, S. A., Poulton, S. W., Gordon, G. W., and Paradis, S. (2018). Links between seawater paleoredox and the formation of sediment-hosted massive sulphide (SHMS) deposits—Fe speciation and Mo isotope constraints from Late Devonian mudstones. Chemical Geology, 490, 45-60.

Martinez, A. M., Boyer, D. L., Droser, M. L., Barrie, C., and Love, G. D. (2019). A stable and productive marine microbial community was sustained through the end-Devonian Hangenberg Crisis within the Cleveland Shale of the Appalachian Basin, United States. Geobiology, 17(1), 27-42.

Marshall, J. E. A. 2010. The Late Devonian and Early Carboniferous terrestrial climatic record. In: Programme and Abstracts, International Palaeontological Congress, 28 June–3 July 2010, London, 263.

Marynowski, L., Zaton, M., Rakocinski, M., Filipiak, P., Kurkiewicz, S. and Pearce, T. J. (2012). Deciphering the upper Famennian Hangenberg Black Shale depositional environments based on multi-proxy record. *Palaeogeography, Palaeoclimatology, Palaeoecology*. 346-347, 66-86.

Marynowski, L. and Filipiak, P. (2007). Water column euxinia and wildfire evidence during deposition of the Upper Famennian Hangenberg event horizon from the Holy Cross Mountains (central Poland). *Geological Magazine*. 144, 569-595.

Matyja, H., Sobień, K., Marynowski, L., STEMPIEŃ-SAŁEK, M. A. R. Z. E. N. A., and Małkowski, K. (2015). The expression of the Hangenberg Event (latest Devonian) in a relatively shallow-marine succession (Pomeranian Basin, Poland): the results of a multi-proxy investigation. Geological Magazine, 152(3), 400-428.

Matyja, H., Malkowski, K., Sobien, K. and Stempien- Salek, M. (2010). Devonian-Carboniferous boundary in Poland: conodont and miospore successions and event stratigraphy. In: Programme and Abstracts, International Palaeontological Congress, 28 June-3 July 2010, London, 268.

Matyja, H., Sobien, K., Marynowski, L., Stempien-Salek, M. and Malkowski, K. (2014). The expression of the Hangenberg Event (latest Devonian) in a relatively shallow-marine succession (Pomeranian Basin, Poland): the results of a multi-proxy investigation. *Geological Magazine*. 153, 429-443.

Mayer, B. and Krouse, H.R. (2004). Procedures for sulfur isotope abundance studies. In: de Groot, P.A. (Ed.), *Handbook of Stable Isotope Analytical Techniques*, Elsevier, pp.538-596.

McGhee, G.R. (1996). The Late Devonian Mass Extinction. *Columbia University Press*, New York (303 pp.).

McGhee Jr., G.R., Clapham, M.E., Sheehan, P.M., Bottjer, D.J. and Droser, M.L. (2013). A new ecological-severity ranking of major Phanerozoic biodiversity crises. *Palaeogeography, Palaeoclimatology, Palaeoecology*. 370, 260-270.

McLennan, S. M. (2001). Relationships between the trace element composition of sedimentary rocks and upper continental crust. *Geochemistry, Geophysics, Geosystems*. 2(4).

Meijer Drees and N.C, Johnston, D.I. (1993). Geology of the Devonian±Carboniferous boundary beds in Alberta. In: Karvonen, R., Haan, J.D., Jang, K., Robinson, D., Smith, G., Webb, T., Wittenberg, J. (Eds.), Carboniferous to Jurassic Pangea-Core Workshop, C.S.P.G. and *Global Sedimentary Geology Program.* Calgary, pp. 188±205.

Miller, K. G., MouNtaiN, G. S., WriGht, J. D., and BroWNiNG, J. V. (2011). Sea level and ice Volume Variations. *Oceanography.* 24(2), 40-53.

Mongenot, T., Tribovillard, N. P., Desprairies, A.,Verges, E. L. and Defarge, F. L. (1996). Trace elements as palaeoenvironmental markers in strongly mature hydrocarbon source rocks: the Cretaceous La Luna Formation of Venezuela. *Sedimentary Geology*. 103, 23-37.

Morford, J. L., and Emerson, S. (1999). The geochemistry of redox sensitive trace metals in sediments. *Geochimica et Cosmochimica Acta*. 63(11), 1735-1750.

Morford, J. L., Emerson, S. R., Breckel, E. J., and Kim, S. H. (2005). Diagenesis of oxyanions (V, U, Re, and Mo) in pore waters and sediments from a continental margin. *Geochimica et Cosmochimica Acta*. 69(21), 5021-5032.

Morford J. L., Martin W. R. and Carney C. M. (2012) Rhenium geochemical cycling: Insights from continental margins. *Chemical Geology*. 324-325, 73-86.

Murphy, A. E., Sageman, B. B., Hollander, D. J. (2000). Eutrophication by decoupling of the marine biogeochemical cycles of C, N, and P: a mechanism for the Late Devonian mass extinction. *Geology.* 28, 427-430.

Myrow, P. M., Strauss, J. V., Creveling, J. R., Sicard, K. R., Ripperdan, R., Sandberg, C. A. and Hartenfels, S. (2011). A carbon isotopic and sedimentological record of the latest Devonian (Famennian) from the Western U.S. and Germany. Palaeogeography, Palaeoclimatology, Palaeoecology, 306, 147–159.

Myrow, P. M., Ramezani, J., Hanson, A. E., Bowring, S. A., Racki, G., and Rakociński, M. (2014). High-precision U-Pb age and duration of the latest Devonian (Famennian) Hangenberg event, and its implications. *Terra Nova*. *26*(3), 222-229.

Nägler, T. F., Anbar, A. D., Archer, C., Goldberg, T., Gordon, G. W., Greber, N. D., Siebert, C., Sohrin, Y. and Vance, D. (2014). Proposal for an international molybdenum isotope measurement standard and data representation. *Geostandards and Geoanalytical Research.* 38(2), 149-151.

Nägler, T. F., Neubert, N., Böttcher, M. E., Dellwig, O. and Schnetger, B. (2011). Molybdenum isotope fractionation in pelagic euxinia: Evidence from the modern Black and Baltic Seas. *Chemical Geology*. 289(1), 1-11.

Nakagawa, Y., Takano S., Firdaus M. L., Norisuye K., Hirata T., Vance D. and Sohrin Y. (2012). The molybdenum isotopic composition of the modern ocean. *Geochemical Journal* 46, 131-141.

Nameroff, T. J., Balistrieri, L. S., and Murray, J. W. (2002). Suboxic trace metal geochemistry in the eastern tropical North Pacific. Geochimica et Cosmochimica Acta, 66(7), 1139-1158.

Neely, R. A., Gislason, S. R., Ólafsson, M., McCoy-West, A. J., Pearce, C. R., and Burton, K. W. (2018). Molybdenum isotope behaviour in groundwaters and terrestrial hydrothermal systems, Iceland. Earth and Planetary Science Letters, 486, 108-118.

Neubert, N., Nägler, T. F. and Böttcher, M. E. (2008). Sulfidity controls molybdenum isotope fractionation into euxinic sediments: Evidence from the modern Black Sea. *Geology* 36(10), 775-778.

Noordmann, J., Weyer, S., Montoya-Pino, C., Dellwig, O., Neubert, N., Eckert, S., Paetzel, M. and Böttcher, M.E. (2015). Uranium and molybdenum isotope systematics in modern euxinic basins: Case studies from the central Baltic Sea and the Kyllaren fjord (Norway). *Chemical Geology*. 396, 182-195.

Núñez-Useche, F., Canet, C., Barragán, R., Alfonso, P. (2016). Bioevents and redox conditions around the Cenomanian-Turonian anoxic event in Central Mexico. Palaeogeogr. Palaeoclimatol. Palaeoecol. 449, 205–226.

Orr, W. L. (1977). Geologic and geochemical controls on the distribution of hydrogen sulfide in natural gas. In: *Advances in Organic Geochemistry*. pp.571-597.

Partin, C. A., Lalonde, S. V., Planavsky, N. J., Bekker, A., Rouxel, O. J., Lyons, T. W., and Konhauser, K. O. (2013). Uranium in iron formations and the rise of atmospheric oxygen. *Chemical Geology*. 362, 82-90.

Paschall, O., Carmichael, S. K., Königshof, P., Waters, J. A., Ta, P. H., Komatsu, T., and Dombrowski, A. (2019). The Devonian-Carboniferous boundary in Vietnam: Sustained ocean anoxia with a volcanic trigger for the Hangenberg Crisis?. Global and Planetary Change, 175, 64-81.

Peters, K. E. (1986). Guidelines for evaluating petroleum source rock using programmed pyrolysis. *AAPG bulletin*. 70(3), 318-329.

Piggott N. and Lines M. D. (1991). A case study of migration from the West Canada Basin. In Petroleum Migration (eds. W. A. England and A. J. Fleet). *Geological Society Special Publications*. 59, 207-225.

Podruski J. A., Barclay J. E., Hamblin A. P., Lee P. J., Osadetz K. G., Procter R. M. and Taylor G. C. (1988). Conventional oil resources of western Canada, Part 1: Resource endowment. *Geological Survey of Canada Paper.* 87-26.

Porter, S. J., Selby, D. and Cameron, V. (2014). Characterising the nickel isotopic composition of organic-rich marine sediments. *Chemical Geology*, *387*, 12-21.

Poulson, R. L., Siebert, C., McManus, J. and Berelson, W. M. (2006). Authigenic molybdenum isotope signatures in marine sediments. *Geology.* 34(8), 617-620.

Poulton, S.W., Canfield, D.E. (2005). Development of a sequential extraction procedure for iron: implications for iron partitioning in continentally derived particulates. Chem. Geol. 214, 209–221.

Poulton, S.W., Krom, M.D., Raiswell, R. (2004). A revised scheme for the reactivity of iron (oxyhydr)oxide minerals towards dissolved sulfide. Geochim. Cosmochim. Acta 68, 3703–3715.

Poulson Brucker, R. L., McManus, J., Severmann, S. and Berelson, W. M. (2009). Molybdenum behavior during early diagenesis: Insights from Mo isotopes. *Geochemistry Geophysics Geosystems*. 10(6).

Poulton, S. W., and Canfield, D. E. (2011). Ferruginous conditions: a dominant feature of the ocean through Earth's history. Elements, 7(2), 107-112.

Poulton, S. W. and Raiswell, R. (2002) The low-temperature geochemical cycle of iron: From continental fluxes to marine sediment deposition. American Journal of Science, 302, 774-805.

Pracht, M., Batchelor, R. (1998). A geochemical study of late Devonian and early Carboniferous tuffs from the South Munster Basin, Ireland. Iri. J. Earth Sci. 25–38.

Pratt, B. R. and van Heerde, J. (2016). An arborescent lycopsid stem fragment from the Palliser Formation (Famennian) carbonate platform, southwestern Alberta, Canada, and its paleogeographic and paleoclimatic significance. *Canadian Journal of Earth Sciences*. *54*(2), 141-145.

Pujol, M., Bourdon, B., Brennwald, M. and Kipfer, R. (2017). Physical processes occurring in tight gas reservoirs from Western Canadian Sedimentary Basin: Noble gas signature. *Chemical Geology*.

Qie, W., Liu, J., Chen, J., Wang, X., Mii, H. S., Zhang, X., ... and Luo, G. (2015). Local overprints on the global carbonate δ13C signal in Devonian–Carboniferous boundary successions of South China. Palaeogeography, Palaeoclimatology, Palaeoecology, 418, 290-303.

Racki, G., Rakocinski, M., Marynowski, L. and Wignall, P. B. (2018). Mercury Enrichments and the Frasnian–Famennian Biotic Crisis: A Volcanic Trigger Proved.

Raiswell, R. (1982). Pyrite texture, isotopic composition and the availability of iron. Am. J. Sci. 282, 1244–1263.

Raiswell, R. and Berner, R. A. (1987). Organic carbon losses during burial and thermal maturation of normal marine shales. *Geology*. 15, 853-856.

Reinhard, C. T., Planavsky, N. J., Robbins, L. J., Partin, C. A., Gill, B. C., Lalonde, S. V., Bekker, A., Konhauser, K. O. and Lyons, T. W. (2013). Proterozoic ocean redox and biogeochemical stasis. *Proceedings of the National Academy of Sciences*. 110(14), 5357-5362.

Ricci, J., Quidelleur, X., Pavlov, V., Orlov, S., Shatsillo, A., and Courtillot, V. (2013). New 40Ar/39Ar and K–Ar ages of the Viluy traps (Eastern Siberia): further evidence for a relationship with the Frasnian–Famennian mass extinction. Palaeogeography, Palaeoclimatology, Palaeoecology, 386, 531-540.

Richards, B. C. and Higgins, A. C. (1988). Devonian-Carboniferous boundary beds of the Palliser and Exshaw formations at Jura Creek, Rocky Mountains, southwestern Alberta. In:

McMillan NJ, Embry AF, Glass DJ (eds) Devonian of the world. *Canadian Society of Petroleum Geologists Memoir.*

Richards, B. C., Mamet, B. L. and Bamber, E.W. (1999). Uppermost Devonian and Carboniferous sequence stratigraphy, biostratigraphy and basin development, Banff region, southwestern Alberta. XIV International Congress on the Carboniferous and Permian. *Geological Survey of Canada*. University of Calgary, p. 193.

Richards, B. C., Ross, G. M., and Utting, J. (2002), UPb geochronology, lithostratigraphy and biostratigraphy of tuff in the upper Famennian to Tournaisian Exshaw Formation: Evidence for a mid-Paleozoic magmatic arc on the northwestern margin of North America, in Hills, L.V., et al., eds., Carboniferous and Permian of the world: *Canadian Society of Petroleum Geologists Memoir*. 19, p. 158-207.

Rimmer, S. M. (2004). Geochemical paleoredox indicators in Devonian–Mississippian black shales, central Appalachian Basin (USA). Chemical Geology, 206(3-4), 373-391.

Robison, V. D. (1995). The Exshaw Formation: a Devonian/Mississippian hydrocarbon source in the Western Canada Basin. In *Petroleum source rocks* (pp. 9-24). Springer, Berlin, Heidelberg.

Rodhe, H. (1992). 4 Modeling Biogeochemical Cycles. In International Geophysics (Vol. 50, pp. 55-72). Academic Press.

Ross, D. J. and Bustin, R. M. (2009). Investigating the use of sedimentary geochemical proxies for paleoenvironment interpretation of thermally mature organic-rich strata: examples from the Devonian–Mississippian shales, Western Canadian Sedimentary Basin. *Chemical Geology*. 260(1-2), 1-19.

Ryder, R. T. (1996). Fracture patterns and their origin in the upper Devonian Antrim Shale gas reservoir of the Michigan basin; a review (No. 96-23). *US Geological Survey.*

Saltzman, M. R. (2005). Phosphorus, nitrogen, and the redox evolution of the Paleozoic oceans. Geology, 33, 573–576.

Sandberg, C. A., Morrow, J. R. and Ziegler, W. (2002). Late Devonian sea-level changes, catastrophic events, and mass extinctions. In: Koeberl, C., Macleod, K.G. (Eds.), Catastrophic Events and Mass Extinction: Impacts and Beyond. *Geological Society of America Special. Paper*. 356. pp. 473-487.

Sandberg, C.A., Ziegler, W., Leuteritz, K., Brill, S.M. (1978). Phylogeny, speciation, and zonation of siphonodella (Conodonta, Upper Devonian and Lower Carboniferous). *Newsletter Stratigraphy*. 7, 102-120.

Sarmiento, J. L., and Gruber, N. (2006). Ocean biogeochemical dynamics. Princeton university press.

Savoy, L. E. (1990). Sedimentary record of Devonian-Mississippian carbonate and black shale systems, southernmost Canadian Rockies and adjacent Montana.

Savoy, L. E. and Harris, A. G. (1993). Conodont biofacies and taphonomy along a carbonate ramp to black shale basin (latest Devonian and earliest), southernmost Canadian Cordillera and adjacent Montana. *Canadian Journal of Earth Science*. 30, 2404-2422.

Scholz, F., Hensen, C., Noffke, A., Rohde, A., Liebetrau, V., and Wallmann, K. (2011). Early diagenesis of redox-sensitive trace metals in the Peru upwelling area–response to ENSO-related oxygen fluctuations in the water column. Geochimica et Cosmochimica Acta, 75(22), 7257-7276.

Scholze, F. and Gess, R. W. (2017). Oldest known naiaditid bivalve from the high-latitude Late Devonian (Famennian) of South Africa offers clues to survival strategies following the Hangenberg mass extinction. *Palaeogeography, Palaeoclimatology, Palaeoecology*. *471*, 31-39.

Scott, C., Lyons, T. W., Bekker, A., Shen, Y. A., Poulton, S. W., Chu, X. L. and Anbar, A. D. (2008). Tracing the stepwise oxygenation of the Proterozoic ocean. *Nature*. 452(7186), 456-459.

Scott, C. and Lyons, T. W. (2012). Contrasting molybdenum cycling and isotopic properties in euxinic versus non-euxinic sediments and sedimentary rocks: refining the paleoproxies. *Chemical Geology*. 324, 19-27.

Scott, C., Slack, J. F. and Kelley, K. D. (2017). The hyper-enrichment of V and Zn in black shales of the Late Devonian-Early Mississippian Bakken Formation (USA). *Chemical Geology*. 452, 24-33.

Selby, D. and Creaser, R. A. (2003). Re–Os geochronology of organic rich sediments: an evaluation of organic matter analysis methods. *Chemical Geology*. *200*(3-4), 225-240.

Selby, D. and Creaser, R. A. (2005). Direct radiometric dating of the Devonian-Mississippian time-scale boundary using the Re-Os black shale geochronometer. *Geology*. *33*(7), 545-548.

Sepkoski Jr, J. J. (1986). Phanerozoic overview of mass extinction. In Patterns and Processes in *the History of Life* (pp. 277-295). Springer Berlin Heidelberg.

Siebert C., Nagler T. F., von Blanckenburg F. and Kramers J. D. (2003). Molybdenum isotope records as a potential new proxy for paleoceanography. *Earth and Planetary Science Letters*. 211, 159-171.

Siebert C, McManus J, Bice A, Poulson R and Berelson WM. (2006). Molybdenum isotope.

Sheen, A. I., Kendall, B., Reinhard, C. T., Creaser, R. A., Lyons, T. W., Bekker, A., Poulton, S. and Anbar, A. D. (2018). A model for the oceanic mass balance of rhenium and implications for the extent of Proterozoic ocean anoxia. *Geochimica et Cosmochimica Acta*. 227, 75-95.

Smith, M. G., and Bustin, R. M. (1998). Production and preservation of organic matter during deposition of the Bakken Formation (Late Devonian and Early Mississippian), Williston Basin. Palaeogeography, Palaeoclimatology, Palaeoecology, 142(3-4), 185-200.

Smith, M. G. and Bustin, R. M. (2000). Late Devonian and Early Mississippian Bakken and Exshaw black shale source rocks, Western Canada Sedimentary Basin: a sequence stratigraphic interpretation. AAPG bulletin. 84(7), 940-960.

Song, H., Song, H., Algeo, T. J., Tong, J., Romaniello, S. J., Zhu, Y., ... and Anbar, A. D. (2017). Uranium and carbon isotopes document global-ocean redox-productivity relationships linked to cooling during the Frasnian-Famennian mass extinction. Geology, 45(10), 887-890.

Sorauf, J. E., and Pedder, A. E. H. (1986). Late Devonian rugose corals and the Frasnian–Famennian crsis. Canadian Journal of Earth Sciences, 23(9), 1265-1287.

Stasiuk, L. D. and Fowler, M. G. (2004). Organic facies in Devonian and Mississippian strata of Western Canada Sedimentary Basin: relation to kerogen type, paleoenvironment, and paleogeography. *Bulletin of Canadian Petroleum Geology*, *52*(3), 234-255.

Streel, M., Caputo, M.V., Loboziak, S. and Melo, J. H. G. (2000). Late Frasnian–Famennian climates based on palynomorph analyses and the question of the Late Devonian glaciations. *Earth-Sciece Reviews*. 52, 121-173.

Stylo, M., Neubert, N., Wang, Y., Monga, N., Romaniello, S. J., Weyer, S. and Bernier- Latmani, R. (2015). Uranium isotopes fingerprint biotic reduction. *Proceedings of the National Academy of Sciences*. 112(18), 5619-5624.

Taylor, S. R. and McLennan, S. M. (1995). The geochemical evolution of the continental crust. *Reviews of Geophysics.* 33, 241-265.

Trapp, E., Kaufmann, B., Mezger, K., Korn, M., and Weyer, D. (2004). Numerical calibration of the Devonian-Mississippian boundary: Two new U-Pb isotope dilution-thermal ionization mass spectrometry single-zircon ages from Hasselbachtal (Sauerland, Germany): *Geology*. 32, 857-860.

Trela, W. and Malec, J. (2007). Zapis d^{13}C wosadach pogranicza dewonu i karbonuw poludniowej czesci Gor Swietokrzyskich. *Przeglad Geologiczny*. 55, 411-415.

Tribovillard, N., Algeo, T. J., Lyons, T., and Riboulleau, A. (2006). Trace metals as paleoredox and paleoproductivity proxies: an update. *Chemical Geology*. 232(1), 12-32.

Tucker, R. D., Bradley, D. C., Ver Straeten, C. A., Harris, A. G., Ebert, J. R., and McCutcheon, S. R. (1998). New U-Pb zircon ages and the duration and division of Devonian time: *Earth and Planetary Science Letters*. 158, 175-186.

Veeh, H. H. (1967). Deposition of uranium from the ocean. Earth and Planetary Science Letters, 3, 145-150.

Wallace, M. W., Shuster, A., Greig, A., Planavsky, N. J. and Reed, C. P. (2017). Oxygenation history of the Neoproterozoic to early Phanerozoic and the rise of land plants. *Earth and Planetary Science Letters.* 466, 12-19.

Walliser, O. H. (1996). Global events in the Devonian and Carboniferous. In: Walliser, O. (Ed.), Global Events and Event Stratigraphy in the Phanerozoic. Springer-Verlag, Berlin, pp. 225-250.

Wang, J. (2016). Uranium and Molybdenum Isotope Constraints on Ocean Redox Conditions During Deposition of the Upper Devonian Kettle Point Formation, Ontario (Master's thesis, University of Waterloo).

Wang, P., Chen, Z., Jin, Z., Jiang, C., Sun, M., Guo, Y., Chen. X. and Jia, Z. (2018). Shale oil and gas resources in organic pores of the Devonian Duvernay Shale, Western Canada Sedimentary Basin based on petroleum system modeling. *Journal of Natural Gas Science and Engineering*, *50*, 33-42.

Wanty, R. B. and Goldhaber, M. B. (1992). Thermodynamics and kinetics of reactions involving vanadium in natural systems: accumulation of vanadium in sedimentary rocks. *Geochimica et Cosmochimica Acta*. 56, 1471-1483.

Warren, M. J. and Cooper, M. (2017). Classic hydrocarbon traps and analog structures in the southern Canadian Rockies. *AAPG Bulletin*, *101*(4), 589-597.

Wei, H., Wei, X., Qiu, Z., Song, H. and Shi, G. (2016). Redox conditions across the G–L boundary in South China: Evidence from pyrite morphology and sulfur isotopic compositions. Chemical Geology, 440, 1-14.

Weyer S., Anbar A. D., Gerdes A., Gordon G. W., Algeo T. J. and Boyle E. A. (2008). Natural fractionation of $^{238}U/^{235}U$. *Geochimica et Cosmochimica Acta*. 72, 345-359.

White, D. A., Elrick, M., Romaniello, S., and Zhang, F. (2018). Global seawater redox trends during the Late Devonian mass extinction detected using U isotopes of marine limestones. Earth and Planetary Science Letters, 503, 68-77.

Witzke, B. J. and Heckel, P. H. (1988). Paleoclimatic indicators and inferred Devonian paleolatitudes of Euramerica. In: McMillan NJ, Embry AF, Glass DJ (eds) Devonian of the world. Canadian Society Petroleum Geology. 14: 49-63.

Wicander, R., Clayton, G., Marshall, J. E. A., Troth, I. and Racey, A. 2011. Was the latest Devonian glaciation a multiple event? New palynological evidence from Bolivia. Palaeogeography, Palaeoclimatology, Palaeoecology, 305, 75–83.

Xu, D.Y, Zhang, Q.W., Sun, Y.Y., Yan, Z., Chai, Z.F., He, J.W., 1989. Event stratigraphy and extraterrestrial events. In: Duff, P.D., Smith, A.J. (Eds.), Astrogeological Events in China. Scottish Academic Press, Edinburgh, 264 pp.

Yang, S., Kendall, B., Lu, X., Zhang, F. and Zheng, W. (2017). Uranium isotope compositions of mid-Proterozoic black shales: Evidence for an episode of increased ocean oxygenation at 1.36 Ga and evaluation of the effect of post-depositional hydrothermal fluid flow. *Precambrian Research*. 298, 187-201.

Zhang, S., Wang, X., Wang, H., Bjerrum, C. J., Hammarlund, E. U., Costa, M. M., ... and Canfield, D. E. (2016). Sufficient oxygen for animal respiration 1,400 million years ago. Proceedings of the National Academy of Sciences, 113(7), 1731-1736.

Zhou L, Wignall PB, Su J, Feng Q, Xie S, Zhao L, Huang J. (2012). U/Mo ratios and $\delta^{98/95}$Mo as local and global redox proxies during mass extinction events. Chem Geol 324-325:99-107.

Zhou L, Algeo TJ, Shen J, Hu Z, Gong H, Xie S, Huang J, Gao S. (2015). Changes in marine productivity and redox conditions during the Late Ordovician Hirnantian glaciation. Palaeogeogr Palaeoclimatol Palaeoecol 420:223-234.